STUDY OF THE I-35W HIGHWAY BRIDGE COLLAPSE MECHANISM

by

Miguel A. Robles Lora

Thesis submitted to the Faculty of the

Virginia Polytechnic Institute and State University

In partial fulfillment of the requirements for the degree of

Master of Science

In

Civil Engineering

William J. Wright, Chair

Roberto T. Leon

Cristopher D. Moen

April 30, 2013

Blacksburg, VA

Keywords: I-35W Bridge Collapse, Collapse Mechanism, Gusset Plate Buckling, Plastic Hinges, Plastic deformations

STUDY OF THE I-35W HIGHWAY BRIDGE COLLAPSE MECHANISM

Miguel A. Robles Lora

ABSTRACT

The Deck truss portion of the I-35W Highway Bridge in Minneapolis, Minnesota collapsed on August 1, 2007 while roadwork was underway on the bridge. The entire truss was recovered from the river to study the causes of failure. The National Transportation Safety Board attributes the collapse to inadequate load carrying capacity of the steel gusset plates connecting the main truss members at four specific nodes. Permanent deformations of the members in proximity to these nodes were documented and a surveillance video camera recorded the collapse event in a major section of the structure.

The inelastic behavior of the deck truss during the collapse event is studied in this research by performing nonlinear structural analysis on a simplified two-dimensional model. Nonlinear behavior is discretized at specific locations starting with buckling of the critical gusset plates and continuing with yielding in members where the internal forces increased at a higher rate during the post-buckling behavior.

The analysis results show the sequence of failure events that lead to the formation of a collapse mechanism in the center span of the deck truss, which is the first to fall into the river. Comparison between the available evidence and the analysis results validate the conclusions drawn in this research.

ACKNOWLEDGEMENTS

I would like to extend my gratitude to those who contributed in making this thesis possible and to the ones who supported me throughout the process. First to the Virginia Tech Faculty, especially to Dr. William Wright for providing me plenty information for this study, for his guidance and support and as my committee chair, to Dr. Roberto Leon and Dr. Cristopher Moen for their advice and help as committee members, and to Dr. Mathew Eatherton for this teaching and helpful knowledge my research.

Appreciation is extended to the Fulbright Scholarship for making my graduate education possible through their excellent program, and LASPAU for the advice and assistance provided as administrator of my scholarship. To PUCMM for the support provided during the application process and trusting in my commitment. Also, to Antonio Franco for incentivize and support me in both academic and professional matters.

Special thanks go to my mother Daysi Lora, my father Jose Robles, my older brother Jose Alejandro Robles and the rest of my family for their love, encouragement and unconditional support during my entire life, I would not have come this far without them. Also to my fiancée, Anafran Henriquez for her love, patience, understanding and the help in preparing my defense presentation. Lastly to all my friends here in Blacksburg for making my life more enjoyable these past two years.

TABLE OF CONTENTS

LIST OF TABLES

LIST OF FIGURES

CHAPTER 1. INTRODUCTION, OBJECTIVES AND ORGANIZATION

1.1 Introduction

The Warren-type Deck truss portion of the I-35W Highway Bridge in Minneapolis, Minnesota, shown in Figure 1.1-1, collapsed on August 1, 2007 while roadwork was underway on the bridge. The entire truss was recovered from the river to study the causes of failure. The National Transportation Safety Board (NTSB) attributes the collapse to inadequate load carrying capacity of the steel gusset plates connecting the main truss members at four specific nodes. Permanent deformations of the members in the proximity of these nodes were documented and a surveillance video camera recorded the collapse of a major part of the structure.

Figure 1.1-1: View of the deck truss portion of the bridge, looking northeast (Source: NTSB)

The main truss portion of the bridge separated into three sections during the collapse. Most of the center section fell into the river while the north and south sections fell onto land. The video footage shows that the collapse mechanism started at the south end of the center span and progressed to the north end of the center span.

The inelastic behavior of the main truss during the collapse event is studied in this research. The study is based on nonlinear structural analysis of a simplified two-dimensional model using the software *SAP2000* version 14 (CSI, 2009). Nonlinear behavior was discretized at specific locations starting with buckling of the critical gusset plates, which is the triggering event, and continuing with yielding in members where the internal forces increased at a higher rate during the post-buckling behavior.

Two general inelastic phenomena are considered: gusset plate buckling modeled with Nonlinear Link elements and plastic deformation of the modeled with Frame Hinge properties. The constitutive relations for the links and hinges are determined by finite element analysis and cross section fiber analysis. To ensure convergence in the structural analysis, the fracture phenomenon is not considered because it would cause a drop on loading that might prevent the formation of a full collapse mechanism.

The analysis results show the failure sequence of events that lead to the formation of a collapse mechanism in the center span of the deck truss. During the actual collapse, after the center spans was separated from the end spans, these were pulled off their bearings and collapsed back onto the riverbanks. These are considered secondary collapses and are not addressed in this study.

1.2 Objectives

The collapse of the I-35W Highway Bridge in Minneapolis, Minnesota in 2007 is very well documented and several publications present in-depth studies of the causes of the collapse. Most of these studies are focused on the initial triggering event and little attention is given to the subsequent failures that developed the collapse mechanism. The primary objective of this research is study the event-to-event collapse sequence of the bridge until a collapse mechanism was formed. This provides a better understanding of the inelastic behavior of the system. A secondary objective is to correlate the permanent deformations predicted in the nonlinear model to the documented deformations of members recovered from the wreckage and the deflected shape captured by surveillance video camera to validate the results of this study.

1.3 Thesis Organization

This thesis is presented in five chapters. After this introduction, Chapter 2 presents a literature review of the bridge description, the accident report and existing studies of the collapse. Chapter 3 describes the analysis techniques, the development of the structural models, and their purposes. The analysis results and collapse study are presented in detail and discussed in Chapter 4. Conclusions on the most important findings are presented in Chapter 5.

CHAPTER 2. LITERATURE REVIEW

2.1 Bridge Description

The main truss portion of the I-35W highway bridge over the Mississippi River in Minneapolis, Minnesota (National Bridge Inventory structure no. 9340), was a Warren-type Deck Truss designed under the 1961 American Association of State Highway Officials (AASHO), *Standard Specifications for Highway Bridges* (NTSB, 2008). Final design plans were approved by the Minnesota Department of Transportation (MN/DOT) on June 18, 1965 and the bridge opened to traffic in 1967.

The two main trusses (east truss and west truss) had three spans and cantilever ends that supported the approach spans (see Figure 2.1-1). The trusses were spaced at 72 ft.-4 in. and were connected transversely by 27 floor trusses (which cantilevered out 16 ft. beyond the main trusses) and two floor beams at the ends, all spaced longitudinally at 38 ft. for a total length of 1,064 ft.

The cast-in-place reinforced concrete deck consisted of two parallel sections separated by 6 in., each carrying four traffic lanes and two shoulders; the overall deck width was therefore113 ft., 4 in. The deck was supported by 14 I-shaped longitudinal stringers, 27-in. deep, spaced at 8 ft. - 2 in. (see Figure 2.1-2). The initial minimum deck thickness was 6.5 inches in 1967 and the average thickness had increased to about 8.5 in. due to a 1992 retrofit. Longitudinal expansion joints were located in the deck above main truss nodes 4, 8, 14, 8’ and 4’.

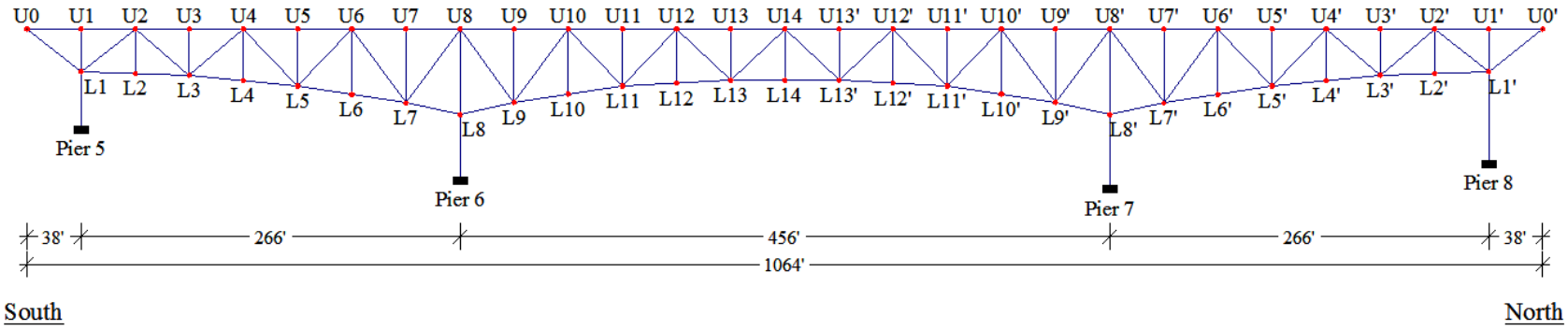

Figure 2.1-1: Typical main deck truss elevation, looking west

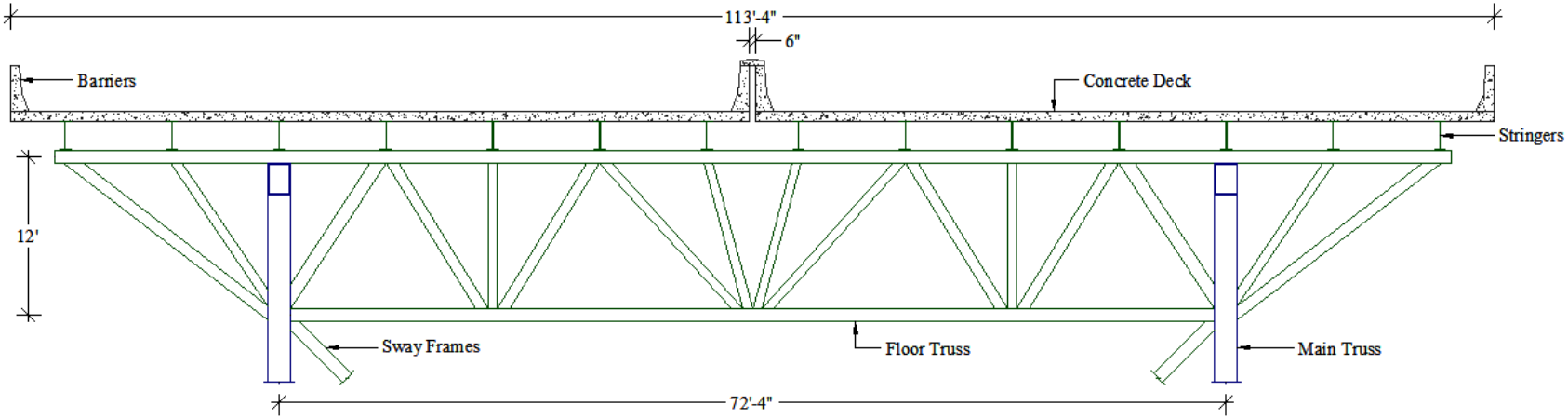

Figure 2.1-2: Typical cross-section of the deck truss portion

The overall bridge had 14 spans supported by 13 piers and 2 abutments. Eleven of these spans were approach spans to the deck truss portion, five to the south side and six to the north side. The main trusses were supported at piers 5, 6, 7, and 8 and were labeled spans 6, 7 and 8 of the overall bridge. Short cantilevers supported a portion of approach spans 5 and 9. To accommodate longitudinal thermal expansion, fixed bearings were located at pier 7, and roller bearing at piers 5, 6, and 8 (see figure 2.1-3).

Figure 2.1-3: Expansion roller bearings at pier 5, looking east
(Source: NTSB)

The upper and lower chords, vertical and diagonal members of the main trusses designed for compression were built-up box members. The east and west plates of the box members are designated as “side plates”, and the top and bottom plates as “cover plates”. All box members had access holes in both cover plates, except for the top chord members, which had blind cover plates at the top because there was a longitudinal stringer located directly above the truss chords.

The vertical and diagonal members designed primarily for tension forces were built-up H-shaped members with flanges on the east and west sides welded to a web plate. All main truss members were 21 inches wide measured in the east-west direction. The main truss members were connected at the nodes by riveted steel gusset plates similar to the one shown in Figure 2.1-4.

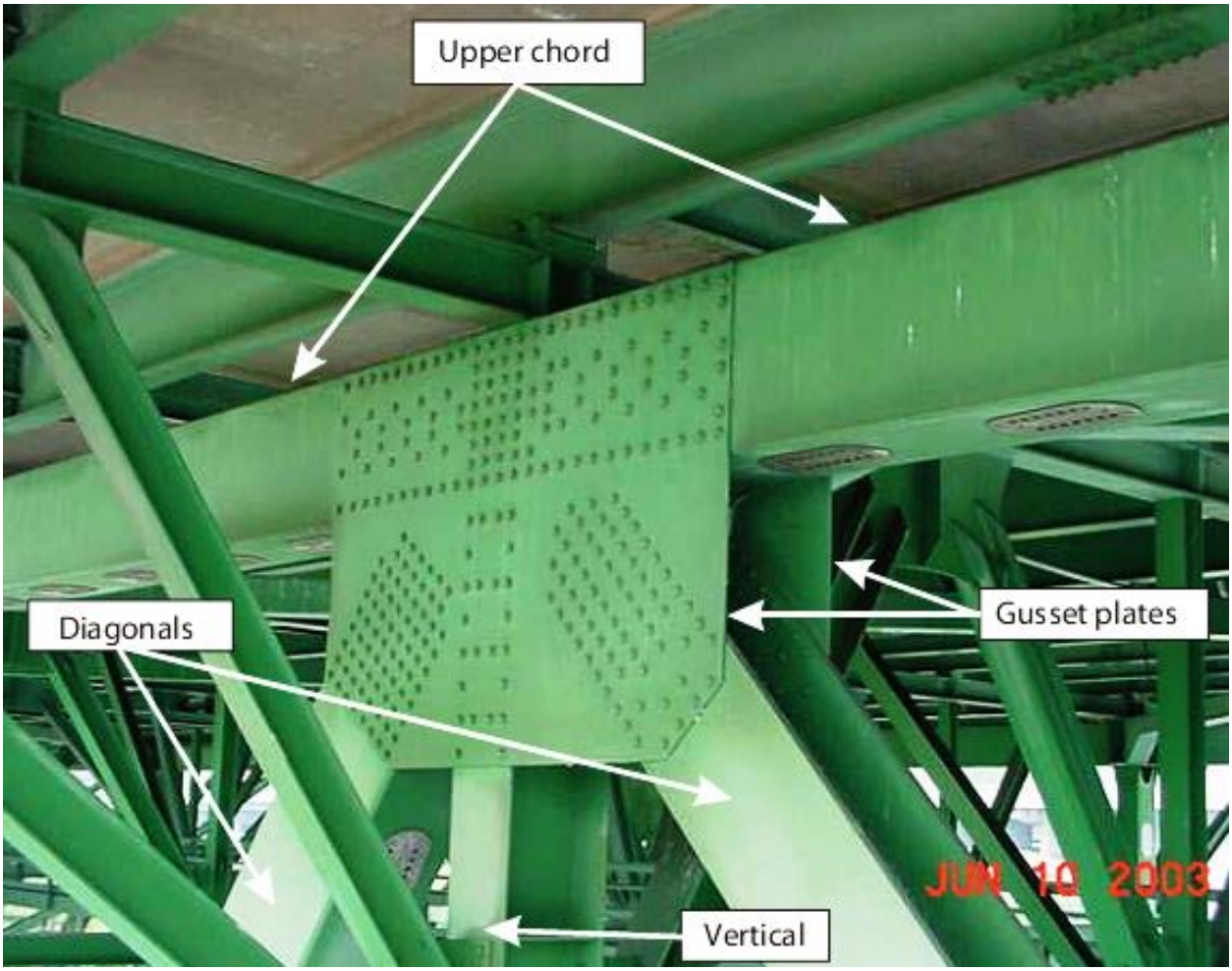

Figure 2.1-4: Typical five-member connection of the main trusses
(Source: NTSB)

2.2 Collapse summary

The main truss portion of the I-35W highway bridge collapsed on August 1, 2007 about 6:05 p.m. central daylight time (NTSB, 2008). Photographic evidence from the day of the collapse event and post-collapse observations of the wreckage show that the bridge collapsed under the combined effect of self-weight, vehicle traffic, and construction loads. Deck resurfacing work was underway the day of the collapse. Construction equipment and piles of aggregate were positioned on the deck directly over nodes U10 that was found to be the initiation point for the collapse (see Figure 2.2-1).

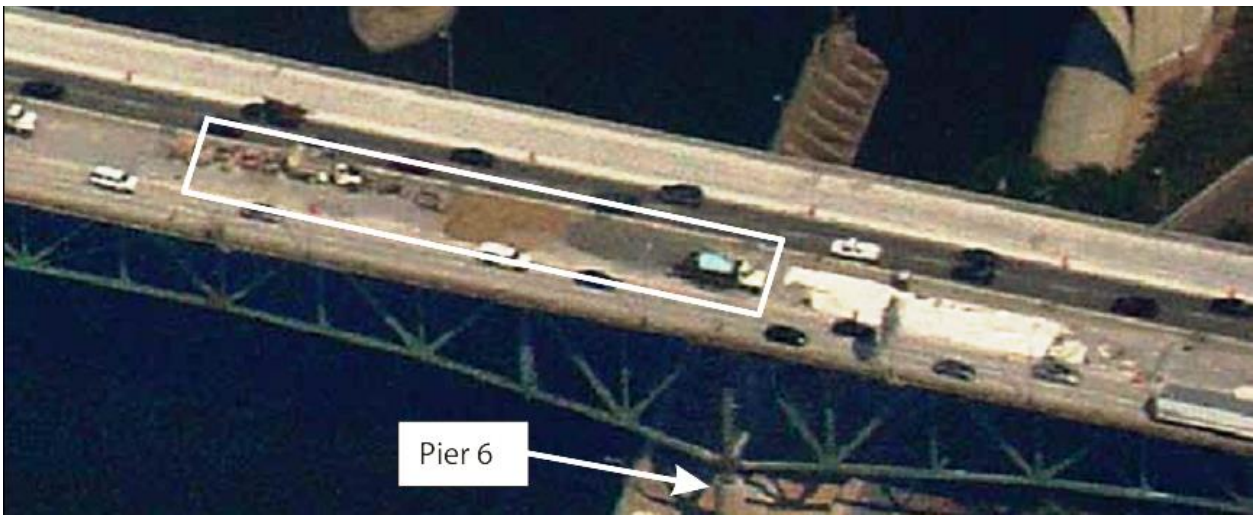

Figure 2.2-1: Construction equipment and aggregates about 2:15 hours before the collapse. (Enlargement of photograph taken by a passenger in a commercial airliner. Source: NTSB)

The main truss portion of the bridge separated into three sections during the collapse (see Figure 2.2-2). Most of the center section, between piers 6 and 7, fell into the river. The north and south sections fell onto land (NTSB, 2008). Video footage shows that the collapse started at the south end of the center span and progressed toward the north end of the center span. The center section remained relatively level in the east-west direction as it was falling, indicating that collapse of the east and west trusses occurred simultaneously.

Most of the inelastic behavior occurred between nodes 8 and 11 at both ends of the center span, specifically in the upper chord between nodes U8 and U10, and in the lower chord between nodes L9 and L11; these are henceforth called the fracture areas.

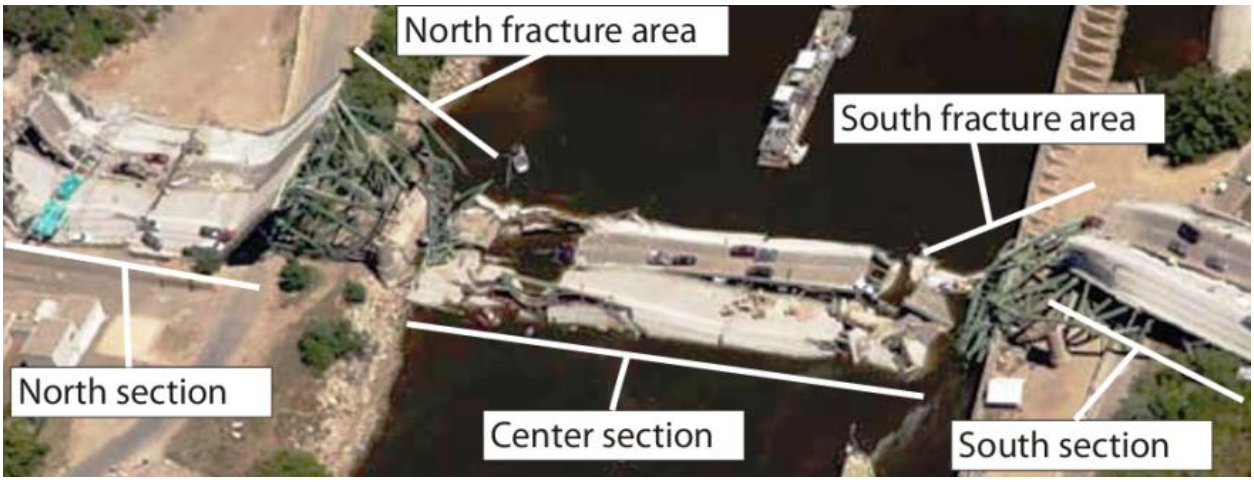

Figure 2.2-2: Collapsed deck truss north, center, and south sections of the bridge (Source: NTSB)

2.3 Probable cause of the collapse

After exhaustive investigation, the NTSB concluded that the cause of collapse of the I-35W Highway Bridge was inadequate load capacity of the gusset plates at the U10 and U10' truss nodes. The gusset plates, shown on the bridge plans, were approximately half the thickness needed for a proper design. The reasons for the inadequate design are not exactly known, but there was some breakdown in the design process. Other major safety issues were identified including: “insufficient bridge design firm quality control procedures for designing bridges, and insufficient Federal and State procedures for reviewing and approving bridge design plans and calculations, lack of guidance for bridge owners with regard to the placement of construction loads on bridges during repair or maintenance activities, exclusion of gusset plates in bridge load rating guidance, lack of inspection guidance for conditions of gusset plate distortion, and

inadequate use of technologies for accurately assessing the condition of gusset plates on deck truss bridges" (NTSB, 2008).

The NTSB also considered many other causes and possible collapse scenarios and concluded that "the following were neither causal nor contributory to the collapse of the I-35W bridge: corrosion damage found on the gusset plates at the L11 nodes and elsewhere, fracture of a floor truss, pre-existing cracking in the bridge deck truss or approach spans, temperature effects, or shifting of the piers" (NTSB, 2008). Therefore, the discarded causes and scenarios were not considered in this research.

2.4 Loads on the bridge

The total load on the deck truss portion of the bridge at the time of collapse included the dead load (weight of the structural steel, concrete deck, concrete barriers, inspection walkways, and the additional weight of the retrofitted concrete deck and barriers), construction equipment and materials, traffic vehicles, and pedestrians. These loads are described as follows:

- **Steel Structure:** The weight of the steel structure is taken as the weight reported in the construction plans and shop drawings (as-built weight). The dimensions shown on the plans were verified through measurements of the wreckage. Since the structural model does not account for the weight of miscellaneous components (stiffener plates, welds, paint, bolts, etc.), the base steel density of $490\ lb/ft^3$ was adjusted in the model to match the as-built weight.
- **Concrete Deck:** During the post-collapse investigation, cores were sampled from the deck at various locations to measure the deck thickness and concrete density. It was

determined that the original concrete deck had a density of $160\ lb/ft^3$ and thickness of 6.5 inches, and the additional 2 in. of concrete added in the retrofit had a density of $140\ lb/ft^3$ (Ocel & Wright, 2008).

- **Concrete Barriers:** The weight of the original concrete barriers was estimated as $516\ lb/ft$ for the exterior barriers and $507\ lb/ft$ for the interior barrier, and the retrofitted barriers were estimated as $778\ lb/ft$ for the exterior barriers and $1{,}055\ lb/ft$ for the interior barrier (Ocel & Wright, 2008).
- **Inspection walkways:** There were four catwalks for bridge inspections: one walkway runs longitudinally to the bridge, located 26 ft. -3 in. from the west truss and is supported by the bottom chords of the floor trusses; and three walkways that run transverse to the bridge at floor trusses 8, 10 and 8'. The weights were estimated as $108.6\ lb/ft$ for the longitudinal and $117.4\ lb/ft$ for the transverse walkways (Ocel & Wright, 2008).
- **Construction and traffic loads:** Location of vehicles, construction equipment and materials were determined using post-collapse locations, photographic evidence and witness statements. Vehicles weights were estimated using calibrated cranes and portable scales. Vehicle occupants and pedestrians were assigned an average weight based on the age range. The weights of construction materials were estimated based on photographic evidence and statements of construction workers. Detailed information is reported by the NTSB (Morrison, Brazy, & Schultheisz, 2007).

The loads are applied to the structural model in four load stages to represent the accumulation of loading over time. Stage 1 includes the self-weight of the components before the concrete deck hardens, Stage 2 includes the dead loads applied after the concrete deck hardens, Stage 3 adds the additional concrete weight from retrofits over the life of the structure, and Stage

4 applies the live loads and construction loads present on the day of collapse. The loads added at each stage are listed as follows:

- **Stage 1:** self-weight of the steel structure, inspection walkways and concrete deck.
- **Stage 2:** weight of the concrete barriers.
- **Stage 3:** additional weights of the retrofitted concrete deck and barriers.
- **Stage 4:** construction and traffic loads.

2.5 Approach spans

The approach spans were connected to the ends of the main trusses through rocker bearings at nodes U0 and U0'. A portion of the approach span weight and live loads are transmitted to the deck trusses through these bearings. Since the approaches were multi-span continuous units, the approach span stiffness affected load transfer to the truss span. The Federal Highway Administration (FHWA) developed separate models of the approach spans to determine equivalent forces and springs that simulate the approach span effect. (Ocel & Wright, 2008). The results are summarized in Table 2.5-1.

Table 2.5-1: Approach spans - equivalent reactions and stiffness

Location	**Stiffness (kip/in)**	**Reaction (kip)**			
		Stage 1	**Stage 2**	**Stage 3**	**Stage 4**
SE Corner (node U0 E)	7.05	160.5	160.5	200.7	207.7
NE Corner (node U0' E)	5.00	446.8	446.8	543.0	547.9
SW Corner (node U0 W)	9.45	196.5	196.5	245.1	249.8
NW Corner (node U0' W)	2.95	451.7	451.7	553.1	565.9
Total		**1,345.5**	**1,345.5**	**1,541.9**	**1,571.3**

The total loads applied to the deck truss portion of the bridge include both the weight estimates described in Section 2.4 and the equivalent approach spans reactions listed in this section. The best estimate of total load present at the time of collapse is itemized in Table 2.5-2.

Table 2.5-2: Total loads on the deck truss portion of the bridge

Component	**Load Estimate (kip)**	**Percentage (%)**
Steel structure	6,322.9	25.1
Original concrete deck	10,342.7	41.0
Original concrete barriers	1,628.0	6.5
Additional concrete deck	3,139.0	12.4
Additional concrete barriers	1,132.6	4.5
Inspection walkways	136.9	0.5
Construction	385.0	1.5
Traffic	574.9	2.3
Approach spans reactions	1,571.3	6.2
Total	**25,233.3**	**100.0**

As discussed in the FHWA report, the total dead load applied to the full model may be up to $300\ kip$ lighter than the estimates because of all the sources of uncertainty (Ocel & Wright, 2008). In addition, the NTSB estimates a potential error of plus/minus 5 percent in the construction and traffic loads, which is equivalent to $\pm 48\ kip$ in the full model (NTSB, 2008).

CHAPTER 3. DEVELOPMENT OF ANALYSIS MODELS

The results of this research are obtained from structural analysis using the software *SAP2000* version 14 (CSI, 2009). First, a full three-dimensional model was created and calibrated to field data obtained by University of Minnesota (UOM) in a fatigue evaluation of the bridge in 2001 (O'Connell, Dexter, & Bergson, 2001). Second, a simplified two-dimensional trusses model was developed to study the collapse mechanism. Point loads and springs were used to represent the weights and stiffness of the removed elements. The reactions and axial forces at the U10 nodes in both models were used to validate the simplified 2D model. The base model used for this research was simplified further to a single two-dimensional truss. This simplification is justified since the video footage of the collapse shows that both trusses failed almost simultaneously and therefore similar behavior of both trusses may be assumed. The west truss was selected because the construction and traffic loads were shifted towards the west side of the bridge creating greater member forces in the west truss.

Nonlinear connection behavior was incorporated into the base model using Nonlinear Links and Frame Hinges properties. Nonlinear Links are used at the upper end of the L9-U10 members to model buckling behavior of the U10 gusset plates. The buckling capacity was determined by Finite Element Analysis (FEA) using Nonlinear Shell elements with applied notional loads to simulate the effect of initial imperfections. Equivalent Frame Hinges were determined by performing fiber analysis of cross-sections, the frame hinges were calibrated and validated by FEA, and then were assigned to the mid and end-points of chord members U8-U10 and L9-L11 which are directly above and below the L9-U10 diagonals.

3.1 3D Model and Calibration

The full three-dimensional model was created to calibrate the boundary conditions of the bridge to the influence lines reported by the UOM (O'Connell, Dexter, & Bergson, 2001) and to analyze the load transfer from the floor trusses to the main trusses. The geometry of the model is based on the General Management Plan, Elevations & Sections (Allied Structural Steel Company, 1966) and T.H. 35W State of Minnesota Department of Highways, Bridge no. 9340 Design Drawings (Sverdrup & Parcel and Associates, Inc., 1965). The material mechanical properties used are as reported by the FHWA in (Beshah, Wright, & Graybeal, 2008) and (Graybeal, 2008).

The model incorporates all the bridge elements: concrete deck, longitudinal stringers and their cross frames, floor trusses, main trusses, vertical and horizontal sway frames, concrete piers, and stiffness of the approach spans. Frame elements (beam elements) were used to model the entire steel structure and the columns of the concrete piers. The concrete deck, spandrels, and walls of the concrete piers were modeled using Shell elements. Link elements were used to connect the stringers to the floors trusses and Joint Springs to model the stiffness of the approach spans (see Figures 3.1-1 and 2).

All the main trusses members were welded, built-up box or H-shape sections. These were modeled plate-by-plate using the Section Designer tool of SAP2000. The upper and lower chords, verticals, and diagonal members, designed primarily for compression, were box-shape members with access holes in both cover plates. The exception is the top chord members with blind cover plates at the top.

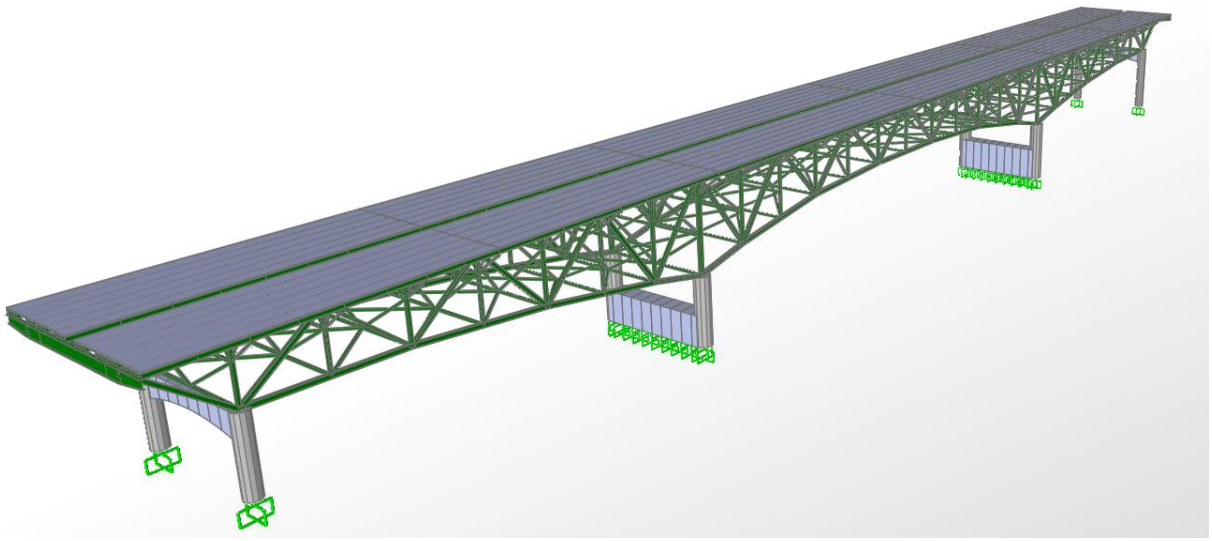

Figure 3.1-1: Extruded view of the 3D model, looking down to northwest

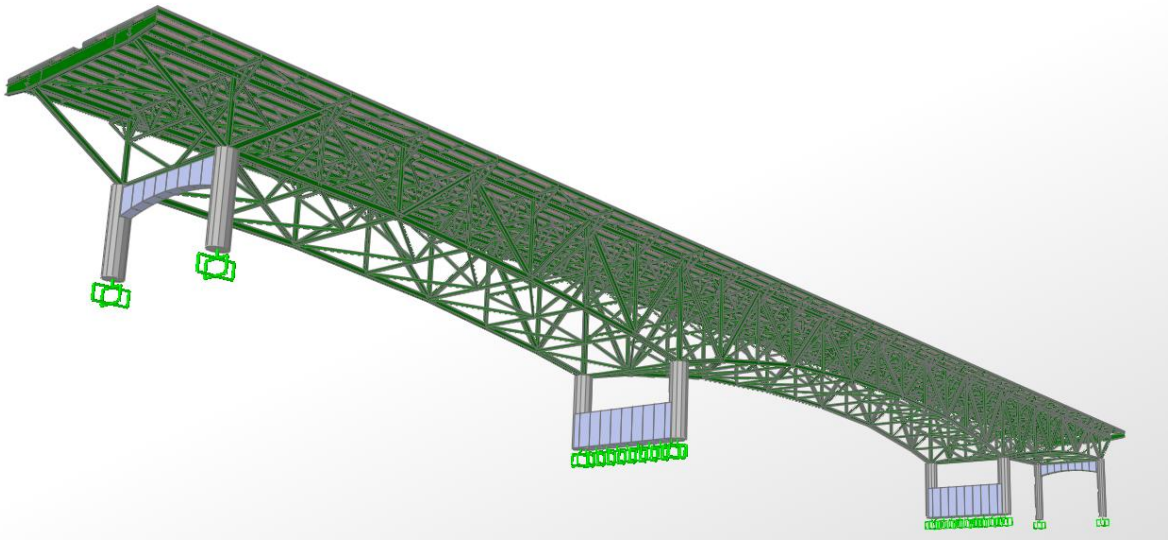

Figure 3.1-2: Extruded view of the 3D model, looking up to northwest

Only one cross section can be assigned to a single Frame element. The cover plate holes create section property variations along the length of the members. Therefore, the frame element properties need to be somewhere between the gross and net cross-sectional properties. Since the truss behavior is mainly in plane, torsion in individual members is negligible and the model can be simplified to a single two-dimensional truss, the stresses in the cover plates are longitudinal and therefore, the cover plates can be idealized as solid plates with an effective thickness that provides the equivalent longitudinal stiffness.

The effective thickness of the cover plates was determined by performing FEA on two plates of the same width, length, and boundary conditions. One of the plates had access holes and the other was a solid plate. The same axial force was applied to both plates and the thickness of the solid plate was changed until its axial displacement matched that of the plate with the access holes (see Figure 3.1-3). The results show that a factor of 0.5984 can be applied to the cover plates with access holes to obtain a solid plate with equivalent longitudinal stiffness.

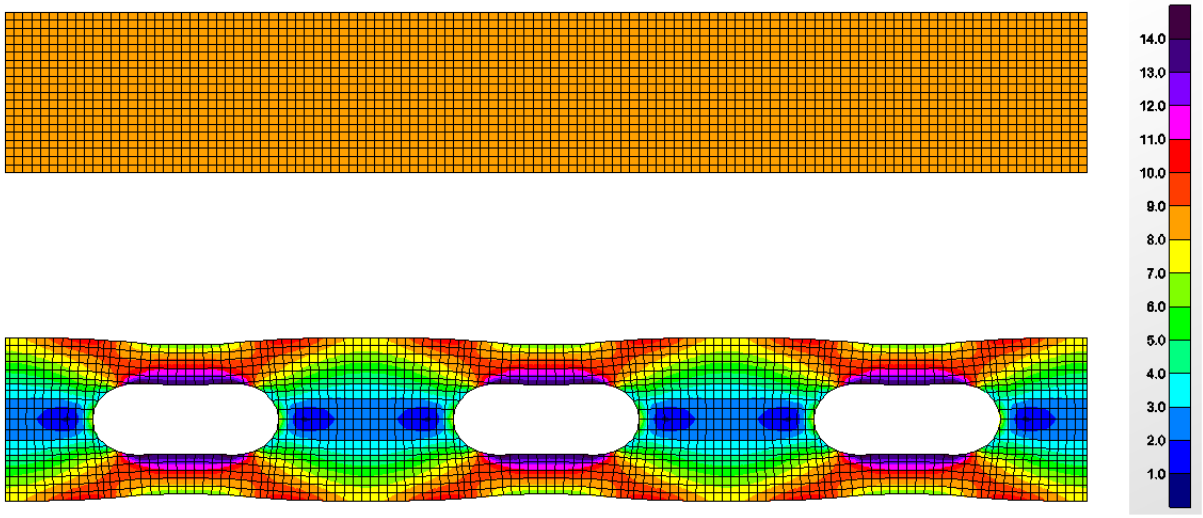

Figure 3.1-3: Von Mises stresses (ksi) plotted on the deformed shape of the cover plates solid plate (top) and plate with access holes (bottom)

The verticals and diagonals that were designed primarily for tension forces consisted of built-up H-shaped members with flanges on the east and west sides welded to a web plate. The vertical members at piers 6 and 7, U8-L8 and U8'-L8', were built-up box members. These carry the largest axial compression forces and had an additional web plate welded to the side plates to provide additional strength. All the plates in the main truss members were modeled at their centroid location and the effective thickness factor was applied to the cover plates where applicable. Typical cross sections are shown in Figure 3.1-4.

The concrete deck, defined as a membrane element to neglect the out-of-plane stiffness, was supported by the longitudinal stringers. Link elements were used to connect the stringers to the floor trusses with the corresponding eccentricity and boundary conditions. Since the stringers were discontinuous and allowed to move longitudinally relative to each other at the deck expansion joint locations and the stringers directly above the main trusses had longitudinal discontinuity at every node, the composite action between the main trusses and the deck is negligible. All the floor truss elements were fully connected by welds and were modeled with fixed connectivity. The floor trusses were connected to the main trusses by rivets. The riveted connections between the main trusses members were modeled as fixed because it is closer to reality than pin connections. The analysis results show that the axial force eccentricity in these members is small.

The steel structure weight was automatically calculated by SAP2000. Since the structural model does not account for the weight of miscellaneous parts (stiffener plates, welds, paint, etc.), the steel density of $490\ lb/ft^3$ was adjusted to $560.7\ lb/ft^3$ to better match the as-built weight.

The weight of the concrete deck was applied as a uniform area load, the barriers were applied as line loads, and the inspection walkways were applied as point loads and line loads (for the longitudinal and transverse walkways respectively) on the bottom chords of the floor trusses. The construction and traffic loads were simplified to point loads that are applied on the upper chord nodes of the main trusses. The approximate weights and locations of each component over the deck are given in the Report No. 07-115 by NTSB (Morrison, Brazy, & Schultheisz, 2007). Two-way lever rule was used to convert the deck loads to the main truss point loads. The resulting point loads are shown in Table 3.1-1.

The model was calibrated to field data obtained by University of Minnesota (UOM) during a fatigue evaluation of the bridge in 2001 (O'Connell, Dexter, & Bergson, 2001). Four tests were performed with different truck configurations consisting of nine tandem-axle dump trucks. Test 4 was selected to calibrate the model because it provided the most consistent results among the four. In this test, the trucks were run along the bridge at highway speed in groups of three, one group at a time. Strain gauges recorded the strain history in the main trusses diagonals, upper chords, and lower chords between nodes 9 and 10. The strains are then elastically converted to stresses.

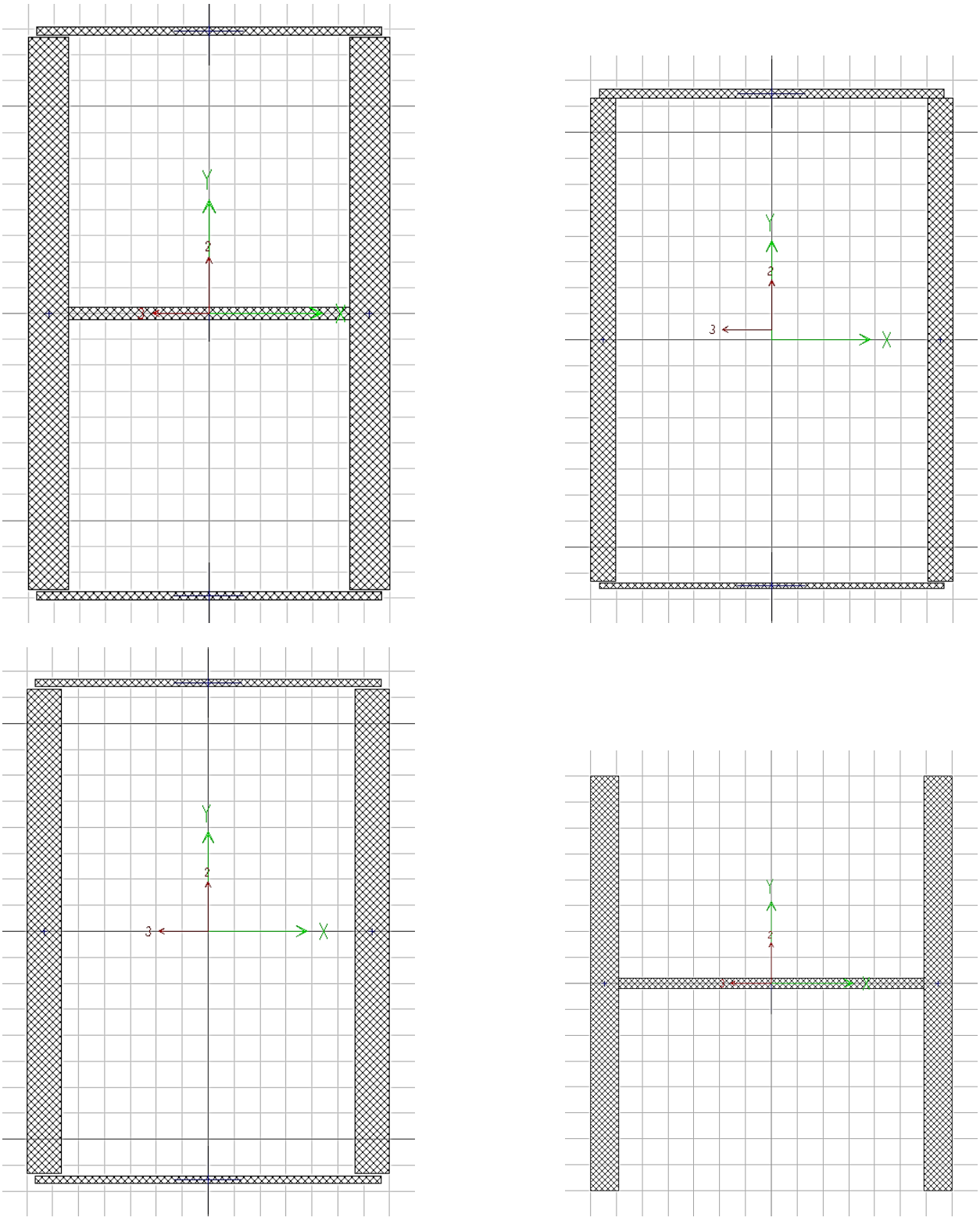

Figure 3.1-4: Typical cross sections of the main trusses members
U8-L8 (top left), U8-U10 (top right), L9-U10 (bottom left) and U10-L11 (bottom right)
(Grids 1.5 by 1.5 inches)

Table 3.1-1: Construction and traffic point loads distribution on main trusses (kip)

Node	Traffic Loads		Construction Loads		Node	Traffic Loads		Construction Loads	
	East	West	East	West		East	West	East	West
U0	-5.83	-6.31	0.00	0.00	**U13'**	-1.41	-7.53	0.00	0.00
U1	-5.51	-43.83	0.00	0.00	**U12'**	-4.05	-7.35	0.00	0.00
U2	-0.21	-43.60	0.00	0.00	**U11'**	-2.75	-9.12	0.00	0.00
U3	-5.51	-6.83	0.00	0.00	**U10'**	-2.09	-4.97	0.00	0.00
U4	-5.66	-21.35	0.00	0.00	**U9'**	-1.70	-4.57	0.00	0.00
U5	-5.51	-19.63	0.00	0.00	**U8'**	-0.68	-2.49	0.00	0.00
U6	-5.97	-4.18	0.00	0.00	**U7'**	0.69	-6.92	0.00	0.00
U7	-3.91	-1.55	-0.11	-0.14	**U6'**	-2.43	-6.02	0.00	0.00
U8	-2.82	-4.48	0.00	0.00	**U5'**	-2.02	-5.47	0.00	0.00
U9	-1.60	-4.31	-64.40	-110.28	**U4'**	-2.44	-6.01	0.00	0.00
U10	-3.44	-8.82	-36.60	-59.44	**U3'**	-2.44	-3.29	0.00	0.00
U11	-10.17	-43.93	-43.03	-69.46	**U2'**	-0.62	-2.74	0.00	0.00
U12	-23.69	-71.11	0.00	0.00	**U1'**	-6.04	-14.75	0.00	0.00
U13	-16.49	-54.59	-0.38	-0.55	**U0'**	-3.46	-8.26	0.00	0.00
U14	-5.32	-17.80	-0.23	-0.34					

To calibrate the model, the stress histories were converted to axial forces to create influence lines for the members. Two different boundary conditions were considered: (1) the ideal pin and rollers (called “rollers”); and the “piers” boundary condition that assumed the rollers were locked and the longitudinal bridge movement caused bending of the piers. The stiffness of the concrete piers was modified to account for cracking that was observed in the field. The influence lines for the center span (between piers 6 and 7), shown in Figures 3.1-5 to 10, indicate that the locked “piers” boundary condition provides the closest agreement to the UOM data.

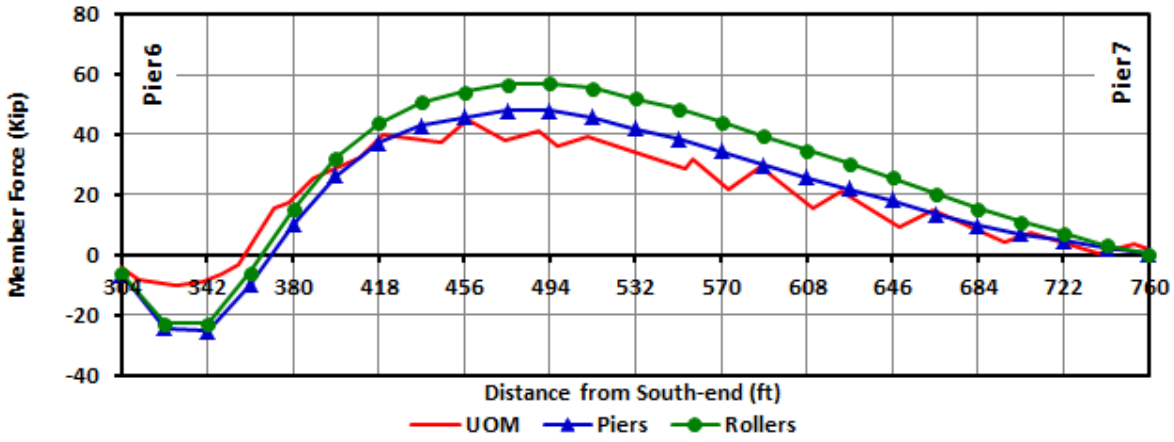

Figure 3.1-5: Influence lines for calibration of upper chord member U8-U10 West

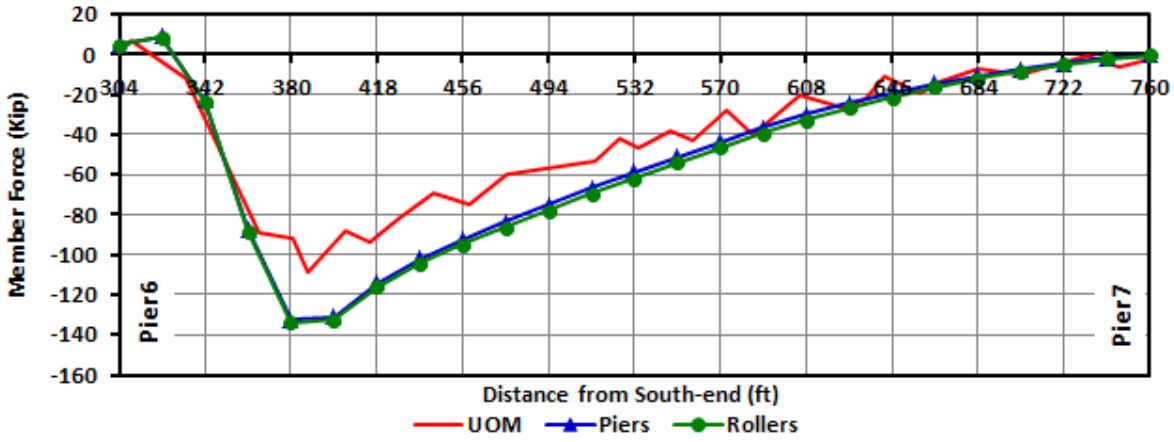

Figure 3.1-6: Influence lines for calibration of diagonal member L9-U10 West

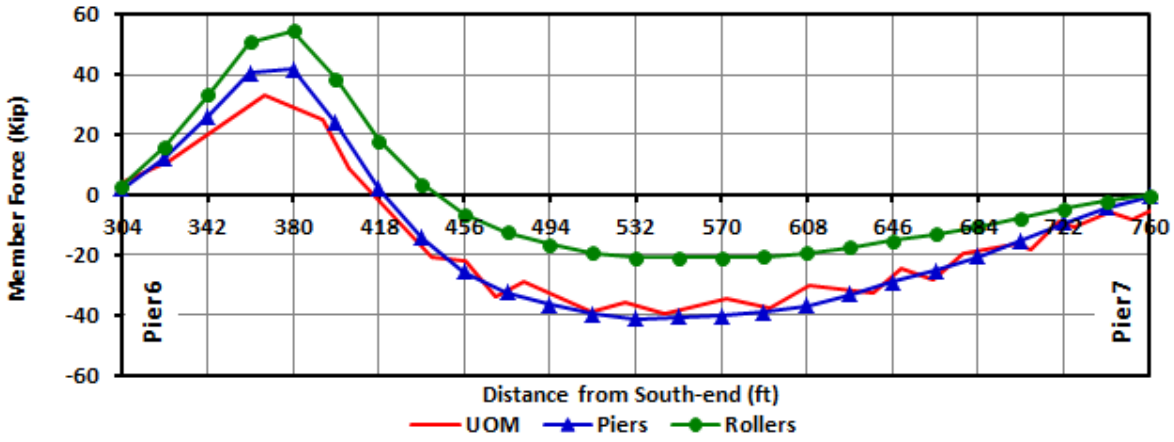

Figure 3.1-7: Influence lines for calibration of lower chord member L9-L11 West

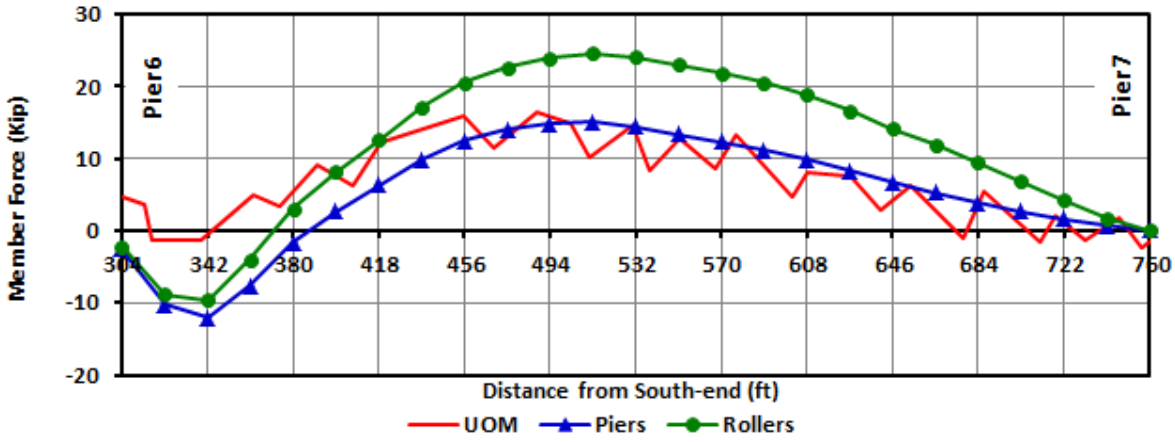

Figure 3.1-8: Influence lines for calibration of upper chord member U8-U10 East

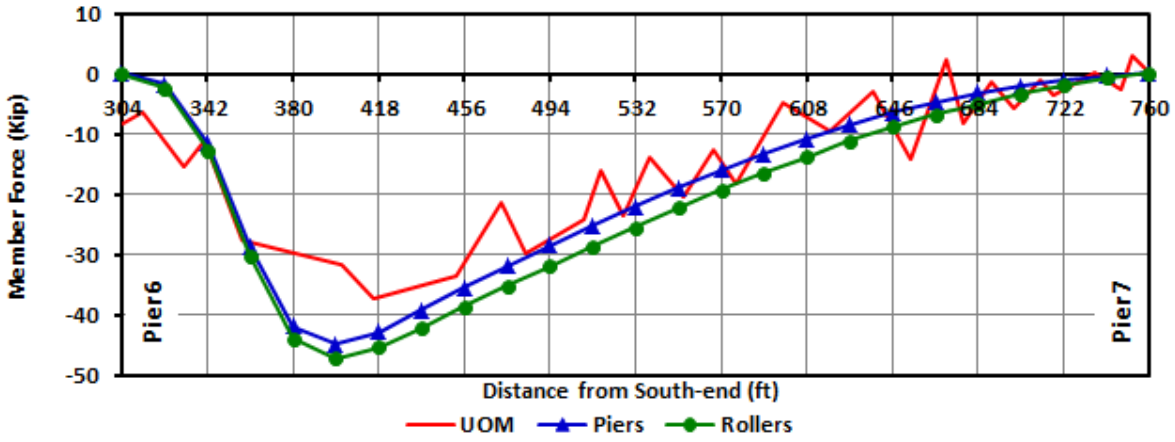

Figure 3.1-9: Influence lines for calibration of diagonal member L9-U10 East

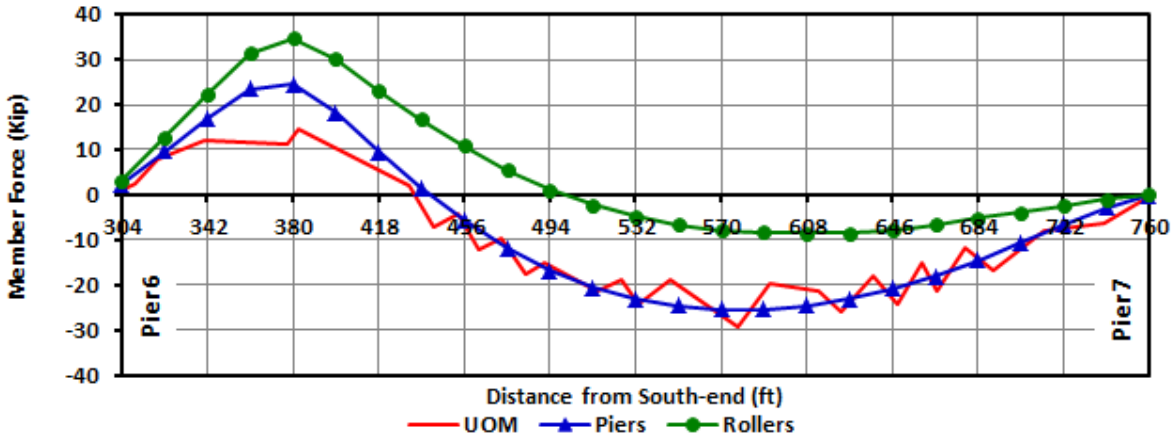

Figure 3.1-10: Influence lines for calibration of lower chord member L9-L11 East

3.2 2D Model and Validation

The calibrated full three-dimensional model was simplified to a two-dimensional truss model to improve computational efficiency. The weights of the removed members were converted to point loads placed at the main truss nodes. The self-weight of the stringers, floor beams, trusses, and the area loads representing the weight of the concrete deck were converted to point loads based on the tributary area concept. The point loads from the longitudinal inspection walkways were transferred to the main trusses using the lever rule and the line loads from the transverse walkways were transferred based on the tributary width of the main trusses. The line loads representing the concrete barriers were converted using the tributary length between the main truss nodes.

To better approximate the element forces, the point loads were split between the nodes where the top and bottom chords of the floor trusses connected to the main trusses. The distribution factors were determined using the Section Cut Forces output of SAP2000 and are presented in Figure 3.2-1. Intermediate nodes, designated with "M", were created to input the loads transferred from the bottom of the floor trusses to the main trusses.

The concrete piers were replaced by rollers and horizontal springs in the two-dimensional model. Since the NTSB concluded that pier shifting did not contribute to the collapse (NTSB, 2008), these were modeled as linear springs. Elevation views of the west main truss of both models are shown in Figures 3.2-2 and 3.

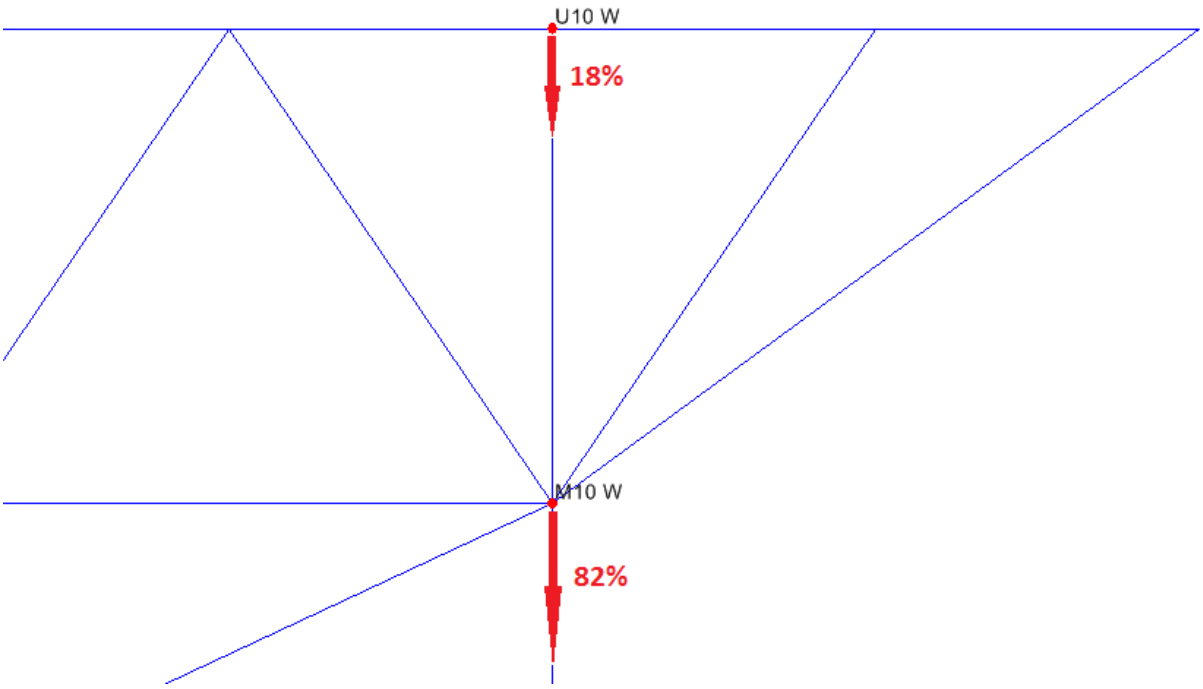

Figure 3.2-1: Elevation of a floor truss segment showing the distribution of the point loads

The support reactions were compared between the 2D and 3D models. The axial forces in the members connected to node U10 are of special interest since the collapse initiated there. These forces were compared between the two models and the results are summarized in Tables 3.2-1 and 2. The maximum difference is 2 percent for the support reactions, 6 percent in the member axial forces at the end of Stage 4, and only 1 percent for critical L9-U10 diagonal. The accuracy of these comparisons validates the simplified two-dimensional model.

The base model for this research consists of a single two-dimensional truss because the video footage shows that the center section remained relatively level in the east-west direction as it was falling (NTSB, 2008). Therefore, there is no twisting of the structure and both trusses will deform in the same modes. The west main truss was selected for the base model because the construction and traffic loads were shifted towards the west side of the bridge, as shown in Figure 2.2-1.

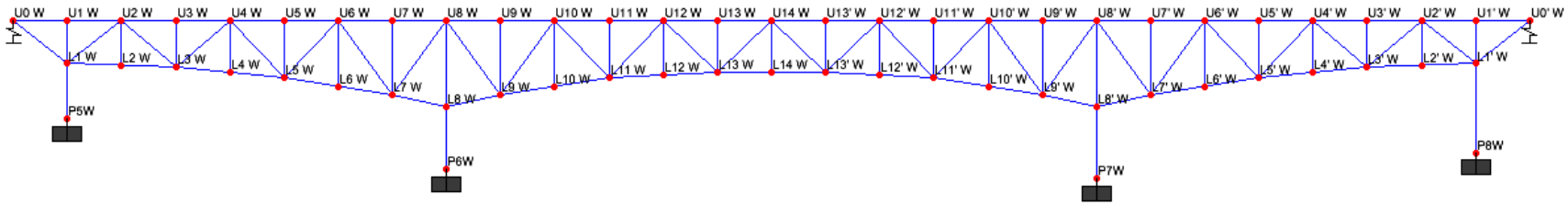

Figure 3.2-2: Main west deck truss elevation of the 3D model, looking west

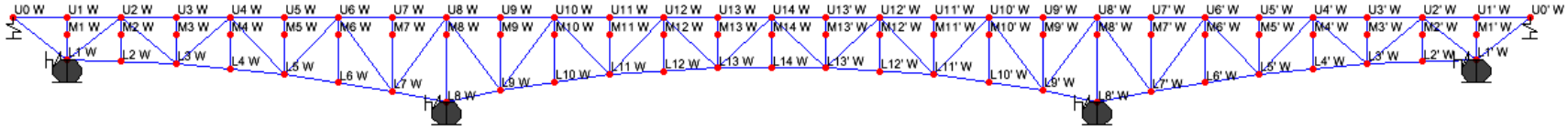

Figure 3.2-3: Main west deck truss elevation of the 2D model, looking west

Table 3.2-1: Main truss reactions of the 3D and 2D models (kip)

Location	Stage 1			Stage 2			Stage 3			Stage 4		
	3D Model	2D Model	Ratio	3D Model	2D Model	Ratio	3D Model	2D Model	Ratio	3D Model	2D Model	Ratio
P5E	982	992	1.01	1,068	1,079	1.01	1,341	1,352	1.01	1,333	1,356	1.02
P5W	1,024	1,036	1.01	1,110	1,122	1.01	1,392	1,406	1.01	1,459	1,459	1.00
P6E	3,371	3,361	1.00	3,692	3,682	1.00	4,529	4,517	1.00	4,761	4,736	0.99
P6W	3,379	3,366	1.00	3,700	3,686	1.00	4,535	4,520	1.00	4,990	4,989	1.00
P7E	3,300	3,287	1.00	3,620	3,608	1.00	4,443	4,430	1.00	4,503	4,487	1.00
P7W	3,312	3,299	1.00	3,633	3,620	1.00	4,455	4,441	1.00	4,605	4,593	1.00
P8E	1,335	1,347	1.01	1,422	1,434	1.01	1,761	1,774	1.01	1,766	1,784	1.01
P8W	1,346	1,357	1.01	1,432	1,444	1.01	1,777	1,791	1.01	1,805	1,814	1.00
Total	**18,049**	**18,047**	**1.00**	**19,678**	**19,675**	**1.00**	**24,234**	**24,231**	**1.00**	**25,221**	**25,218**	**1.00**

Table 3.2-2: Axial Forces at nodes U10 of the 3D and 2D models (kip)

Member	Stage 1			Stage 2			Stage 3			Stage 4		
	3D Model	2D Model	Ratio	3D Model	2D Model	Ratio	3D Model	2D Model	Ratio	3D Model	2D Model	Ratio
U8-U10 E	1,231	1,254	1.02	1,356	1,381	1.02	1,677	1,707	1.02	1,711	1,730	1.01
U8-U10 W	1,233	1,253	1.02	1,358	1,380	1.02	1,679	1,704	1.02	1,769	1,796	1.02
L9-U10 E	-1,536	-1,534	1.00	-1,685	-1,682	1.00	-2,076	-2,072	1.00	-2,244	-2,212	0.99
L9-U10 W	-1,541	-1,540	1.00	-1,689	-1,688	1.00	-2,080	-2,078	1.00	-2,375	-2,392	1.01
U10-L10 E	218	229	1.05	244	254	1.04	306	318	1.04	312	319	1.02
U10-L10 W	218	230	1.05	245	255	1.04	307	319	1.04	315	320	1.02
U10-L11 E	1,251	1,285	1.03	1,371	1,408	1.03	1,688	1,731	1.03	1,806	1,828	1.01
U10-L11 W	1,254	1,290	1.03	1,374	1,412	1.03	1,691	1,736	1.03	1,904	1,985	1.04
U10-U12 E	-545	-547	1.00	-591	-593	1.00	-720	-722	1.00	-874	-849	0.97
U10-U12 W	-547	-554	1.01	-593	-601	1.01	-722	-731	1.01	-945	-998	1.06

3.3 Detailed U10 Connection

A refined analysis of the connection at node U10 is of special interest because the NTSB concluded that the collapse of the I-35W Highway Bridge was probably a result of inadequate load capacity of the gusset plates at these nodes (NTSB, 2008). It was determined that the 0.5 in. gusset plate thickness was about half of what would be required for a proper design. The general opinion is that the portion of the gusset plates connecting the upper end of the L9-U10 diagonal member buckled out of plane thereby triggering the collapse sequence.

Starting from the base two-dimensional model, the main truss members at node U10 were disconnected from the node and the end-point was defined at the actual location according the shop drawings (Allied Structural Steel Company, 1966). The top chord members of the main truss at node U10 were connected with Gap elements that only transfer compression forces (see Figure 3.3-1). The gusset plates connecting the side plates and flanges together and the smaller plates connecting the cover plates of the top chord members were discretely modeled using Nonlinear Layered Shell elements in SAP2000 (CSI, 2009). The individual Frame elements were connected to the corresponding joints of the shell element mesh using Body Constraints at the rivet locations (see Figure 3.3-2). This ignores any possible slip between the connected plates. The rivet holes were not discretely modeled because they have little effect on the buckling capacity of the gusset plates. All six degrees of freedom were activated to allow the full shell behavior of the gusset plates. Out-of-plane restraints were added to the main truss nodes where the sway frames, the top and bottom chords of the floor trusses connected to the main trusses (see Figure 3.3-3).

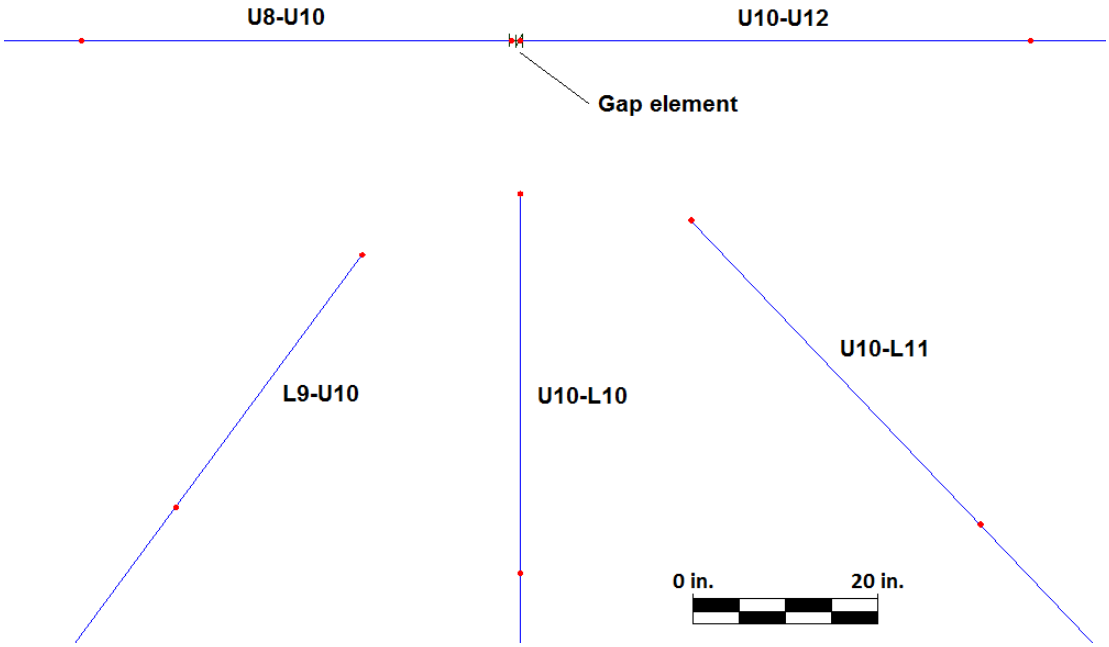

Figure 3.3-1: Main truss members at node U10 in the "Detailed U10 Connection" model

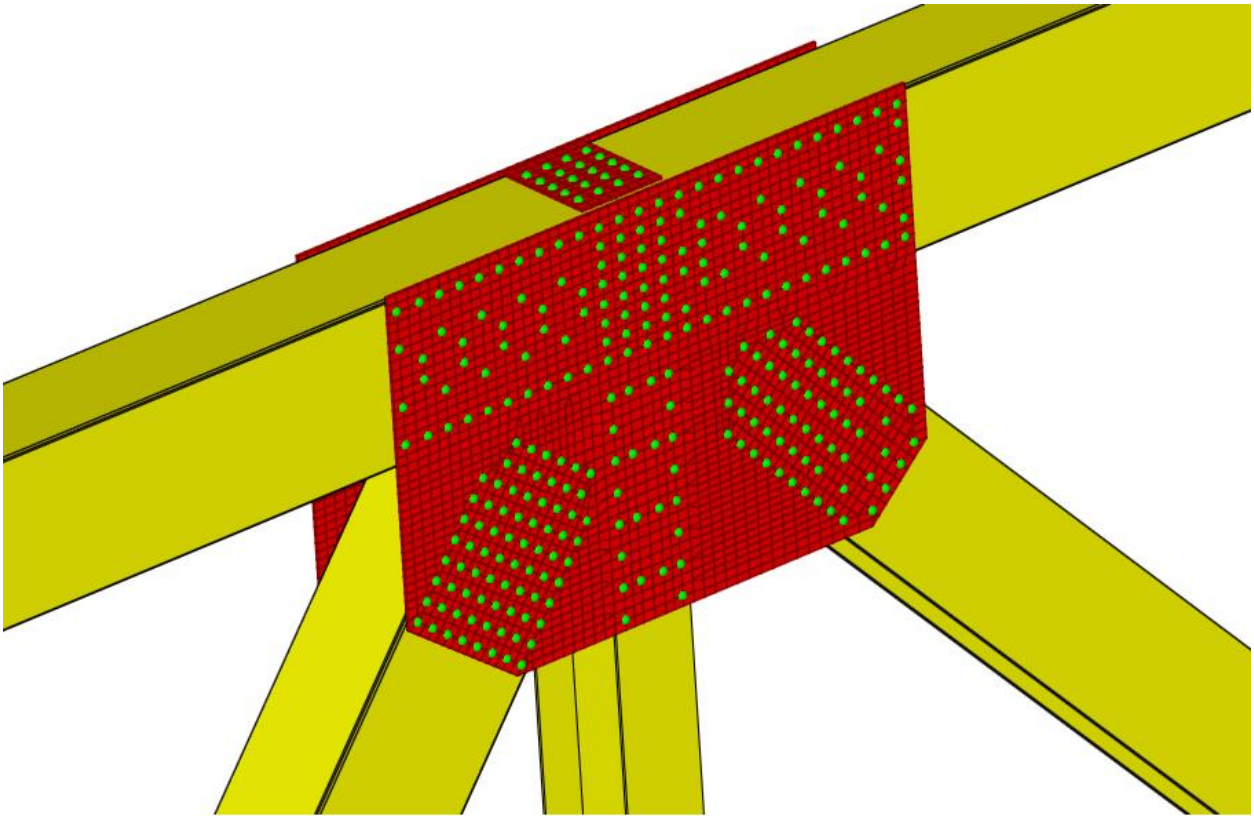

Figure 3.3-2: Extruded view of detailed U10 connection, looking down to northwest

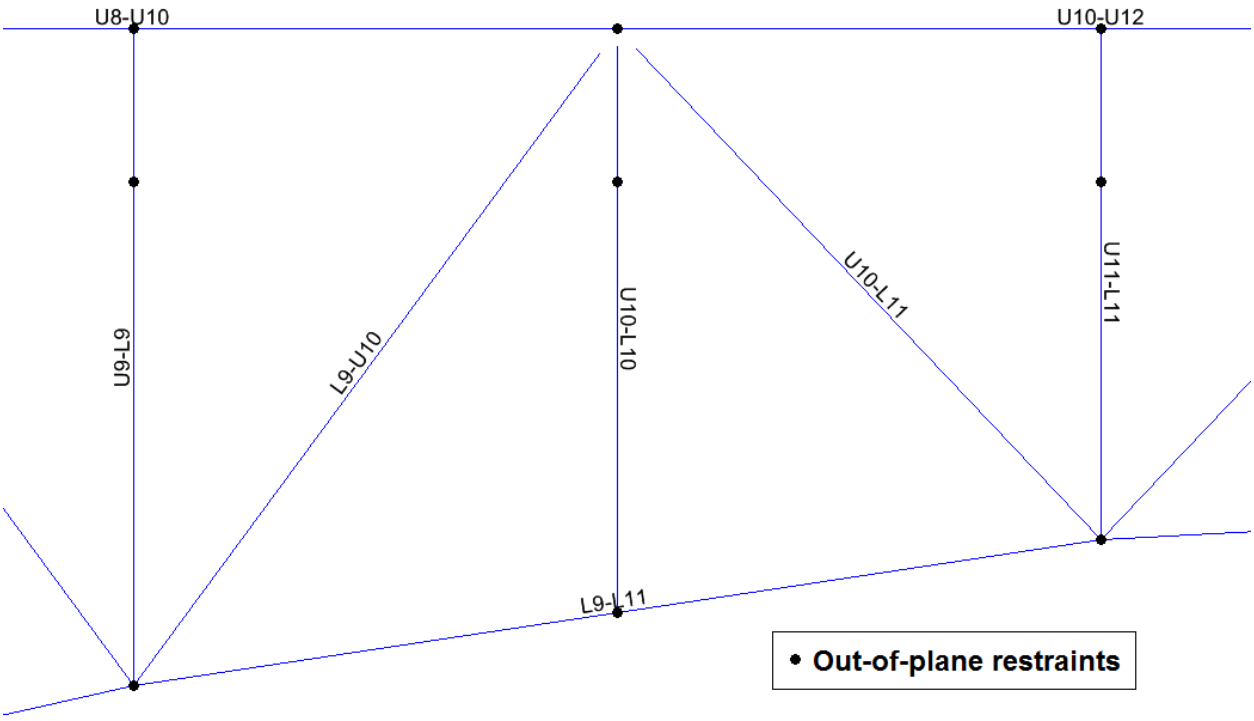

Figure 3.3-3: Typical out-of-plane restraints in the "Detailed U10 Connection" model

The material property information was obtained from the mechanical property test report by the FHWA (Beshah, Wright, & Graybeal, 2008). The gusset plates at the four U10 nodes were recovered from the wreckage and tested at the lab; the average properties were used in the structural analysis. The reported engineering strains (ε_{eng}) and stresses (σ_{eng}) were converted to true strains (ε_{true}) and stresses (σ_{true}) to program the shell elements (see Figure 3.3-4). The following expressions were used (Bruneau, Uang, & Sabelli, 2011):

$$\varepsilon_{true} = \ln(1 + \varepsilon_{eng})$$

$$\sigma_{true} = (1 + \varepsilon_{eng})\sigma_{eng}$$

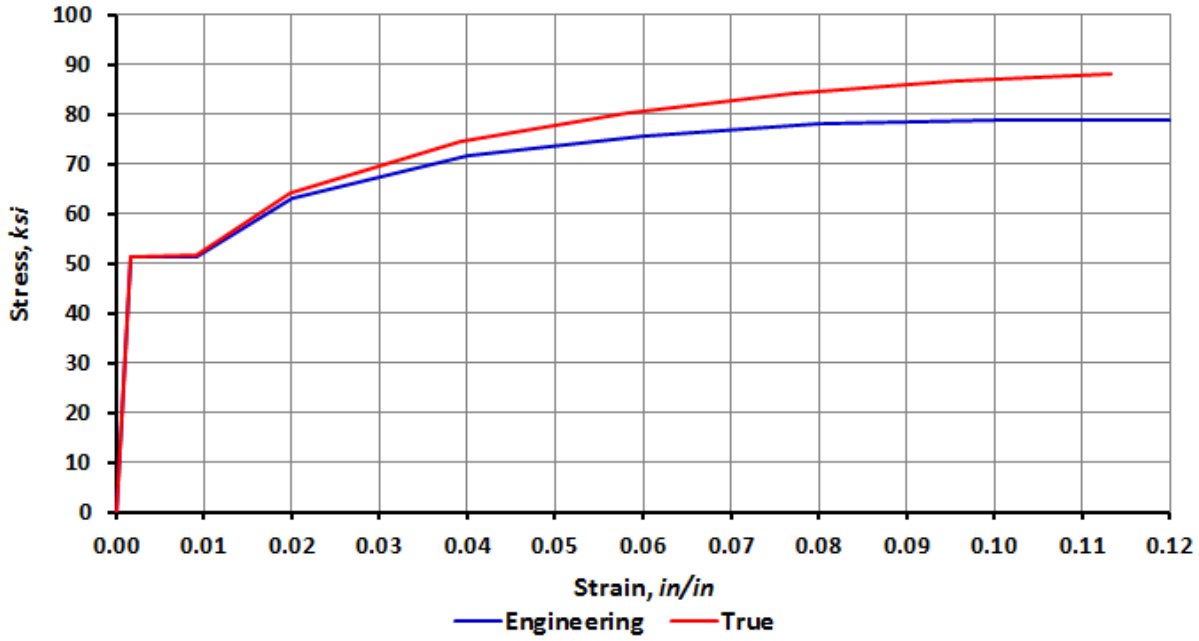

Figure 3.3-4: Stress – Strain relations for the U10 gusset plates material

3.4 Frame Hinge Models

After the gusset plates at the U10 nodes buckled, the axial stiffness of the L9-U10 diagonals was lost and the vertical deflection at this node increased rapidly. As node U10 deflects, flexure is introduced in the top and bottom chord members connected to U10 and L10. Bending began controlling the chord member behavior and they eventually developed axial-flexure plastic hinges. Frame Hinges were used to capture the nonlinear behavior of these members.

A cross section fiber analysis was performed to develop the axial-flexure interaction diagrams for the hinges (Bruneau, Uang, & Sabelli, 2011). The moment-curvature constitutive relationship was assumed as elastic-perfectly-plastic up to the plastic moment for a given axial load. The box members were discretized by dividing the cover plates into two fibers of half thickness, and the side plates with fibers up to 0.25 inches deep.

The mechanic property tests performed by the FHWA were performed at a strain rate of $0.02\ in/min$ or $22\ ksi/min$ approximately, which is close to the lower bound specified by the American Society for Testing and Materials (ASTM) specifications (Beshah, Wright, & Graybeal, 2008). This can be considered as a static loading condition. The plastic hinges developed in the main truss chord members during the collapse after the stiffness of the L9-U10 diagonals had been lost and therefore the strain rate was considerably higher. At high strain rates, the yield strength, tensile strength, and ductility of steel increase (Salmon, Johnson, & Malhas, 2009). The dynamic yield strength (F_{yD}, ksi) can be estimated based on the static yield strength (F_{yS}, ksi), the time of loading (t, sec) and the temperature $(T, °F)$ using the equation (Madison & Irwin, 1974):

$$F_{yD} = F_{yS} + \frac{174{,}000}{\log(2x10^{10}t)\,(T + 459)} - 27.4$$

The weather records from the University of Minnesota show that the temperature at the time of collapse was 92.1 °F (WJE, 2008). The time of loading (t) refers to the uniaxial tension test from the start of loading to the maximum load (Wright, 2012). The first three frames of the video footage were used to determine the time of loading since the frame rate of the video is 1 second. The deflection of the U10 node was scaled based on the length of the U10-L10 vertical member, resulting in an approximate $38\ in/sec$ node velocity of (see Figure 3.4-1). In a separate two-dimensional model, the stiffness of the L9-U10 diagonal was removed shortly after the end of load Stage 3 to simulate the buckling of the gusset plates. The structural analysis results give the stress change in the cross sections related to the deflection of node U10. These two results were used to calculate the strain rate and extrapolate to get the time of loading. This approach ignores

the stresses present in the members before the collapse started, which were between about 40 to 60 percent of yield. The results are summarized in Table 3.4-1.

Figure 3.4-1: First three frames captured by the security camera during the collapse

Table 3.4-1: Static and dynamic yield strengths for the frame hinges models

Member	**Plate**	**Temperature** T, °F	**Time of loading** t, sec	**Yield Strength**		
				F_{yS}, ksi	F_{yD}, ksi	**Increase**
L9-L11	Side	92.1	0.1543	38.42	44.29	15.3%
	Cover	92.1	0.1543	38.42	44.29	15.3%
U8-U10	Side	92.1	0.2828	53.91	58.88	9.2%
	Cover	92.1	0.2789	53.17	58.17	9.4%

The net section was used to define the interaction diagrams for the members. It was assumed that the inner row of rivet holes in the side plates coincides with the same cross section containing the access holes in the cover plates. The idealized cross-sections of the L9-L11 and U8-U10 members that were used for the fiber analysis are shown in Figure 3.4-1 and their respective axial-flexure interactions diagrams in Figures 3.4-2 and 3.

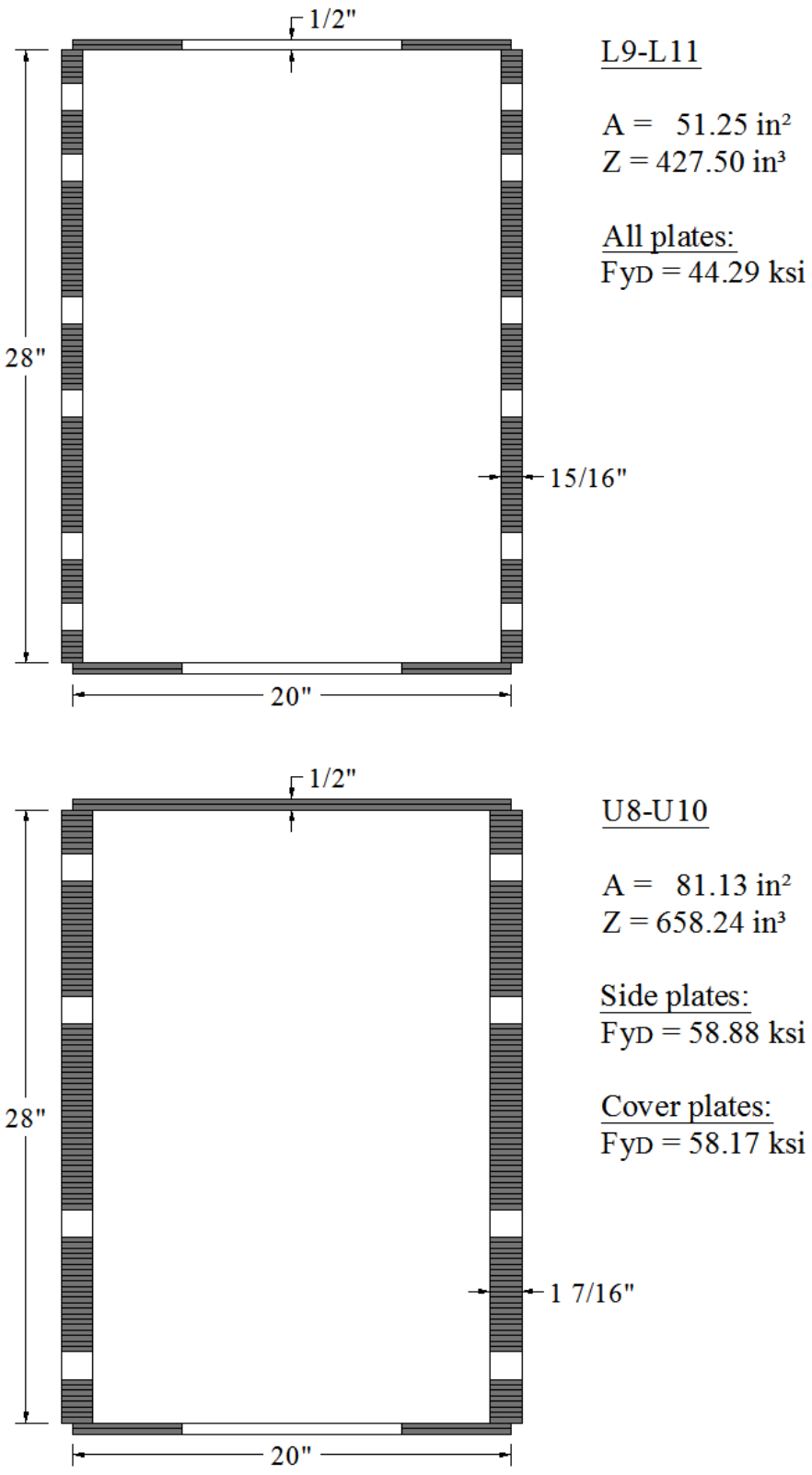

Figure 3.4-2: Discretized cross-sections for fiber analysis and their section properties

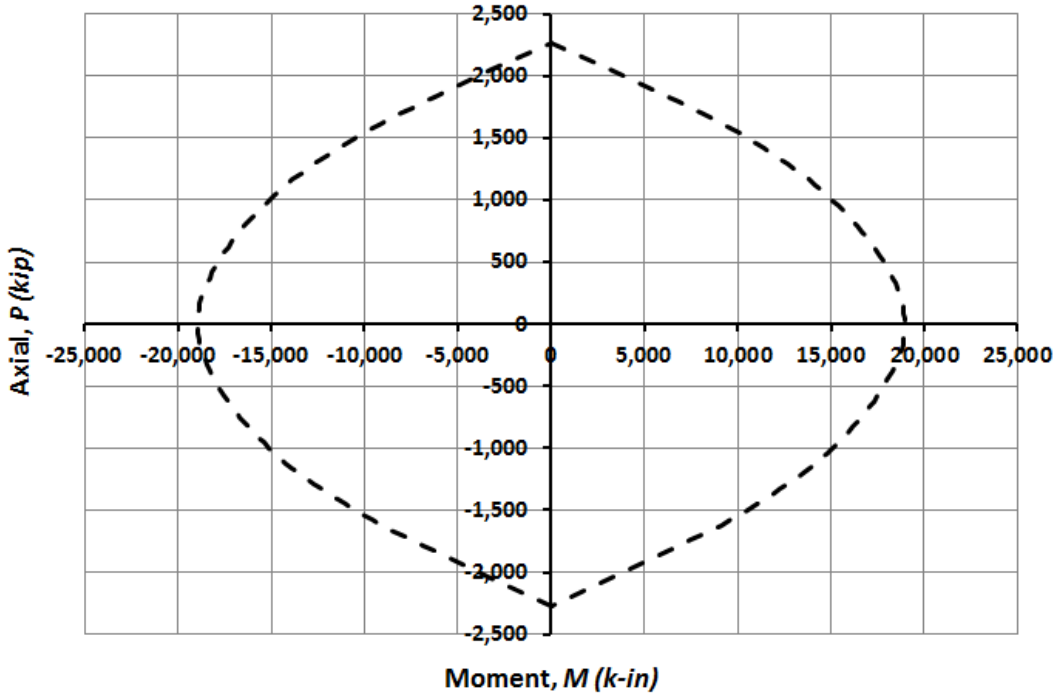

Figure 3.4-3: Axial-flexure interaction diagram for net section of L9-L11 members

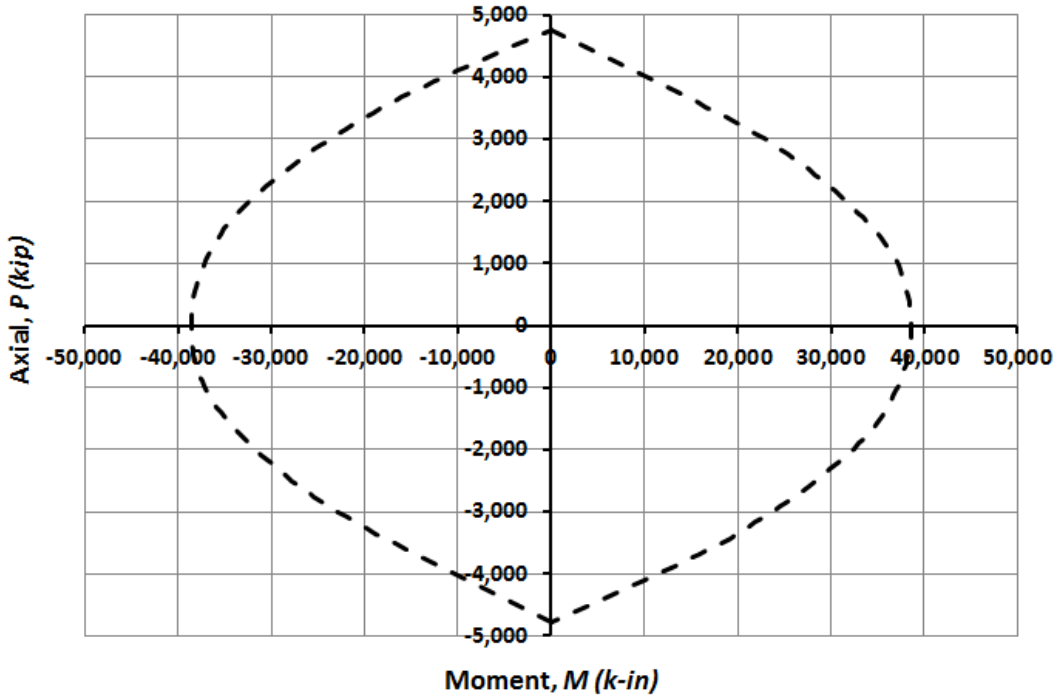

Figure 3.4-4: Axial-flexure interaction diagram for net section of U8-U10 members

3.5 Detailed Segment of the L9-L11 member

The Frame Hinges described in the previous section are defined using a cross-section fiber analysis that assumes that every fiber is at the yield stress in compression at one side of the neutral axis and in tension at the other side of the neutral axis. As shown in Figure 3.1-3, the stresses concentrate at the access hole edges. The same behavior is expected at the rivet hole edges. Therefore, the material will reach yield first at the hole edges. However, inelastic strains will be restrained by compatible deflection of the surrounding elastic material. To investigate the possibility of early local buckling in cross section, a refined finite element model (FEM) of the L9 end segment of the L9-L11 member was developed as shown in Figure 3.5-1. This member was selected because it is a compression-controlled member, the slenderness ratio of the side plates is larger than for the U8-U10 member, it has access holes in both cover plates, and a preliminary analysis using the frame hinges shows that the first plastic hinge develops in the critical section of this segment.

The plates in the FEM were modeled at their mid-surface location with a maximum mesh size of 1 by 1 inches. Since the edges of mid-surfaces do not coincide between the sides and cover plates, the nodes at these edges were connected by Weld Constraints, which couple the joints located within the specified tolerance (CSI, 2009). The segment of the L9-L11 member extends from the L9 end to the second stiffener plate located 210 in. from the end. This length includes five access holes with a tributary length of 42 in. each. The first stiffener was defined using a Diaphragm Constraint that only couples the in-plane deformations. The second stiffener, located at the free end of the model, was defined as a Body Constraint that couples both the in-plane deformation (diaphragm) and the out-of-plane deformation (rigid plate). This is analogous to the general assumption of plane sections and linear strain distribution.

The inner row of rivets holes on the side plates were modeled with 16 nodes around the perimeter and a finer mesh was defined to capture the stress concentrations. The supports consisted of linear springs that restrain in-plane deformations at the rivet locations where the holes were not modeled, and Gap elements that only carry compression forces perpendicular to the edge surface (see Figure 3.5-2). The stiffness of these springs and gap elements was taken as the initial slope of the load versus displacement plots reported for rivet tests performed by the FHWA under the National Cooperative Highway Research Program (NCHRP) Project 12-84 (Ocel J. M., 2013).

The axial forces, shear forces, and bending moments were input at the free end of the segment to represent the pre and post buckling behavior of the gusset plates that was determined by the preliminary analysis. The nonlinear material behavior was included only in the shell elements contained within the 42 inches tributary length of the access hole where the rivet holes were modeled, as shown in Figure 3.5-1.

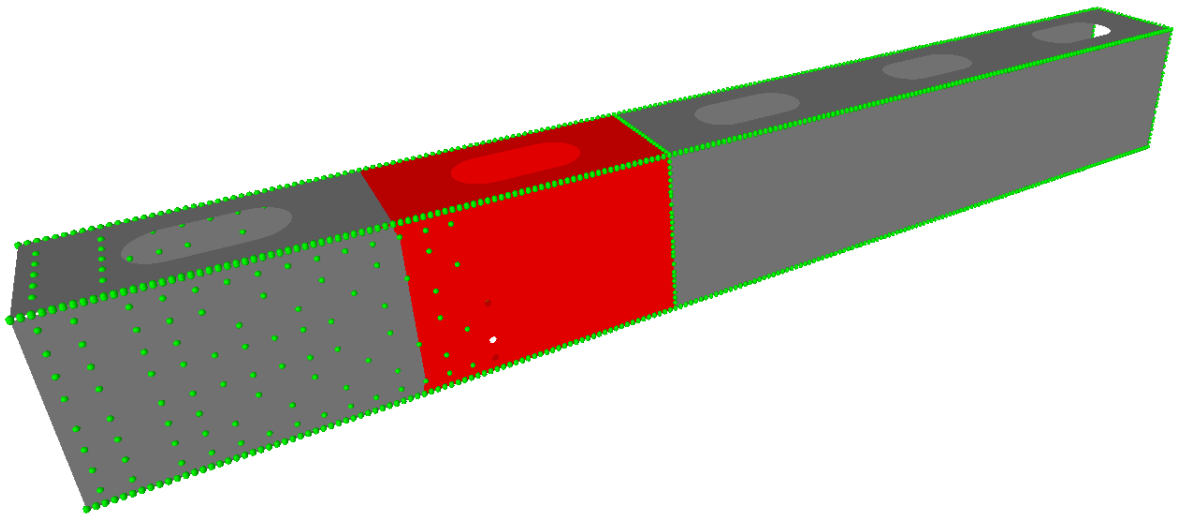

Figure 3.5-1: Detailed segment of the L9-L11 bottom chord member
Linear shells (gray), nonlinear shells (red) and restarined or constrained joints (green)

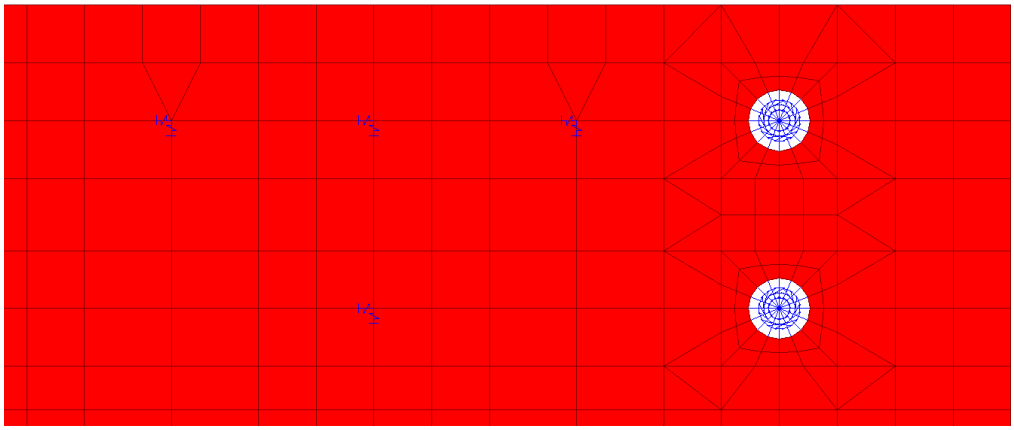

Figure 3.5-2: Close-up at a top portion of the side plates containing rivet holes Springs and gap elements shown in blue

3.6 Nonlinear 2D Model

Nonlinear behavior was incorporated into the base two-dimensional model using Nonlinear Links and Frame Hinges properties. Nonlinear Links are used at the U10 end of the L9-U10 members to model buckling behavior of the U10 gusset plates. The force-displacement relation of the links was defined based on the results of the gusset plates buckling analysis presented later in Section 4.1. Frame Hinges are used at the mid and end points of the chord members immediately above and below the L9-U10 diagonal, the upper chord U8-U10 member and the lower chord L9-L11 member, to model potential plastic hinges at these locations. The axial-flexure interaction diagrams for the hinges were defined by the cross section fiber analysis and calibrated to match the FEA results of the detailed L9-L11 segment. The moment-curvature constitutive relationship was assumed to be elastic-perfectly- plastic up to the plastic moment for the given axial load. The hinges were assigned at the 0.0, 0.5 and 1.0 relative locations for simplicity where in reality these developed in the members just outside of the connection, except for node U10 that fractured between the top chord members; this results in a slight underestimation of the capacity. The final nonlinear 2D model is shown in Figures 3.6-1 and 2.

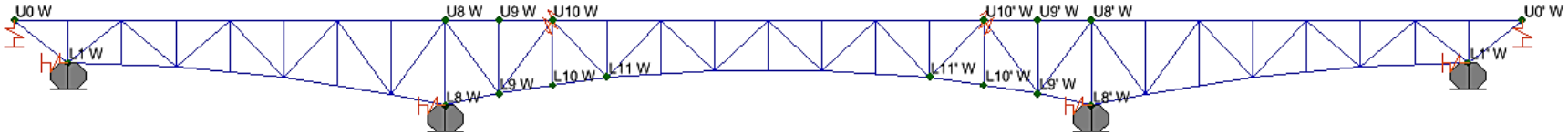

Figure 3.6-1: Elevation view of the nonlinear 2D model, looking west
Frame Hinges (green), Springs and Nonlinear Links (orange)

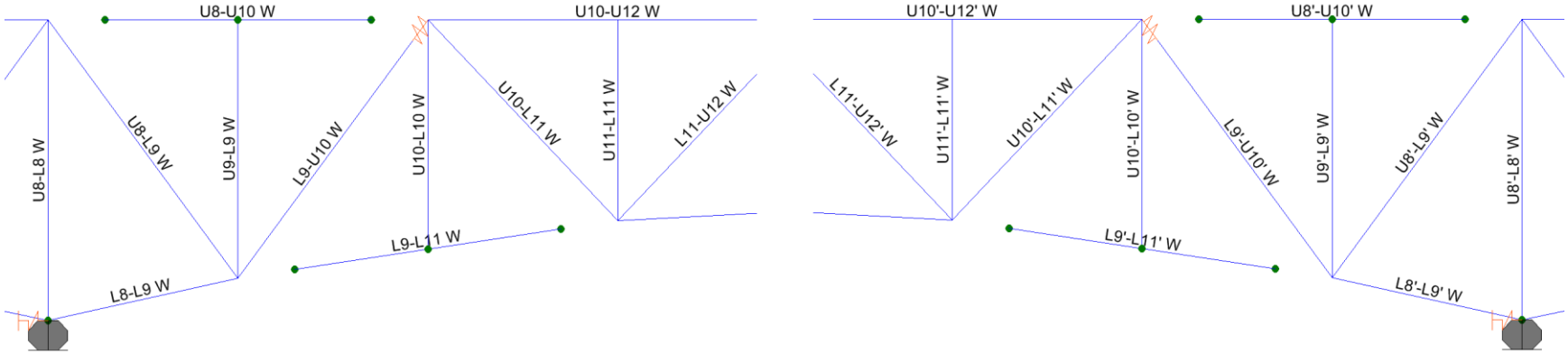

Figure 3.6-2: Center span ends of the nonlinear 2D model,elevation looking west
Frame Hinges (green), Springs and Nonlinear Links (orange)

CHAPTER 4. RESULTS AND DISCUSSION

4.1 U10 Gusset Plate Buckling Analysis

After exhaustive investigation, the NTSB concluded that the collapse of the I-35W Highway Bridge was result of inadequate load capacity of the gusset plates at the nodes U10. The inadequate capacity was due to design error of the bridge design firm resulting in gusset plates with thickness of 0.5 in., which is half of the 1 in. required thickness. In this scenario, the portion of the gusset plates that are connecting the L9-U10 diagonal buckles out-of-plane creating instability in the structure. For this reason, it is very important to start the collapse analysis by studying the buckling behavior of the U10 gusset plates.

The U10 gusset plates connected the five main truss members meeting at nodes U10 and U10' in both trusses, as shown in Figure 2.1-4. There was one large riveted gusset plate at both sides of the main truss members and top and bottom splice plates connecting the cover plates of the upper chord members. This resulted in 630 rivets in the overall connection.

The axial forces transferred from the main truss members to the U10 gusset plate at the end of the different load stages are shown in Table 3.2-2. Special attention is given to the axial forces at the U10 end of the L9-U10 diagonal member where it is believed that the collapse started. Since the total load on the bridge at the time of collapse was somewhere between the loads at the end of Stages 3 and 4, the axial forces were determined for both the Stage 3 plus traffic load case and the Stage 3 plus construction load case, and shown in Table 4.1-1. This is used for later comparison with the buckling load capacity of the gusset plates.

Table 4.1-1: Axial forces at U10 end of L9-U10 diagonal member

Stage 3	Stage 3 + Traffic	Stage 3 + Construction	Stage 4
-2,085	-2,258	-2,228	-2,401

The results shown in Table 4.1-1 give a better estimate of the axial force on the west truss diagonal member L9-U10 at the time of collapse. If the traffic load at the time of collapse is assumed as approximately equal to the normal service of the bridge, the buckling strength of the U10 gusset plates must be between $2{,}258\ kip$ and $2{,}401\ kip$. This represents a range of $143\ kip$ which is only 6 percent of the axial force at the end of load Stage 4.

Photographic evidence shows that the gusset plates at the four U10 connections had out of plane distortions at the free edges where the L9-U10 compression diagonals were connected. The straight white line Figure 4.1-1 shows where the edge of the gusset plate would be without distortion. One photograph was taken by the University of Minnesota staff in 1999 as part of a project, and few others were taken by the URS engineering firm in 2003 as part of a fatigue evaluation, but none of these were reported to the transportation officials before the collapse. The photographs were examined by the NTSB to determine the magnitude of the out of plane distortions. They concluded that the distortions were 0.60 inches plus/minus 0.15 inches, resulting in a range from 0.45 inches to 0.75 inches (Ocel & Wright, 2008).

There are two different buckling analysis methods available in SAP2000, Linear and Nonlinear Buckling (CSI, 2009). The Linear Buckling is an Eigenvalue analysis that predicts the theoretical buckling strength or critical load of the structure idealized as elastic. Perturbations are automatically applied to the structure to form the "mode shapes" and their corresponding buckling factors are calculated based on the applied loads. These factors represent the ratio of the

loading that will induce buckling for the corresponding mode shape. Since the Eigenvalue analysis is a linear approach, the theoretical buckling strength generally overestimates the buckling load. The Nonlinear Buckling analysis is a static method that incorporates material and geometric nonlinearities, and requires a small destabilizing load or initial imperfection to start the solution for the desired buckling mode. Since the nonlinear approach considers material and geometric nonlinearities, it is generally more realistic than the linear approach.

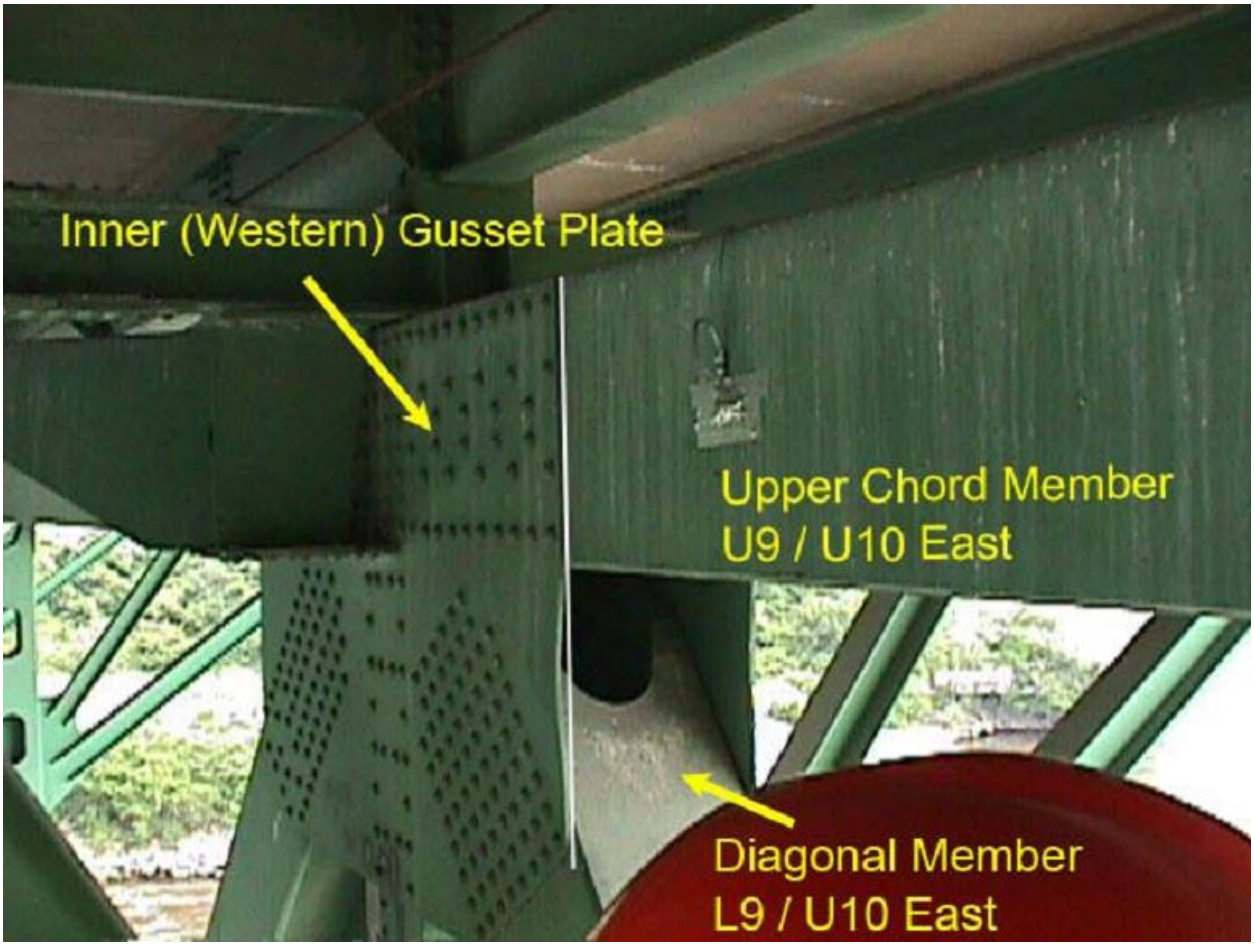

Figure 4.1-1: Bowed U10 East Gusset Plates, looking northeast from inside the structure Retrieved from the NTSB HWY07MH024 – Photograph Study Report (Brazy, 2008)

The buckling analysis of the structure was performed on the 2D model with the detailed U10 connection described in Section 3.3. The Linear Buckling analysis was performed in the structural model to compare the critical buckling mode shape to the actual out of plane distortions of the gusset planes as captured in the photographs. The resulting critical load is probably overestimated by this analysis. Figure 4.1-2 shows the buckled shape for mode 1, which is the critical mode. The out-of-plane displacements at the free vertical edge on the side where the L9-U10 compression diagonal was connected are similar to the ones shown in the photographs. This indicates that that the bowing observed in the gusset plates could have been caused by a developing buckling mode.

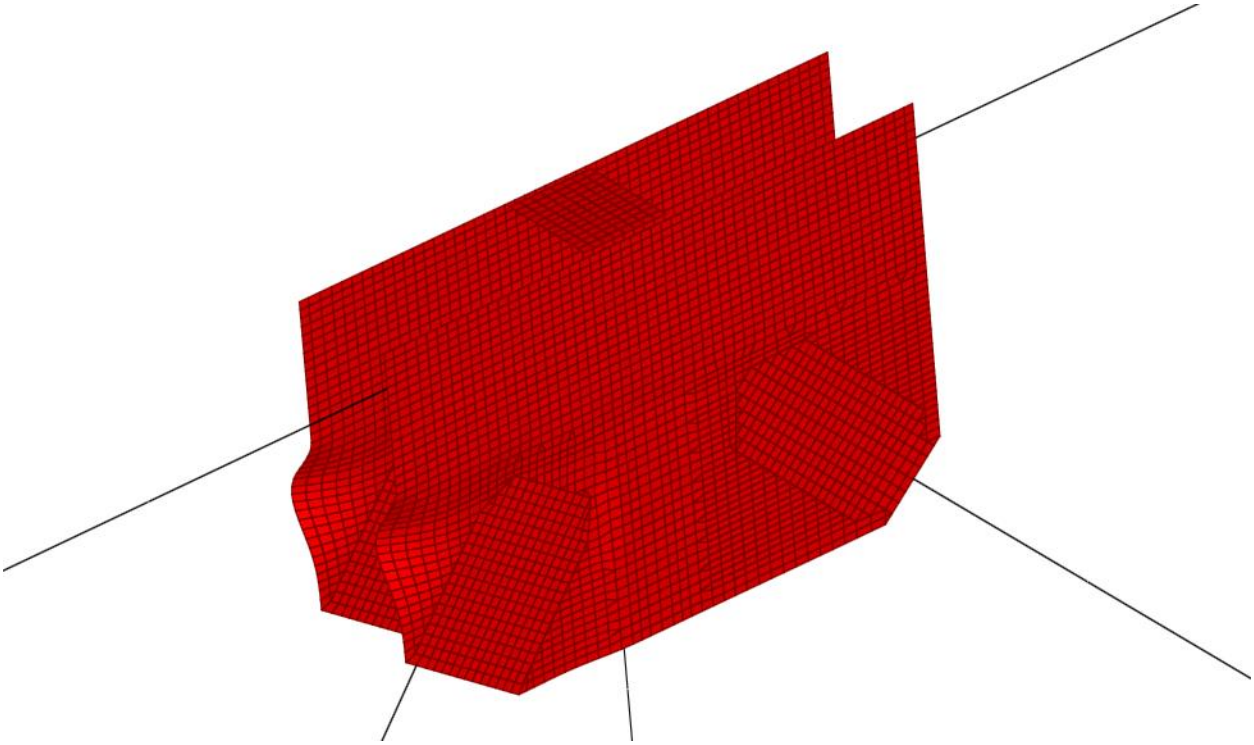

Figure 4.1-2: Critical linear buckling mode shape of the U10 gusset plates (Stiffness at end of Stage 4)

The Eigenvalue analysis can be performed using either the stiffness at the initial unstressed condition or the stiffness at the end of a nonlinear load case that includes the softening effects

that occur due to material nonlinearities. The buckling analyses results using the initial unstressed stiffness and the stiffness at the end of load Stage 4 are shown in Table 4.1-2. The critical axial force in this table represents the theoretical axial forces in the L9-U10 diagonal that would cause buckling of the U10 gusset plates without initial imperfections.

Compared to the expected axial force between $2{,}258\ kip$ and $2{,}401\ kip$ on the west truss L9-U10 diagonal member at the time of collapse, the buckling analysis using the initial stiffness grossly overestimates the critical load by a factor of 3.226. The result using the reduced stiffness at the end of Stage 4 gives a better estimate with a buckling factor of 1.255. The analysis using the reduced stiffness provides a reasonable prediction. The compressive axial force of $2{,}401\ kip$ has no effect on the analysis using the initial stiffness but it creates the softening in the gusset plates' material considered in the analysis using the reduced stiffness at the end of Stage 4.

Table 4.1-2: Linear buckling axial force at U10 end of L9-U10 diagonal

Stiffness	Axial force (kip)	Buckling factor	Critical Axial force (kip)
Initial	-2,401	3.226	-7,745
End of Stage 4	-2,401	1.225	-2,941

The Nonlinear Buckling analysis was also performed in the structural model to study the buckling behavior of the gusset plates and get a more realistic estimate of the buckling capacity. In this analysis, both initial imperfections and a small destabilizing force were used to start a buckling mode similar to that shown in the photographs and later confirmed by the Linear Buckling analysis. The initial imperfections were modeled to represent out-of-straightness of the gusset plates from the shop and the destabilizing load represents the built-in stresses and additional deformations that occur during the erection process.

The contribution of initial imperfections and built-in deformations, plus the additional deformations from the loads on the bridge at the time of collapse, must be in the range between 0.45 inches and 0.75 inches under the normal service load of the bridge. The best estimate of the compression axial force at the U10 end of the L9-U10 diagonal is $2{,}258\ kip$ for Stage 3 plus traffic load. This is assumed as the normal service load of the bridge present when the photographs were taken.

There is no way to proportion the initial imperfections and built-in deformations precisely so that the final deformation, after the Stage 3 and traffic loads were added, matches the best estimate of 0.60 in. Therefore, a notional load was applied at the upper end of the L9-U10 diagonal where it meets the outer-most row of rivets, denoted as the reference point, and a displacement-controlled analysis was performed to get 0.20 in. of out-of-plane deformation at that point, as shown in Figure 4.1-3. This is one-third of the target 0.60 in. deformation. In a second step, the joint displacements were added to the original joint coordinates to create initial imperfections in the unstressed condition.

The built-in imperfections were modeled using a small destabilizing load at the reference point. A trial and error displacement-controlled analysis was performed initially at 0.05 in. displacement increments until the target displacement between 0.45 in. and 0.75 in. was achieved for an axial force of $2{,}258\ kip$ in the compression diagonal. The best match was obtained with a built-in deformation of 0.075 inches resulting in a total displacement of 0.475 inches at the reference point. This required a $0.484\ kip$ destabilizing load (see Figure 4.1-4). The resulting built-in Von Mises stresses in the gusset plates are about $20\ ksi$ in average with peaks of about $40\ ksi$ around the corners at the end of the L9-U10 diagonal, as shown in Figure 4.1-5.

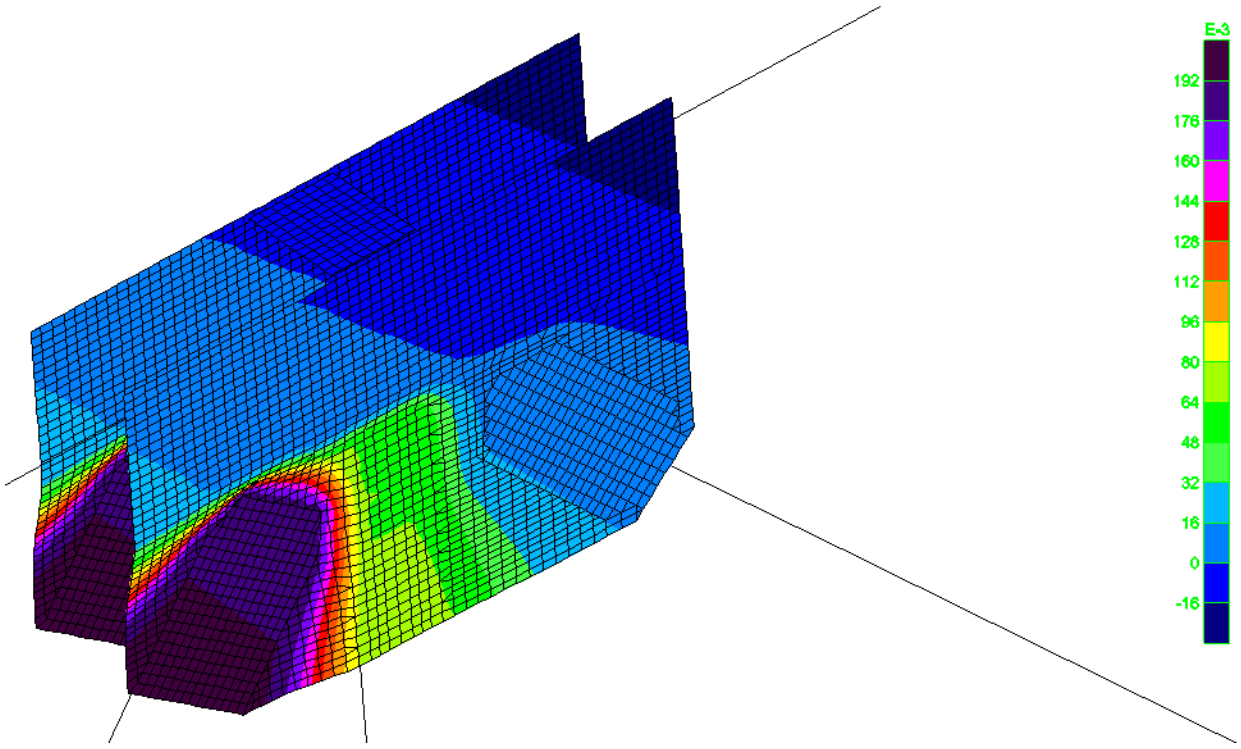

Figure 4.1-3: Initial out-of-plane imperfections (inches) at U10 gusset plates

The total out of plane displacement of the gusset plate was 0.475 in. under service load at the reference point. The maximum displacement reached approximately 0.52 in., including the 0.20 in. from the initial imperfections, occurring approximately at the middle of the vertical free edge (see Figure 4.1-6). It is seen that the displaced shape at this load state is similar to that captured in the photographs.

The Von Mises stresses at this level go as high as 95 ksi locally as shown in Figure 4.1-7. It is worth noting that in SAP2000, yielding occurs independently in each principal direction of layered shell elements, it does not use a biaxial yield criterion like Von Mises or Tresca, which may give unconservative results depending on the different stress combinations. For this reason, calculated Von Mises stresses may be larger than the maximum stress defined in the material constitutive model.

The buckling load is defined as the maximum load applied to the model and it is indicated by softening in the load versus displacement plot. For the given initial imperfection of 0.20 inches and the additional built-in deformation of 0.075 inches at the upper end of the L9-U10 diagonal, the axial force in the compression diagonal is $2{,}319\ kip$ with a total out-of-plane displacement of 0.585 inches at the buckling load.

The deflected shape of the gusset plates at the buckling load is shown in Figure 4.1-8. The displacement of the upper end of the compression diagonal is increasing almost without restriction at this stress level, indicating a complete loss of stiffness of the gusset plate. The maximum displacement of about 0.66 in. occurred at about the middle of the vertical free edge connecting the compression diagonal. The Von Mises stresses in the gusset plates at the buckling load are shown in Figure 4.1-9.

The total load versus displacement and axial force versus displacement plots for the different built-in deformations are shown in Figures 4.1-10 and 11 respectively. The total load refers to the applied load in the model, which totaled $12{,}863\ kip$ at the end of load Stage 4. The axial force is taken at the upper end of the L9-U10 compression diagonal, which reaches a maximum of $2{,}401\ kip$ at the end of Stage 4. The displacement is the total out of plane deformations of the gusset plate at reference point including the initial imperfection, the built-in deformation and the additional deformation due to loading on the bridge. Five curves are plotted in each figure, four with increasing initial imperfections (0.2, 0.25, 0.3, and 0.35 in.) and one curve with the best estimate of the buckling capacity that starts at 0.275 in. The total load and axial forces at the end of Stages 3 and 4 and the displacement range of the photographs are shown in the figures for comparison.

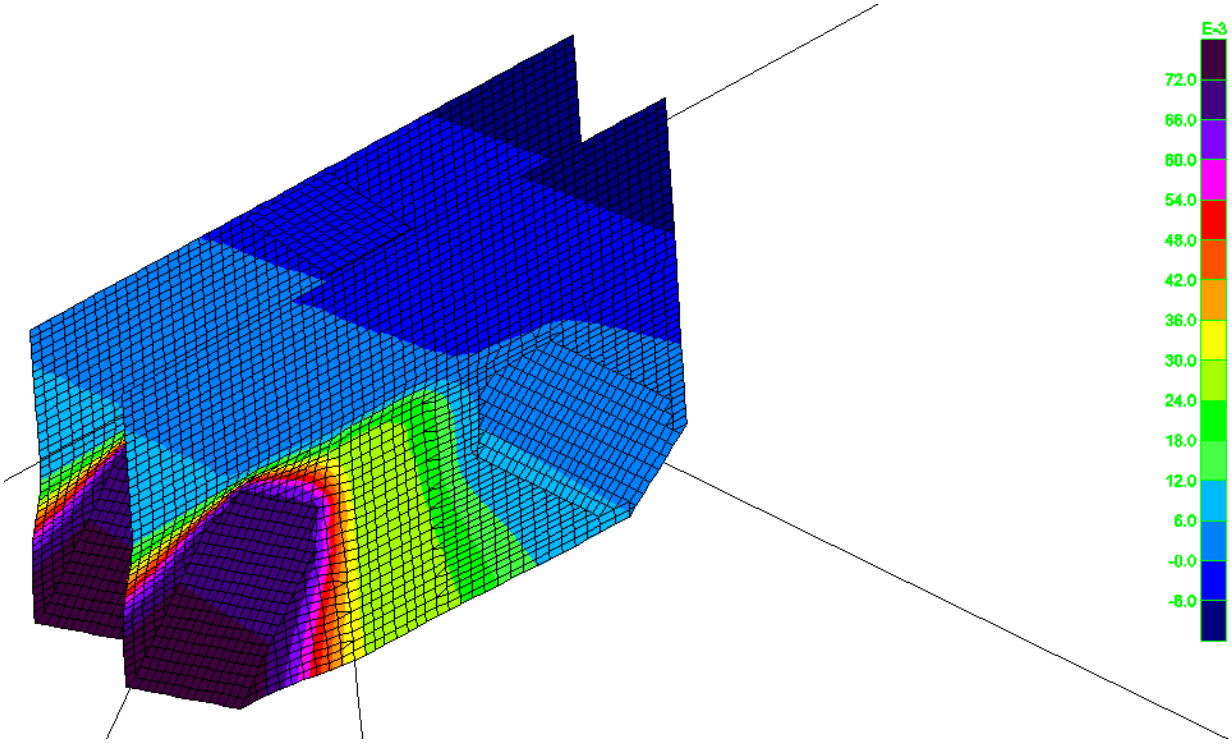

Figure 4.1-4: Built-in out-of-plane imperfections (inches) at U10 gusset plates

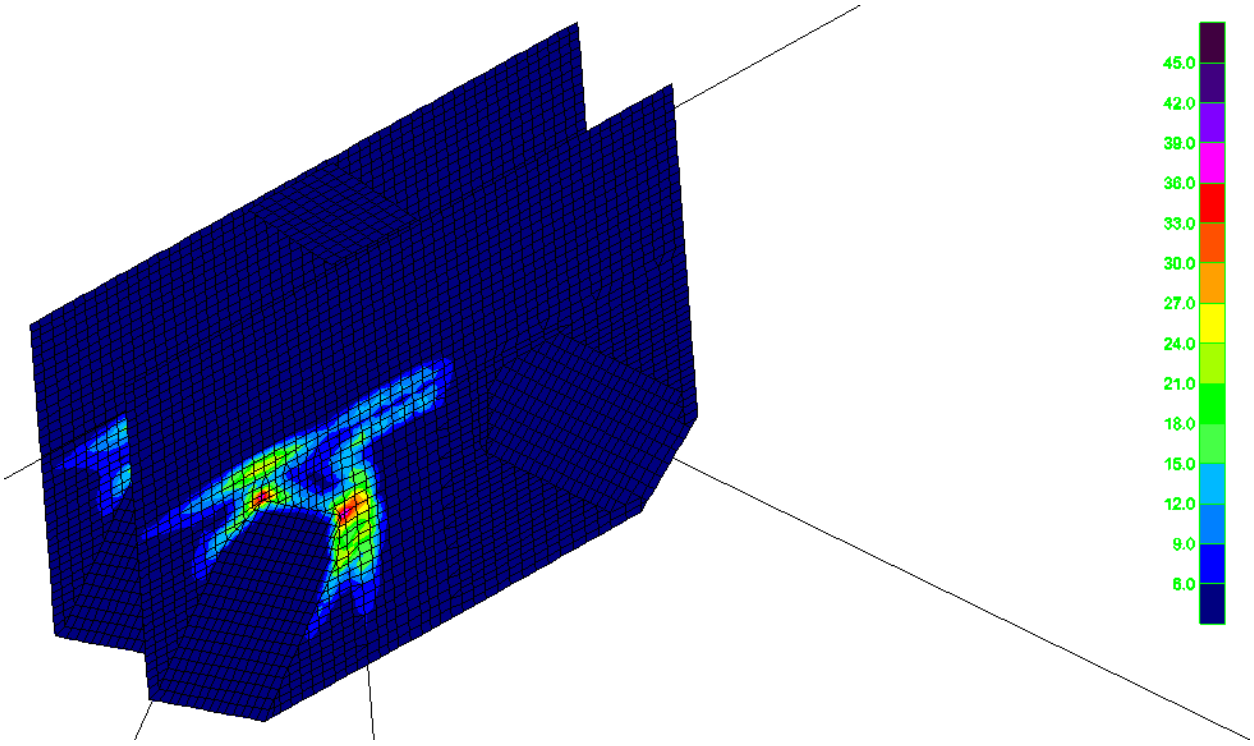

Figure 4.1-5: Built-in Von Mises stresses (ksi) at U10 gusset plates

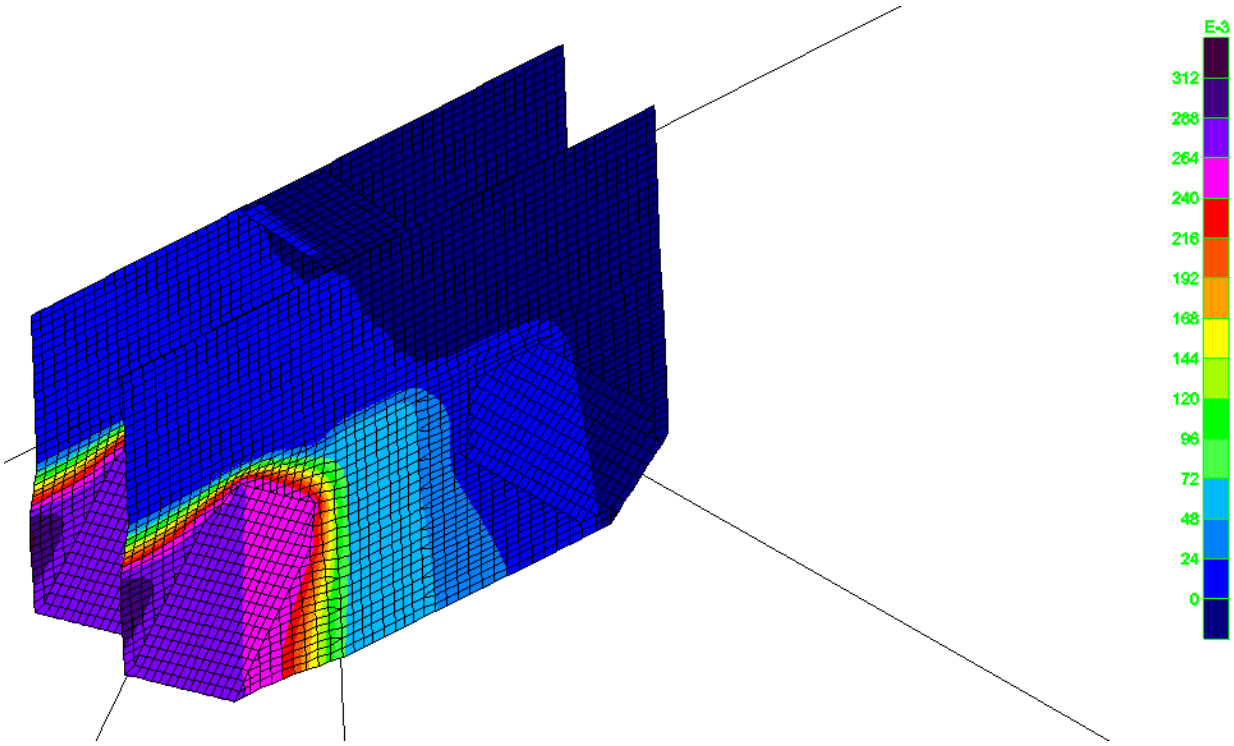

Figure 4.1-6: Service load out-of-plane displacements (inches) at U10 gusset plates

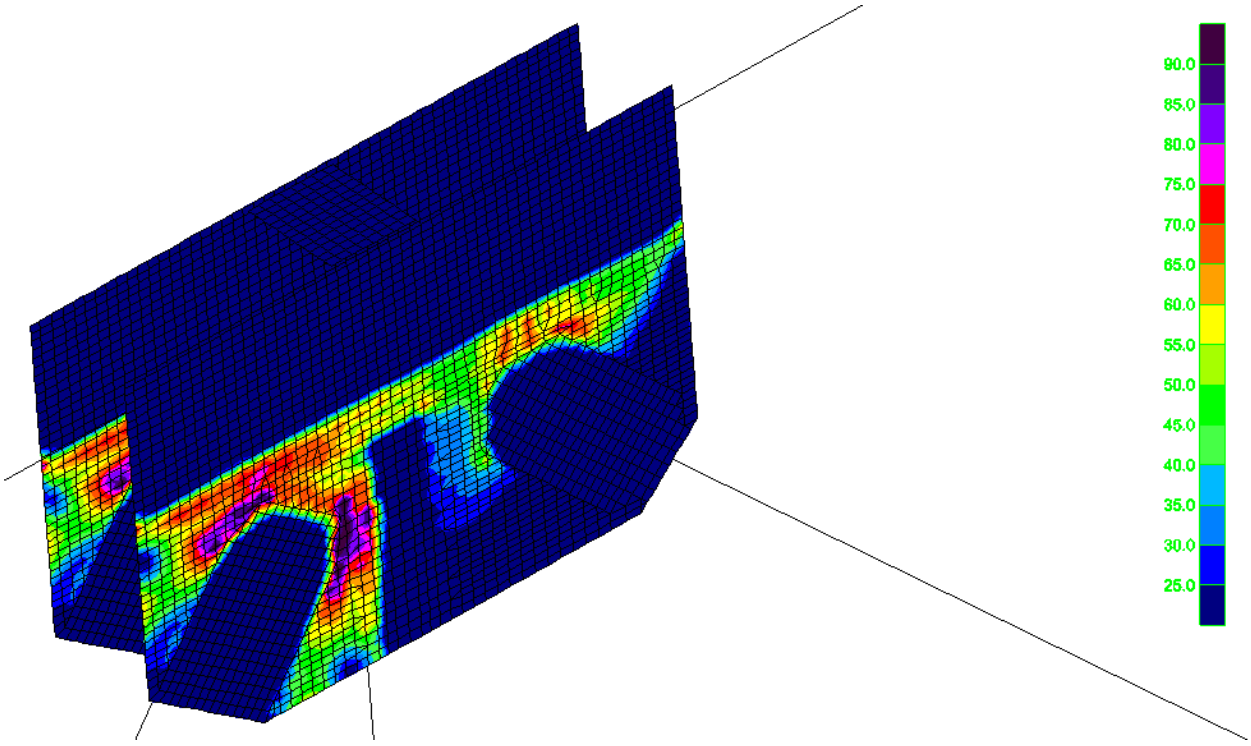

Figure 4.1-7: Service load Von Mises stresses (ksi) at U10 gusset plates

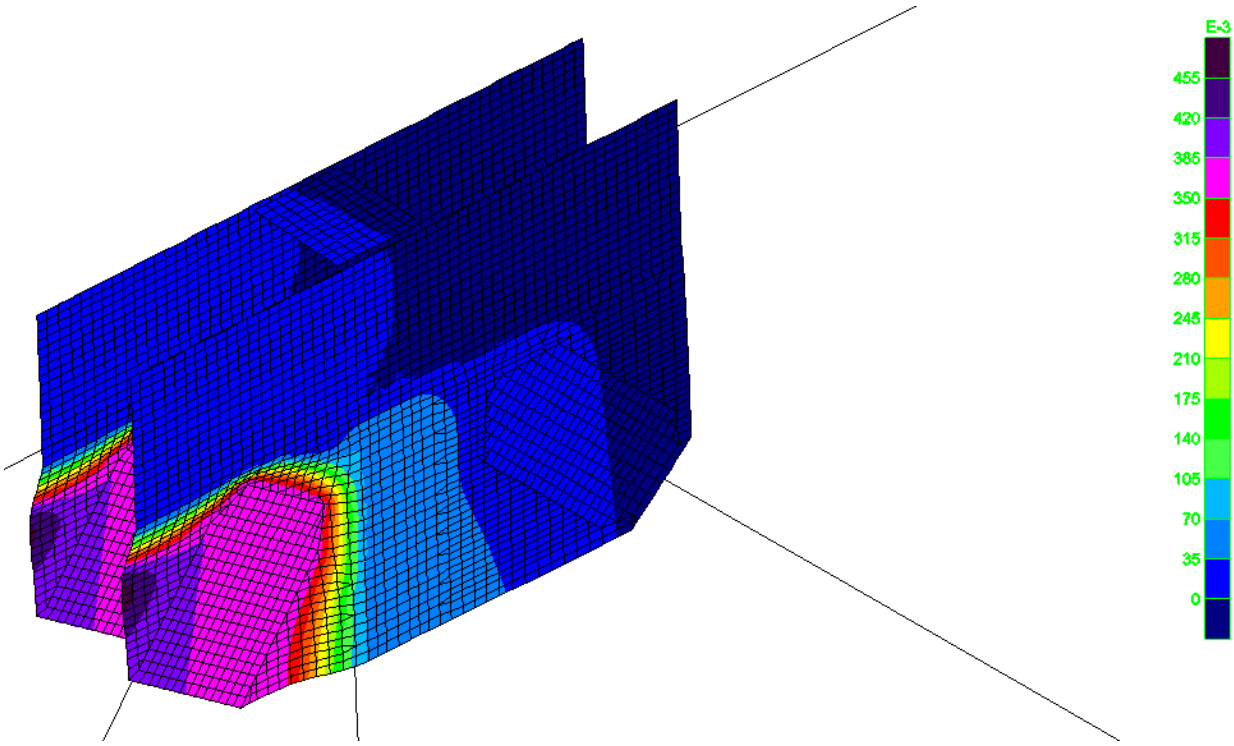

Figure 4.1-8: Maximum load out-of-plane displacements (inches) at U10 gusset plates

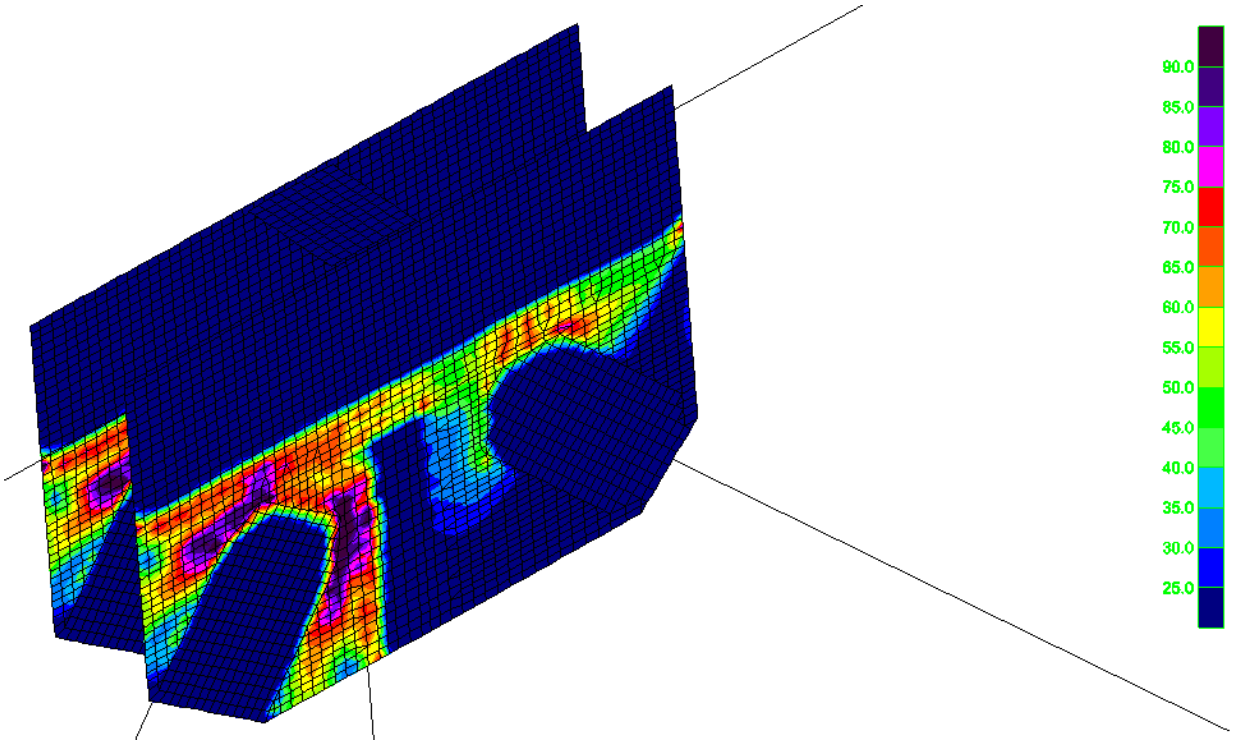

Figure 4.1-9: Maximum load Von Mises stresses (ksi) at U10 gusset plates

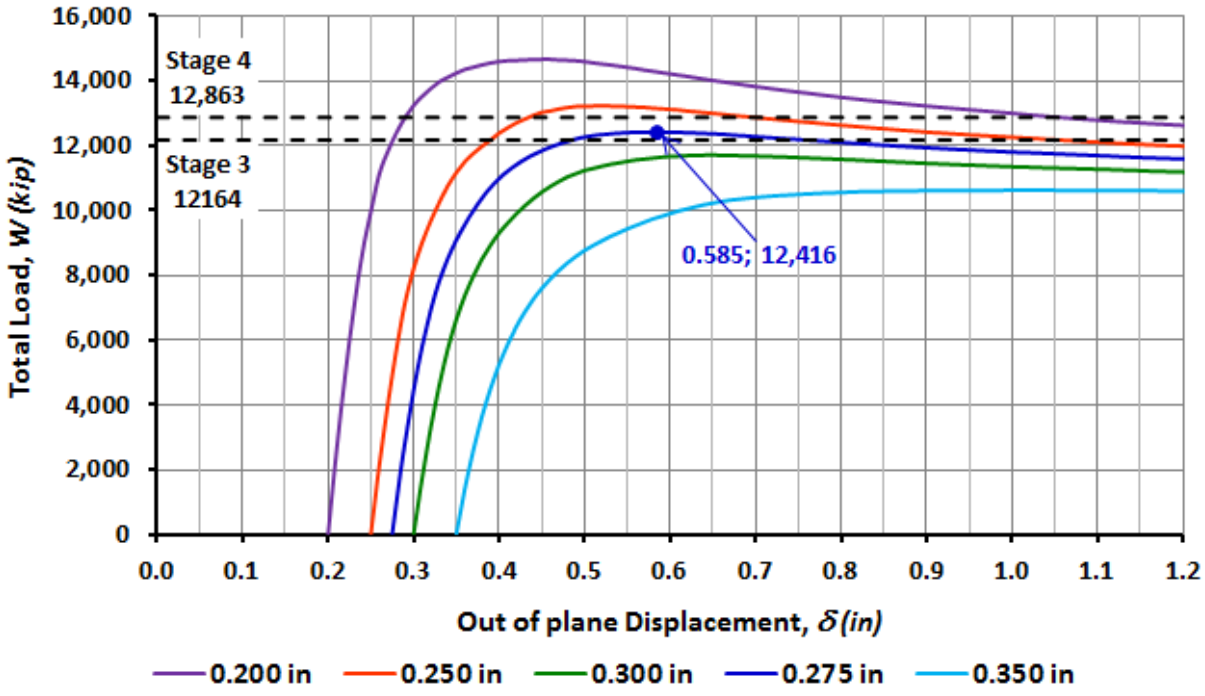

Figure 4.1-10: Total load vs out-of-plane displacement at U10 end of L9-U10 diagonal

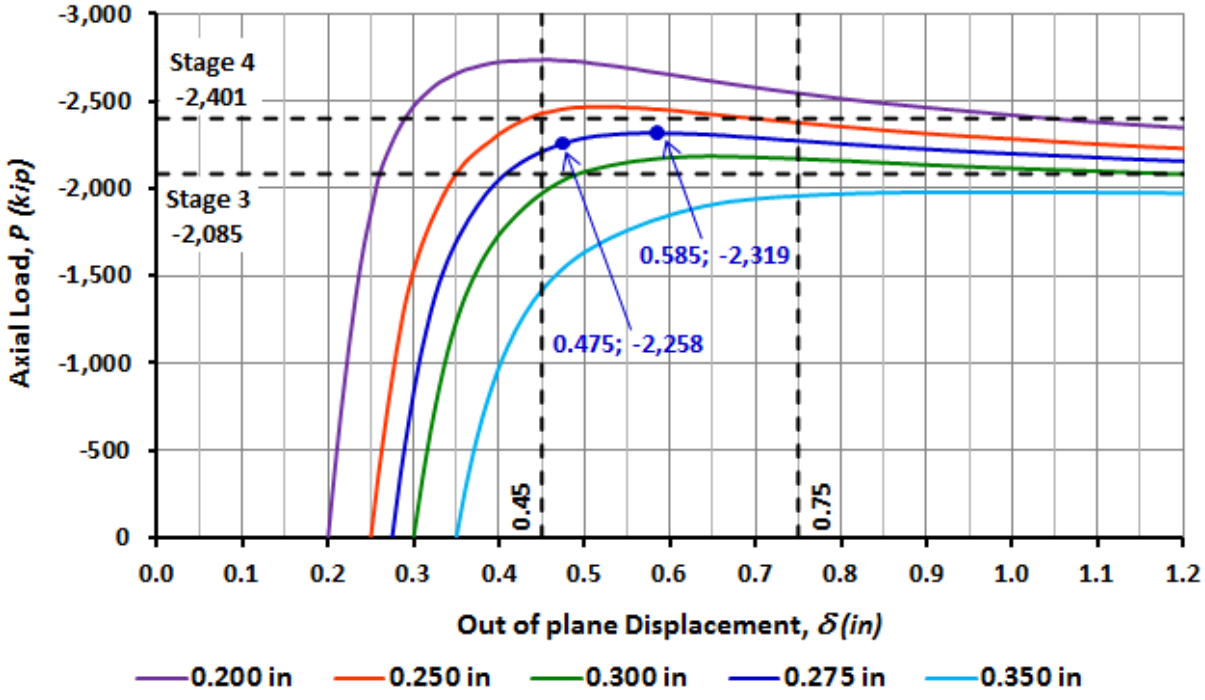

Figure 4.1-11: Axial force vs out-of-plane displacement at U10 end of L9-U10 diagonal

Figure 4.1-10 shows that the only load versus displacement curve where the maximum value falls between load Stages 3 and 4 is the curve based on the starting at 0.275 in. (presented in blue) stating displacement. The curves with smaller initial displacement have buckling capacity greater than the total load at the end of Stage 4 and the curves with larger initial displacement have smaller capacity than the load at the end of Stage 3. The maximum load for each curve, which corresponds to the buckling capacity, and their corresponding total displacement are presented in Table 4.1-3.

Figure 4.1-11 shows that the total out of plane displacement at the reference point of the curve starting at 0.275 inches (presented in blue) is between the 0.45 in. to 0.75 in., range determined by the NTSB. The maximum axial force of this curve falls between the axial forces at the load Stages 3 and 4, which also meets the criteria. The total out-of-plane displacements for $2{,}258\ kip$ axial compressive force, and the axial forces at buckling and their corresponding displacements are presented in Table 4.1-4.

Table 4.1-3: Total load and out-of-plane displacements at U10 end of L9-U10 diagonal

Total initial imperfection (in)	**Maximum load**	
	Displacement (in)	**Total load (kip)**
0.200	0.460	14,657
0.250	0.520	13,217
0.275	0.585	12,416
0.300	0.650	11,703
0.350	1.020	10,617

Table 4.1-4: Axial forces and out-of-plane displacements at U10 end of L9-U10 diagonal

Total initial imperfection (in)	Stage 3 + Traffic		Maximum load	
	Displacement (in)	Axial force (kip)	Displacement (in)	Axial force (kip)
0.200	0.275	-2,258	0.460	-2,738
0.250	0.386	-2,258	0.510	-2,468
0.275	0.475	-2,258	0.585	-2,319
0.300	-	-	0.650	-2,185
0.350	-	-	0.660	-1,980

Another Nonlinear Buckling analysis was performed with the same initial imperfections but with a different plate thickness to study its effect on the buckling capacity of the gusset plates. Figure 4.1-11 shows the axial force versus out-of-plane displacement for thicknesses of 0.5 in. and 0.625 in. It is seen that the maximum compression force increases from 2,319 kip for the 0.5 in. plate to 3,352 kip for the 0.625 in. plate; both occurred at about the same total out-of-plane displacement. A 25 percent increase in the plate thickness resulted in a 45 percent increase in capacity, which suggests that the plate thickness is very significant in the buckling capacity.

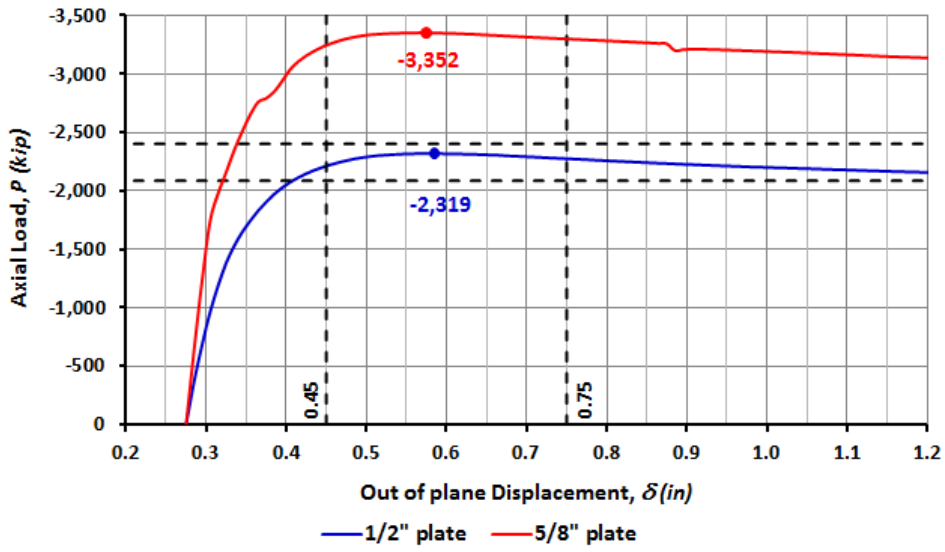

Figure 4.1-12: Axial force vs out-of-plane displacement at U10 for different plate thicknesses

The Nonlinear Buckling analyses were initially limited to a maximum 1 in. additional out-of-plane displacement to accelerate the trial and error process of selecting the appropriate buckling curve. Later, the analysis for the 0.275 in. curve was extended to larger displacements to determine the post buckling force versus deflection response. The final slope on the tension side of the material constitutive model was set to 10 percent of the initial slope to help with convergence and provide a very simplistic method to predict fracture behavior. Similarly, the final slope in the compression side was set to zero to maintain the maximum stress constant. The analysis stopped due to convergence problems when the maximum tensile strain in the gusset plate met the negative slope, thereby indicating possible fracture.

Figure 4.1-13 shows the deformed shape of the gusset plates at the end of the analysis. The total vertical deflection of node U10 at this state was 5.22 in., 0.82 in. beyond the deflection where buckling occurred (4.40 in.). The maximum total out of plane displacement of 4.07 inches occurred at about the middle of the free edge connecting the compression diagonal.

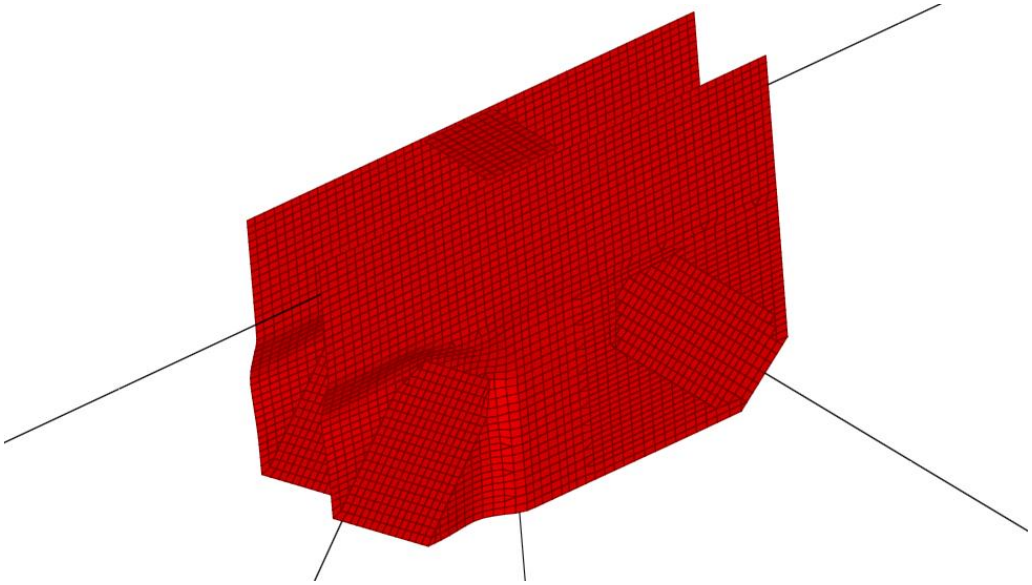

Figure 4.1-13: Deformed shape of the U10 gusset plates at end of analysis (Scale factor of 1.0)

The plots of total load versus out-of-plane displacement of the reference point and the deflection of node U10 are shown in Figure 4.1-14. The load versus out-of-plane displacement relation (presented in blue), an extension of the selected buckling curve in Figure 4.1-10, shows a post-peak load decrease to $11{,}537\ kip$ at about 1.5 inches displacement, followed by a slight increase back up to$12{,}078\ kip$ load with a corresponding 2.80 in. displacement increase. The load versus vertical deflection curve (presented in red) shows a snap-back immediately after the buckling load of $12{,}078\ kip$ at 4.40 in. vertical deflection. The deflection stabilizes and increases back to $12{,}078\ kip$ at 5.22 in. of vertical deflection. This snap-back behavior indicates the possible onset of dynamic deflection of the bridge that may not be predicted well by static analysis. The plots of axial force in the L9-U10 diagonal versus the same deformations are shown in Figure 4.1-15. As expected, they are somewhat proportional the plots shown in Figure 4.1-14. The axial compression forces are $2{,}319\ kip$ at buckling, $2{,}137\ kip$ in the valley, and $2{,}205\ kip$ at the end of the analysis where the curve flattens-out. These plots are in accordance with the result of the NCHRP Project 12-84 (Ocel J. M., 2013).

The deflection of node U10 versus the out-of-plane displacement of the reference point is shown in Figure 4.1-16. The curve starts at 0.275 in. displacement from the 0.2 in. initial imperfection and the 0.075 in. built-in deformation. The onset of buckling is clearly noted when the displacements start increasing rapidly at 0.605 in. displacement and 4.43 in. deflection. The slight drop in deflection to 4.24 in. at 1.21 in. displacement occurs at the snap-back immediately after the buckling load shown in Figure 4.1-14 and 15. When the analysis stopped, at 2.80 in. displacement and 5.22 in. deflection, the slope of the curve was about 100 percent meaning that the displacement was increasing about 1 inch per inch of vertical deflection.

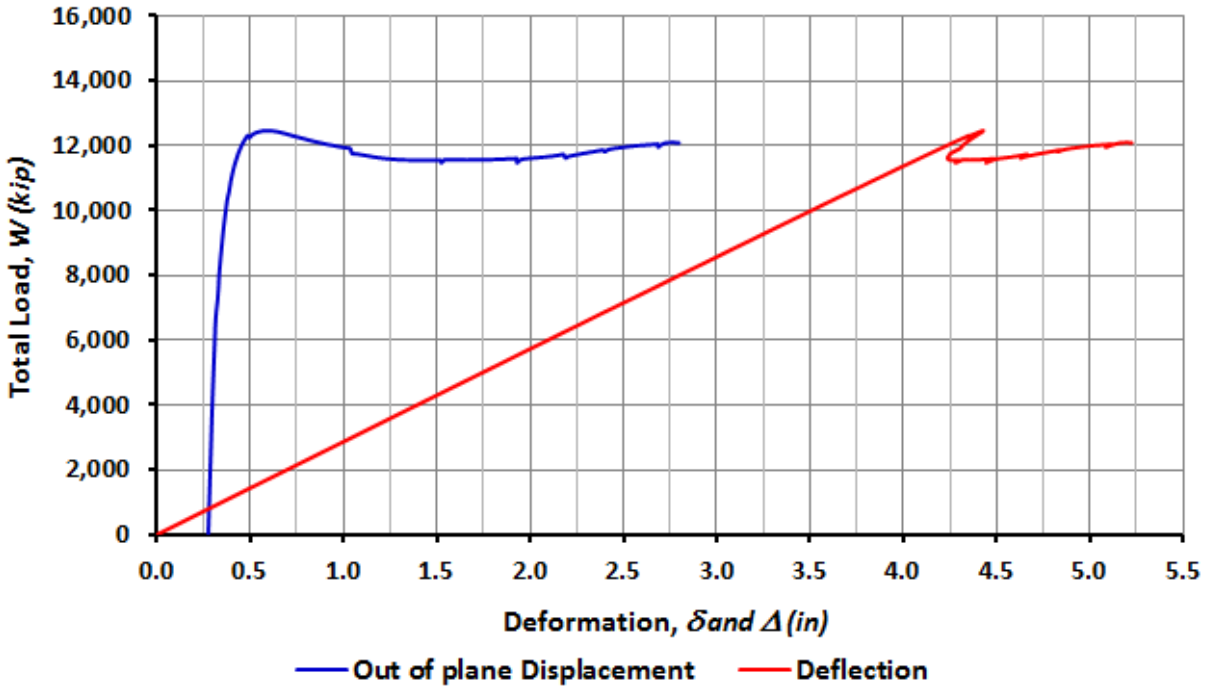

Figure 4.1-14: Total load vs deformations at node U10

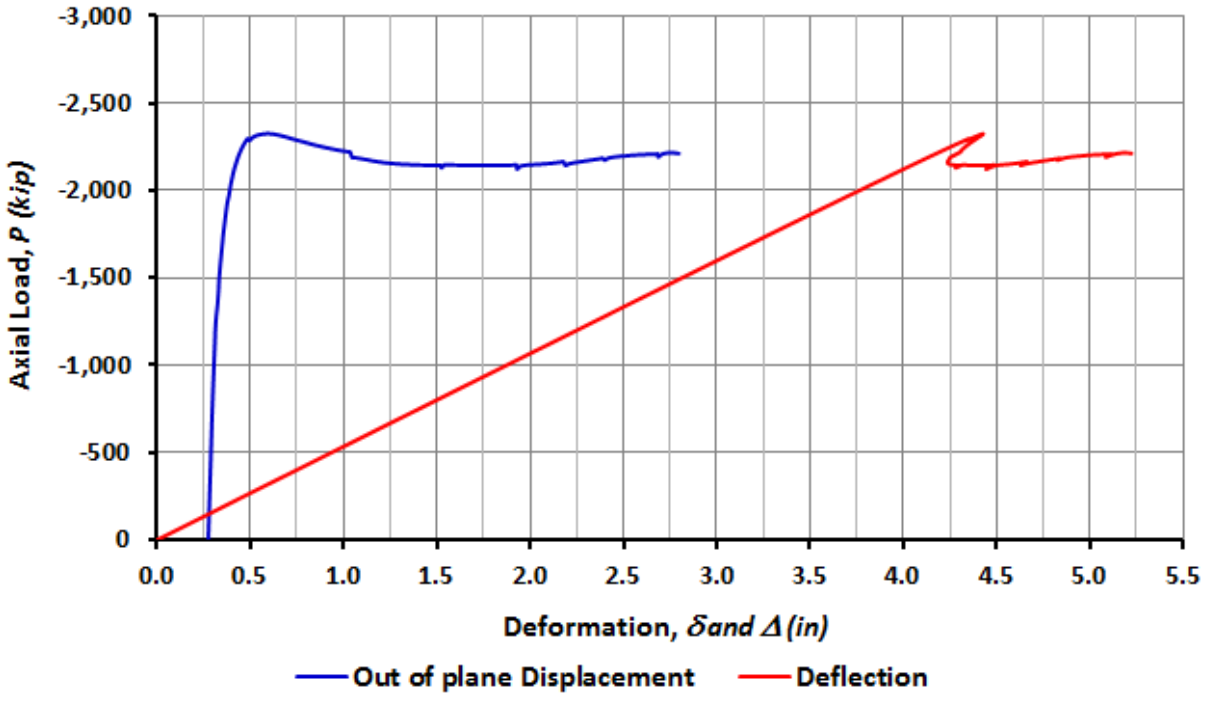

Figure 4.1-15: Axial force of L9-U10 diagonal vs deformations at node U10

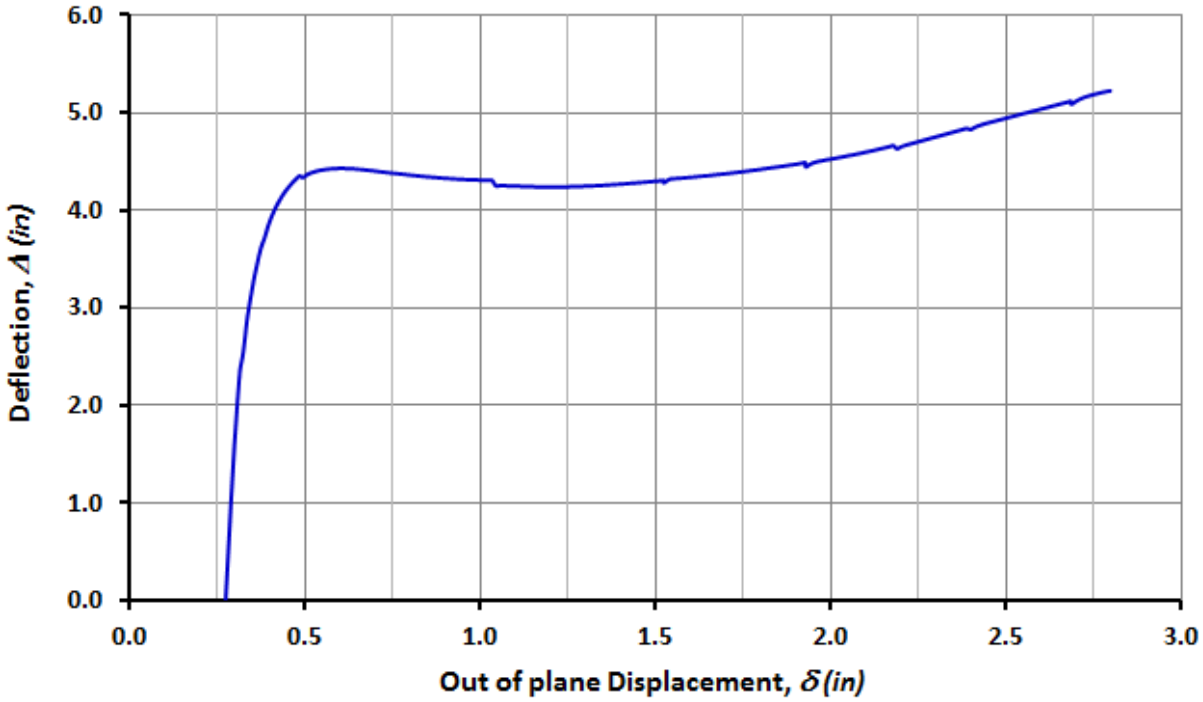

Figure 4.1-16: Deflection vs out-of-plane displacement of U10 gusset plate

The structural model with the detailed U10 gusset plates is very computationally demanding and encounters convergence problems shortly after the buckling capacity. For these reasons, the model was simplified by replacing the gusset plates with a single Nonlinear Link connecting the L9-U10 diagonals to nodes U10 at both ends of the main truss center span. The remaining four elements at these joints remained connected directly to the U10 nodes. This link is intended to represent the pre and post buckling behavior stiffness of the gusset plate connection.

The Nonlinear Link was modeled from the outer-most row of rivets connecting the L9-U10 diagonal to node U10, resulting in a segment length of 61.5 in. The behavior of this segment is defined by the axial force transferred from the compression diagonal and the deformation of the segment. As shown in Figure 4.1-17, the buckling axial capacity of 2,319 kip is reached at 0.07 in. deformation, followed by the drop to 2,137 kip at 0.24 in. deformation, and later followed by

a slight increase up to approximately 2,205 kip axial force and 0.80 in. deformation where the curve flattens-out.

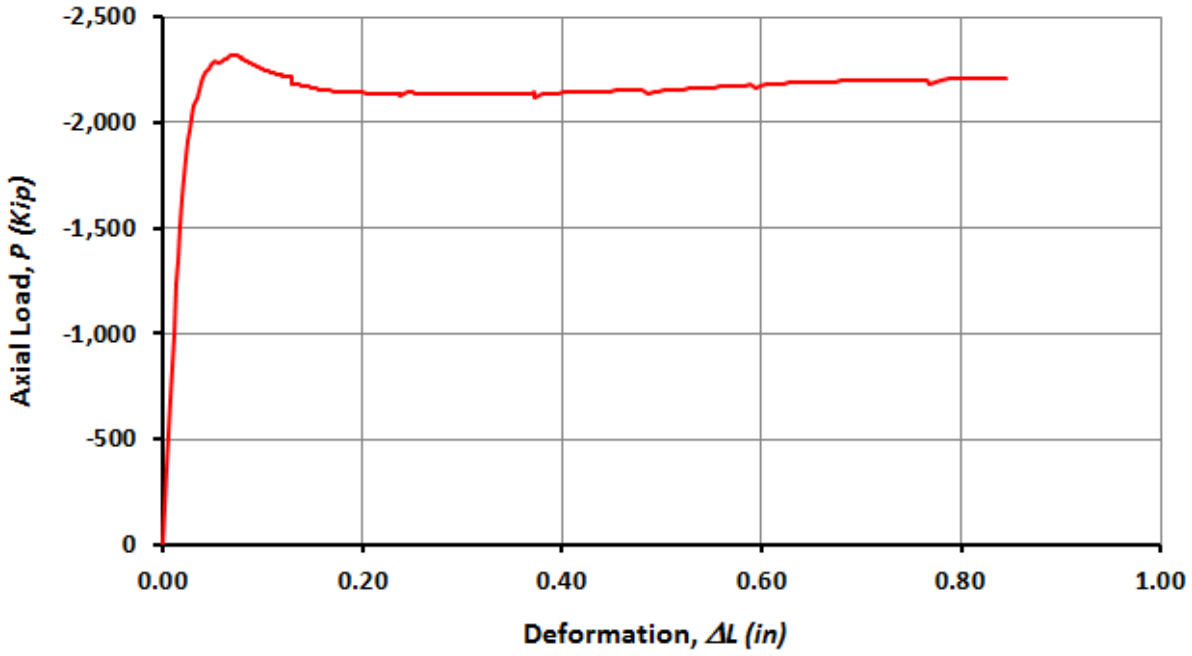

Figure 4.1-17: Force vs deformation of U10 gusset plate, L9-U10 segment

The constitute model of the link was defined by an idealized five-part multilinear relation that describes the behavior of the segment as shown in Table 4.1-5 and Figure 4.1-18. The first line goes from zero to 1,517 kip axial force where softening due to material and geometric nonlinearities become noticeable. The second line rises with a decreased slope to 2,137 kip and the third line keeps this force constant until the nadir of the valley that occurs following the buckling capacity. The fourth line goes up to 2,205kip at the end of the analysis and the fifth line assumes the force is constant thereafter.

This approximation ignores the peak at the buckling load because SAP2000 nonlinear capabilities cannot capture the snap-back shown in Figures 4.1-14 and 15 in the 2D model. The monitored displacement in the detailed U10 connection model is the out-of-plane displacement of the reference point, but this is not allowed in the 2D model. In addition, fracture is likely to occur in the gusset plate shortly after where the analysis stopped. This would represent an additional drop in loading. Since evidence from the wreckage shows that the U8-U10 upper chord member came to bear against the L9-U10 diagonal member at some point during the collapse and the final goal of this research is to get the overall picture of the collapse mechanism, the fifth line keeps the final axial force constant with an unlimited deformation capacity.

Table 4.1-5: Axial forces and deformations of the nonlinear links at nodes U10

Deformation (in)	Axial force (kip)
0.0000	0
0.0172	-1,517
0.0310	-2,137
0.2384	-2,137
0.8456	-2,205
1.0000	-2,205

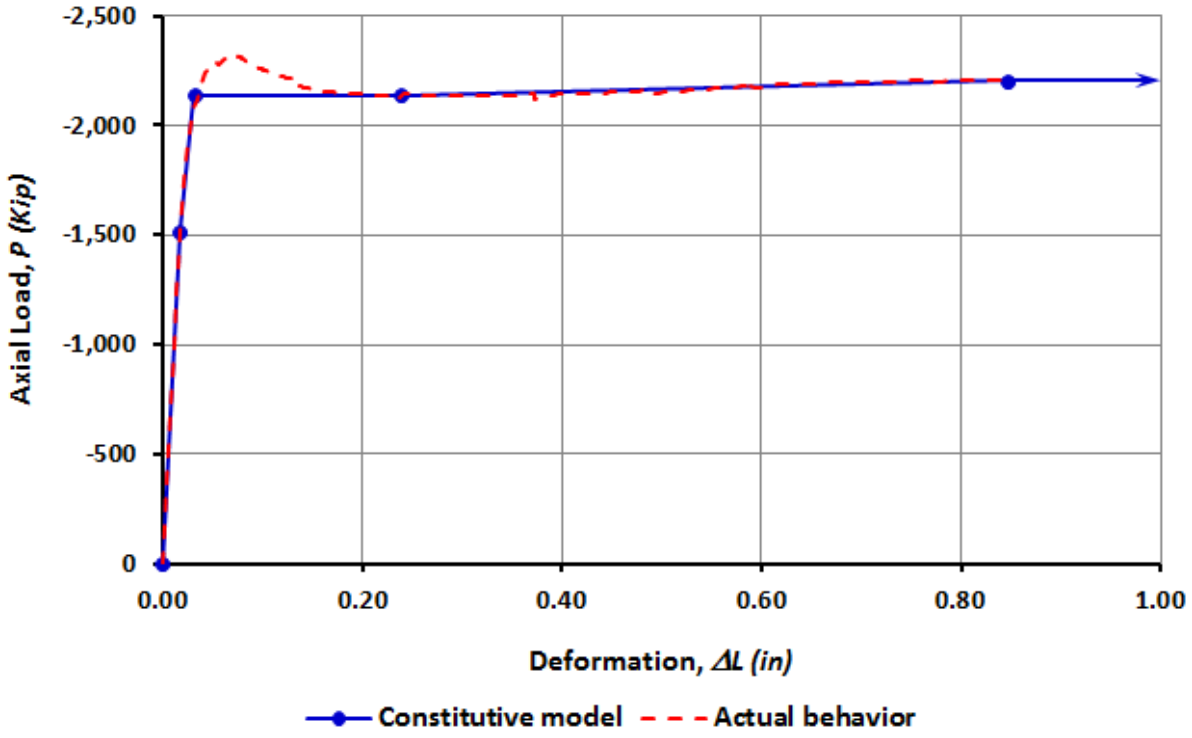

Figure 4.1-18: Force vs deformation of the nonlinear links at nodes U10

The simplified model was run to verify the accuracy of the Nonlinear Links. The total load on the truss and the axial force in the L9-U10 diagonal are plotted versus the U10 node deflection as shown in Figures 4.1-19 and 20, respectively. It is seen that the simplified model results correlate very well with the detailed model, except around the peak where snap-back occurs in the detailed model. The simplified model behavior accurately matches the detailed model up to about 4 in. deflection, and after about 4.2 in. deflection showing that it reasonably predicts both the pre and post buckling behavior. The axial force in L9-U10 remains constant after the end of the detailed model while the total load keeps increasing with the stiffness decreased to 6.5 percent of the initial stiffness.

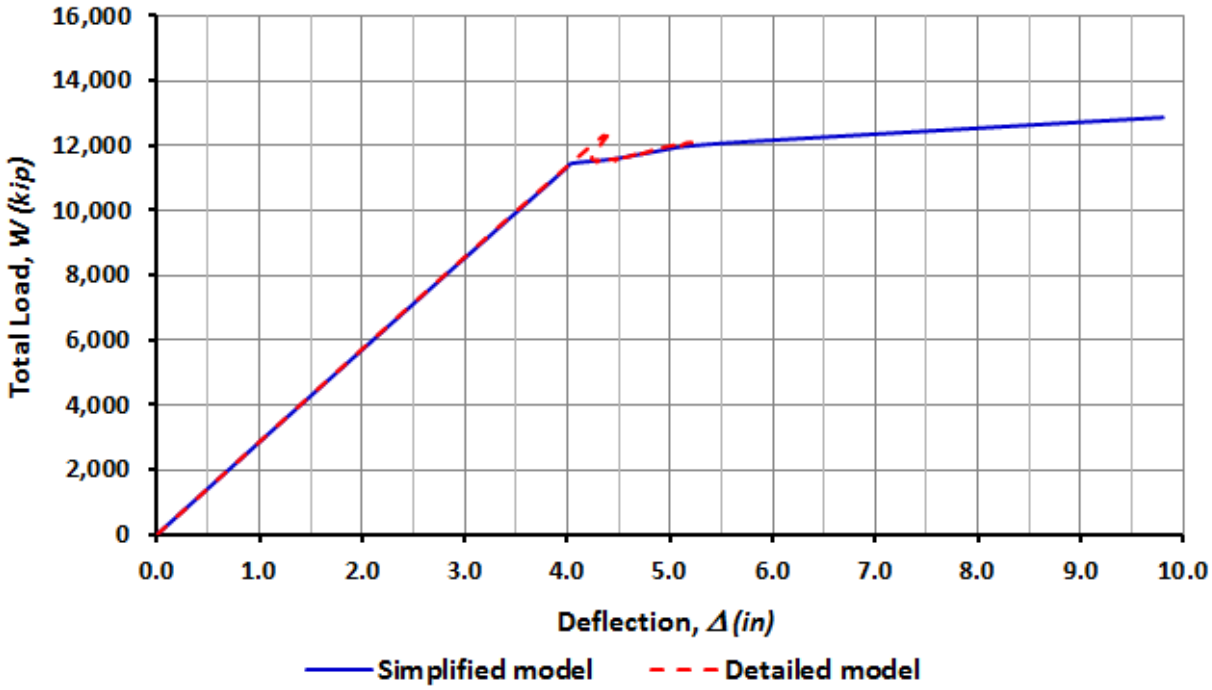

Figure 4.1-19: Total load vs deflection at node U10 for idealized behavior

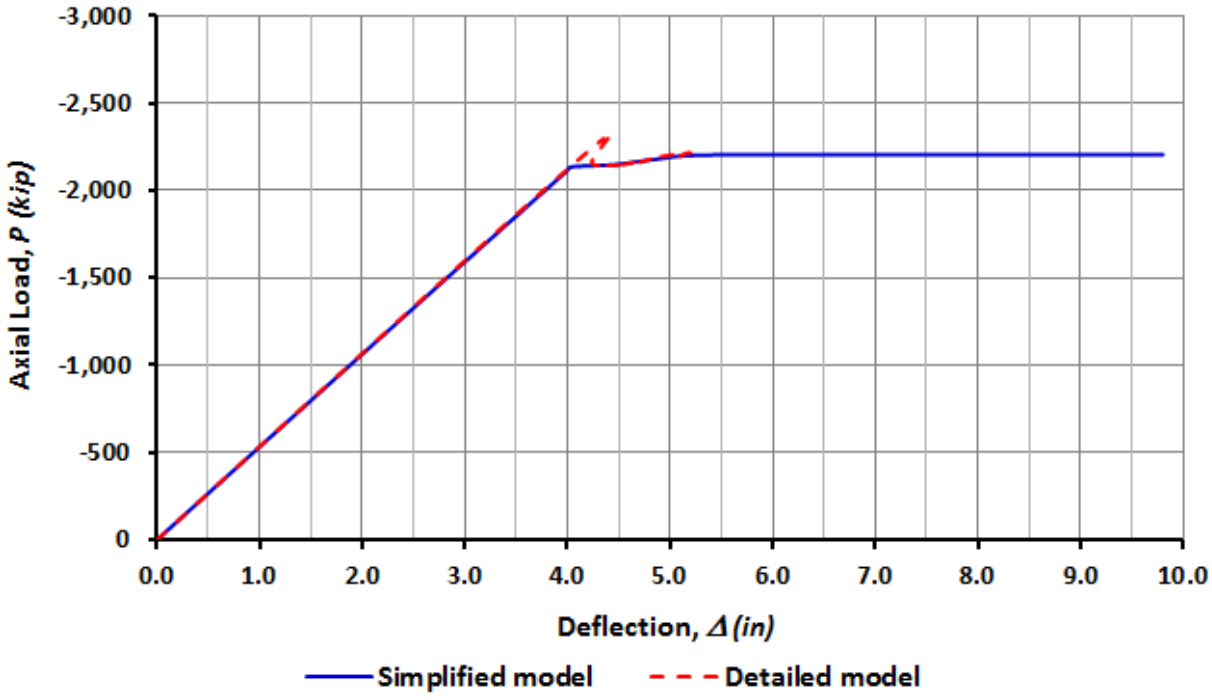

Figure 4.1-20: Axial force vs deflection at node U10 for idealized behavior

4.2 Frame Hinges Calibration and Validation

The discrete Frame Hinges described in Section 3.4 were used to capture the nonlinear behavior occurring at the mid and end-points of the upper and lower chord members between node locations 9 and 10 (U8-U10 and L9-L11). The plastic contours of these diagrams are calibrated in this section based on the results of the detailed FEM described in Section 3.5.

Comparing the relative thicknesses of the U10 connection plates to the side and cover plates of the U8-U10 member, and considering the buckled condition of the gusset plates, makes it obvious that this connection was not strong enough for the member to develop a plastic hinge at that end. Evidence from the wreckage supports this idea. In order to get a more realistic plastic contour for the U10 end of the U8-U10 member, an idealized cross section was conservatively used assuming that the buckled gusset plates only retain shear stiffness along the bottom row of rivets to restrain the upper chord member. The net shear area was defined as a rectangle with its centroid located along the bottom row of rivet holes and the shear yield strength was assumed as 60 percent of the tension yield strength. The idealized cross section is shown in Figure 4.2-1.

The chord members of the main trusses were built in contact at the connections, therefore the compression forces were carried by bearing between the member ends while the tension was carried by the connection plates. As shown in Figure 4.2-1, the discretized cross section for fiber analysis was defined with compression only fibers for the member plates (shown in blue), tension only fibers for the connection plates (shown in red) and longitudinal shear only fibers (shown in green). The static yield strength was used for the connection plates because the stresses in the gusset plates were close to yield at the time of the collapse. The resulting interaction diagram is shown in Figure 4.2-2.

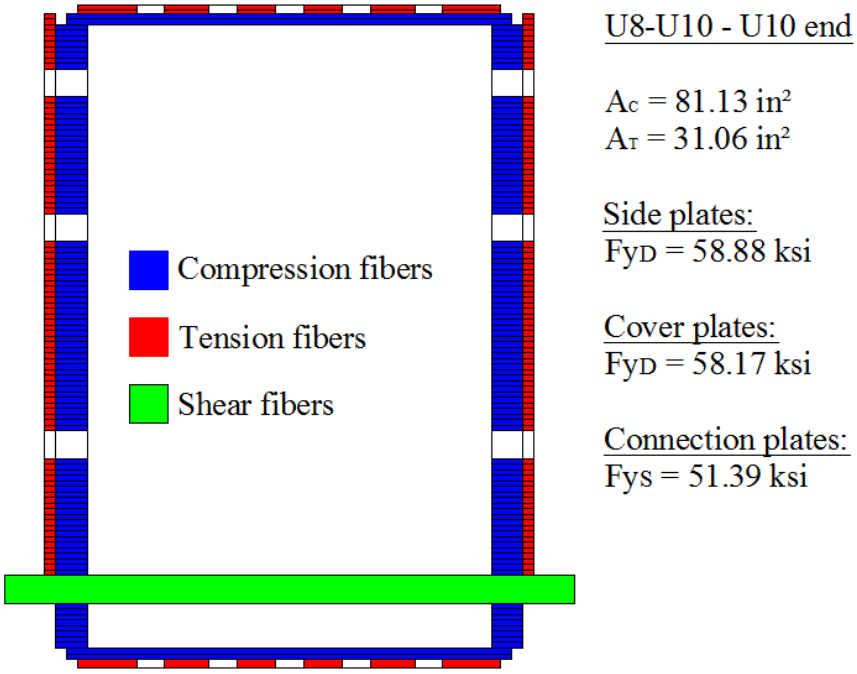

Figure 4.2-1: Discretized cross-section for fiber analysis of U8-U10 member at U10

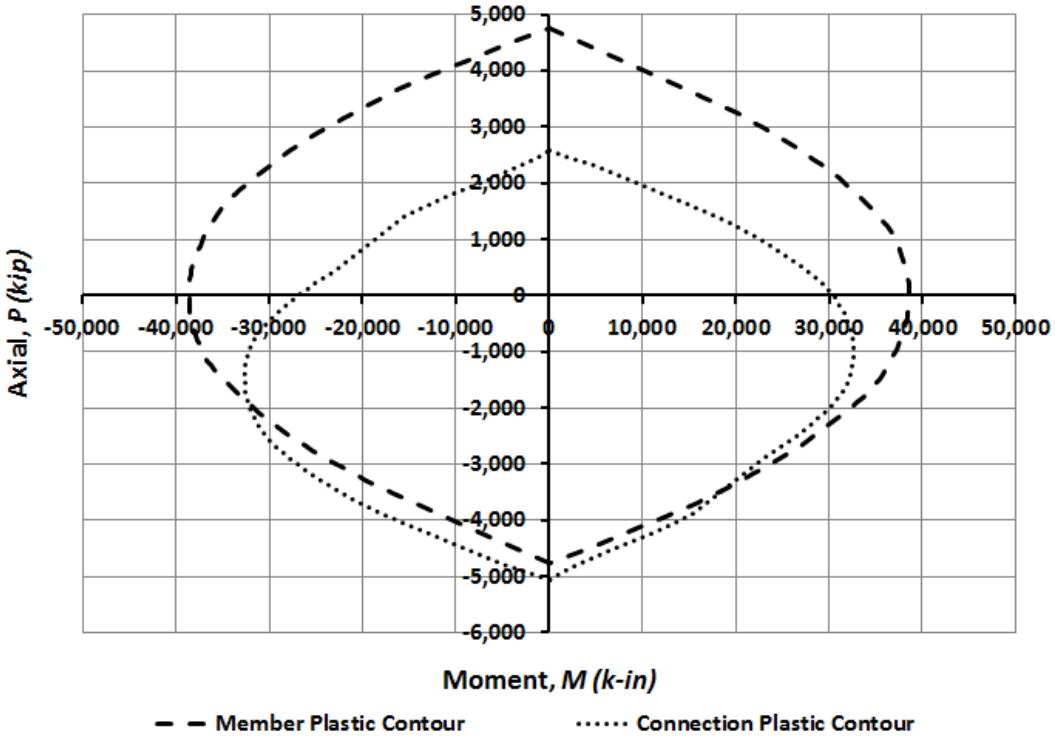

Figure 4.2-2: Axial-flexure interaction diagram for critical sections of U8-U10 members

The purpose of performing the detailed finite element analysis of the segment of the member L9-L11 is to provide a calibration point to scale the interaction diagram obtained from the fiber analysis. The sources of possible inaccuracy in the plastic contours calculated previously are:

- The cross section containing the rivet holes coincides with an edge of one access hole, not with the net section, which may result in higher strength.
- The stresses concentrate at the edges of the access holes, and therefore yielding occurs first along these edges. This introduces the possibility of early local buckling in cross section, which may result in lower strength.
- Based on the elastic-perfectly plastic material constitutive model, the shell elements closer to the neutral axis may not reach yield, which may result in slightly lower strength.

The loading used for the nonlinear analysis included the segment self-weight and the point loads at the right end of the segment. The point loads were determined by analysis of the simplified 2D model containing the nonlinear links and are divided into the steel weight, service load which goes up to the modeled buckling load, and the collapse load which goes until the end of the analysis. These loads were assigned as increments from one load stage to the other. The collapse load increment was applied with a factor of 2.0 so that the final loading slope could go beyond the interaction diagram previously calculated in case the strength was actually higher. The point loads at the end of each stage are presented in Table 4.2-1.

Table 4.2-1: Elastic end forces of segment L9-L11 at different stages

Load state	Axial force (kip)	Shear force (kip)	Bending moment (kip-in)
Steel weight	-305.5	-0.684	37.28
Service	-1,109	0.937	81.61
Collapse	-1,256	-55.67	-2,315

Initial imperfections were modeled mainly on the nonlinear portion of the segment (see Figure 3.5-1) to trigger the buckling mode shown in Figure 4.2-3. Area loads were applied to some elements so that the side plates bow outward and the cover plates inward. These loads were changed by trial and error to obtain a maximum initial imperfection of 1/1000 of the plate width, resulting in 0.028 in. for the side plates and 0.020 in. for the cover plates. Once this target was achieved, the displacements were added to the original joint coordinates to get the initial imperfections in an unstressed condition and the area load were removed.

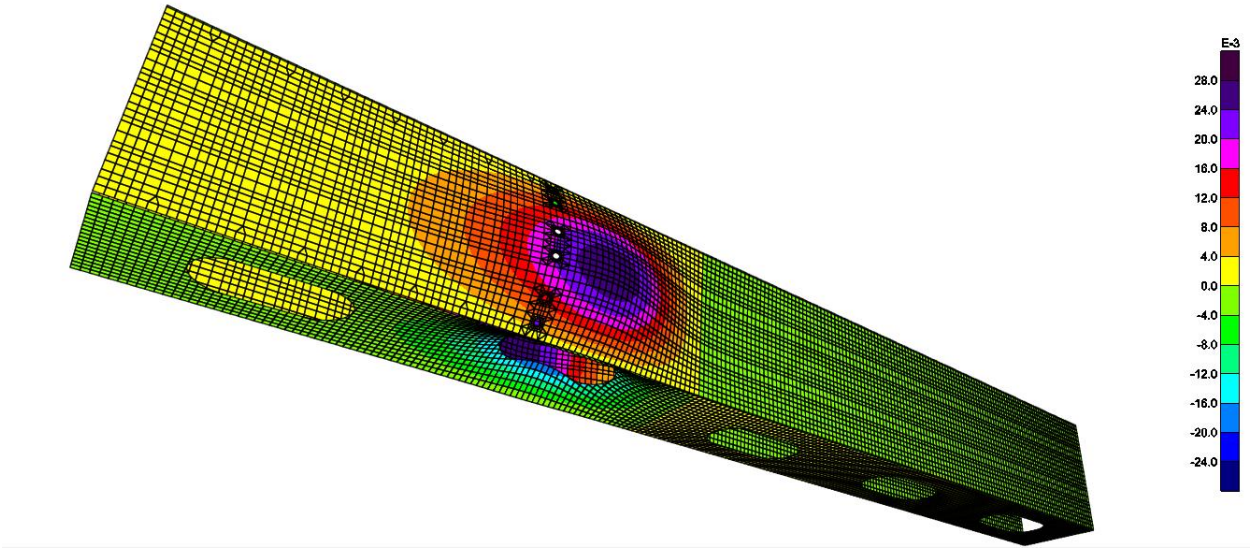

Figure 4.2-3: Initial out-of-plane imperfections (inches) of the L9-L11 detailed segment

The deflected shape of the detailed L9-L11 segment at the end of the analysis is shown in Figure 4.2-4. The overall deflection, with a maximum of about 1.20 inches (see Figure 4.2-5), looks very similar to a cantilever because the end of the segment is very close to the inflection point in the moment diagram. Local deformations are larger in the nonlinear portion, especially at the bottom where the compressive stresses are higher, which indicates that a buckling mode was starting to develop when the maximum capacity was reached. The in-plane deformations of the bottom cover plate are shown in Figure 4.2-6.

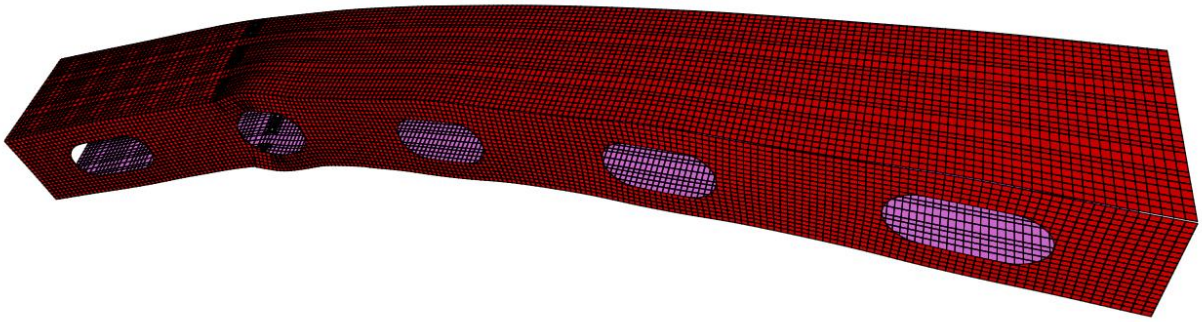

Figure 4.2-4: Deflected shape of the L9-L11 detailed segment, looking up to southwest

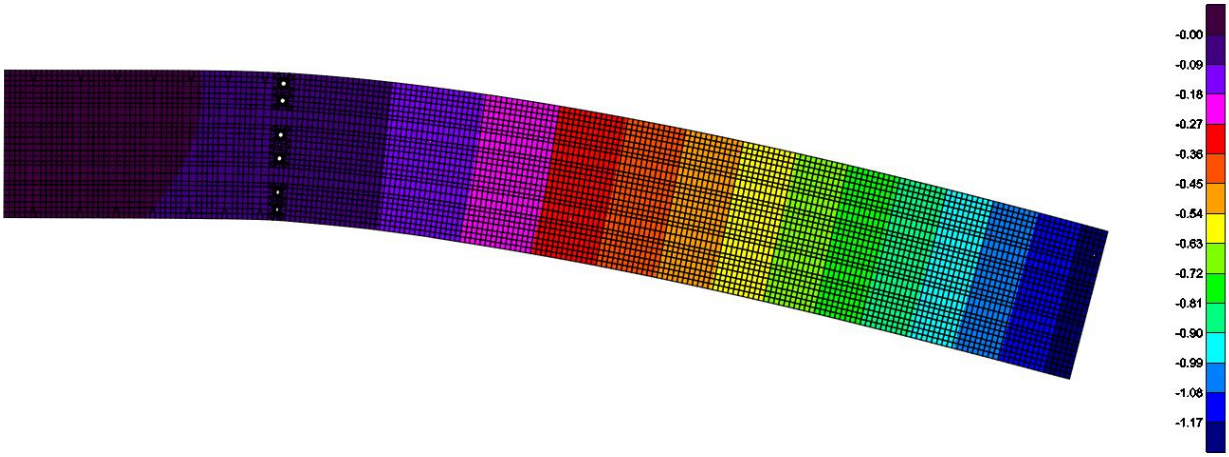

Figure 4.2-5: Vertical deflection (inches) of the L9-L11 detailed segment

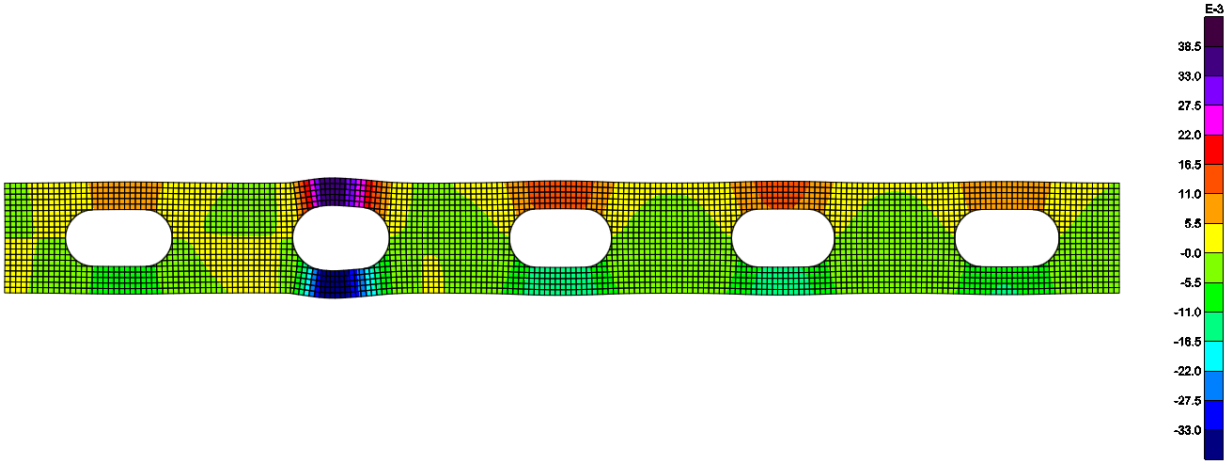

Figure 4.2-6: East-to-west deformations (inches) of the L9-L11 detailed segment (Bottom plate)

The axial stresses in the different plates are shown in Figure 4.2-7. At the critical section where the rivet holes were modeled, compressive stresses at the bottom are at the yield strength of $44.29\,ksi$ up to about the third rivet hole and then decrease in an approximately linear distribution to zero stress at about the second rivet hole from the top where the neutral axis is located, about 4.5 in. from the top. The maximum tensile stresses at this cross section (about $32\,ksi$) occur at the edges where the side plates are connected to the top cover plates. The average stresses in the central 10 in. portion of the cover plates are low but not zero thereby providing some additional strength that was not considered in the fiber analysis.

The maximum compressive stress occurs along the edges of the access hole located at the middle of the bottom cover plate, but this location was modeled with linear shells elements that do not consider yielding. The maximum tensile stress of about $35\,ksi$ occurs at the edges of the second access hole in the top cover plate located from the left end of the segment. Elements at this location have nonlinear material capability but yielding is not reached.

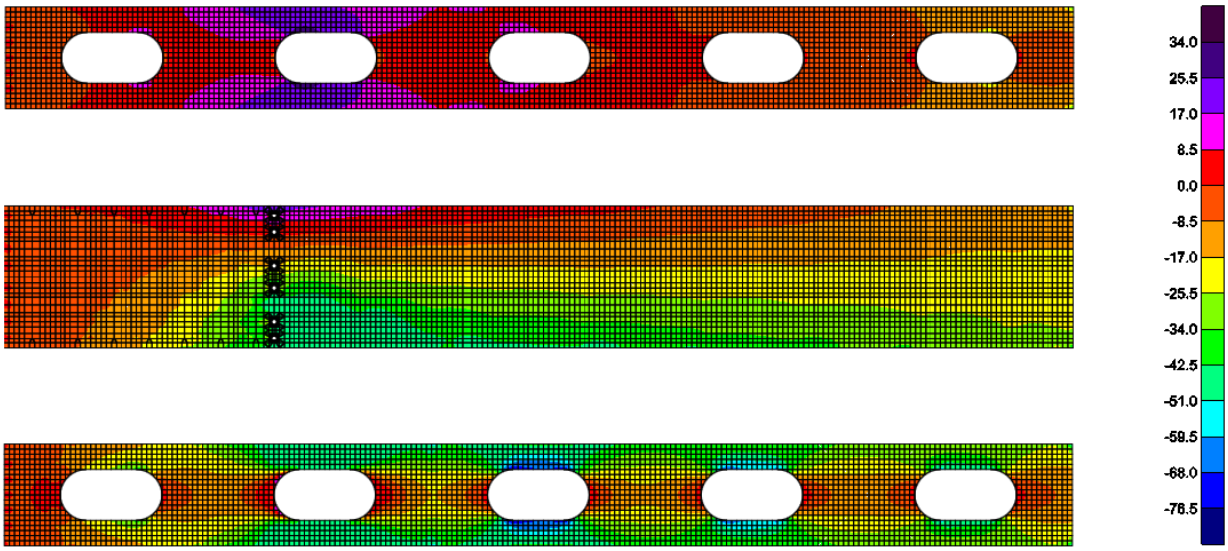

Figure 4.2-7: Longitudinal stresses (ksi) of the L9-L11 detailed segment
Top plate (top), side plates (middle) and bottom plate (bottom)

The nonlinear analysis stopped due to convergence problems when the axial force reached $1{,}265\ kip$ in compression and the moment at the net section reached $13{,}542\ in-kip$ in negative bending. The results are superimposed on the interaction diagram calculated from the fiber analysis in Figure 4.2-8.

The axial force increases with very little eccentricity up to $1{,}109\ kip$ in compression before the collapse initiated. After collapse begins, the eccentricity increased to a very high eccentricity of 86.65 inches. The resultant internal force in the net section at the end of the analysis slightly exceeded the plastic capacity that was previously determined; therefore, the actual strength is a little higher. This is probably caused by the low stresses at the center of the cover plates that were ignored in the fiber analysis.

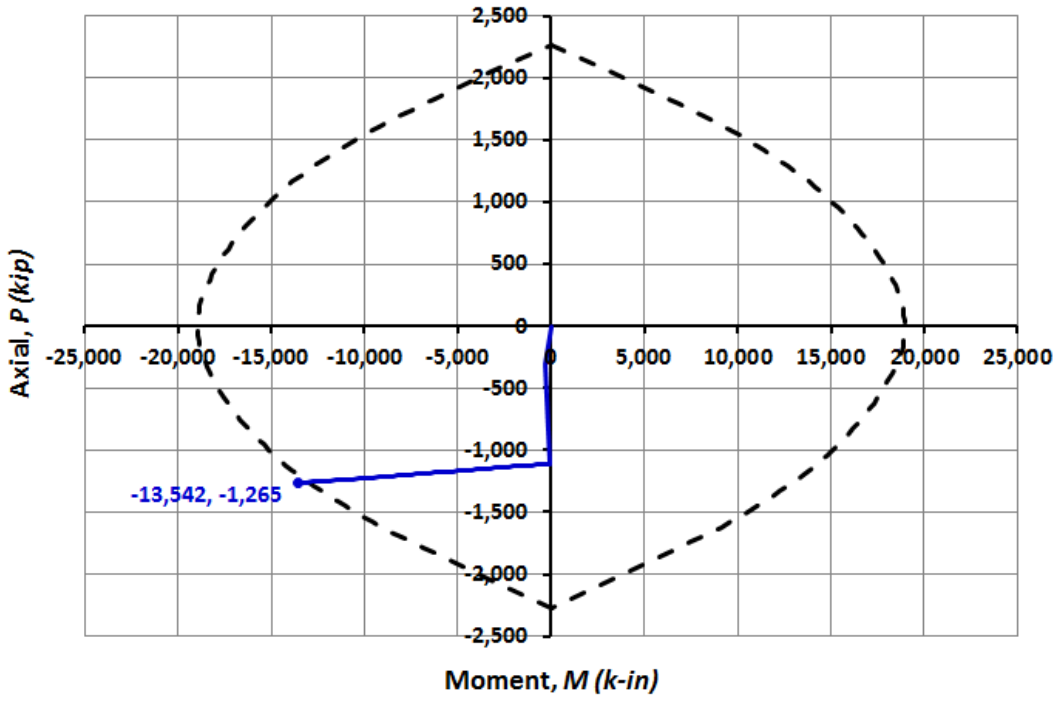

Figure 4.2-8: Applied force path and un-scaled interaction diagram of L9-L11 members

Results from the nonlinear analysis were used to scale the interaction diagrams calculated by fiber analysis. The scale factors for axial force $\boldsymbol{\alpha}$ and for bending moment $\boldsymbol{\beta}$ were calculated by comparing the applied forces, $\boldsymbol{P_u}$ and $\boldsymbol{M_u}$, to the nominal strength, $\boldsymbol{P_n}$ and $\boldsymbol{M_n}$, at the point where the applied force path intersects the un-scaled interaction diagram as follows:

$$\alpha = \frac{P_u}{P_n} = \frac{1{,}265}{1{,}259} = 1.005 \qquad \beta = \frac{M_u}{M_n} = \frac{13{,}542}{12{,}969} = 1.044$$

The scale factors $\boldsymbol{\alpha}$ and $\boldsymbol{\beta}$ were applied to the un-scaled axial forces and bending moments respectively to get the scaled interaction diagram that matches the analysis results, as shown in Figure 4.2-9. These same scale factors were applied to the interaction diagrams of the U8-U10 members assuming similar sources of additional strength. The scaled interaction diagrams that will be used in the collapse analysis are shown in Figures 4.2-10 and 11.

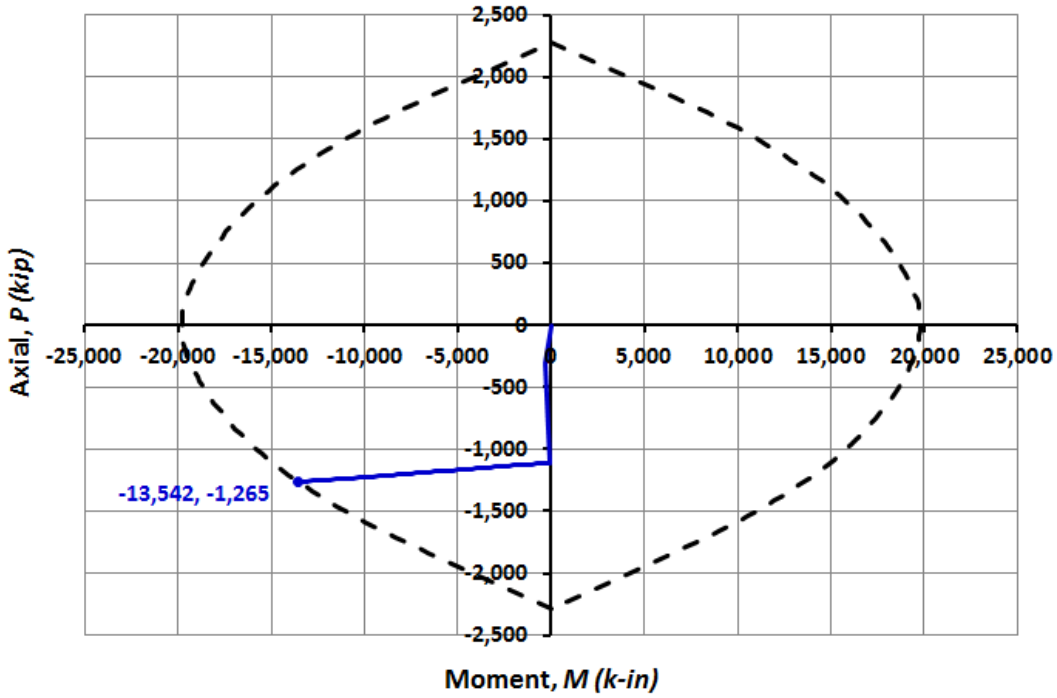

Figure 4.2-9: Applied force path and scaled interaction diagram of L9-L11 members

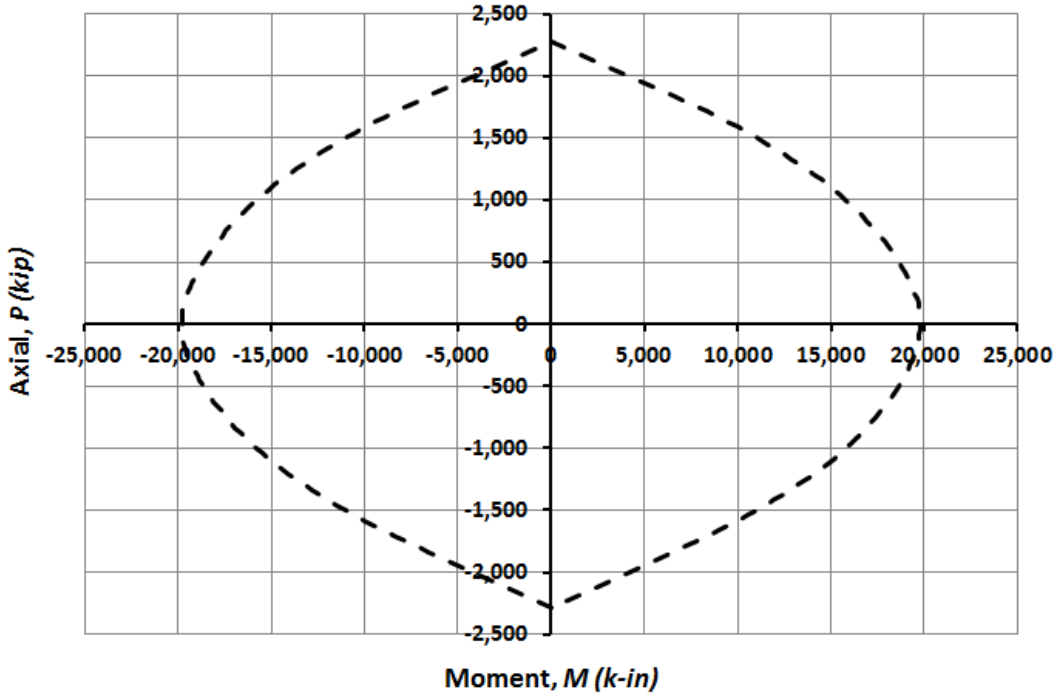

Figure 4.2-10: Scaled axial-flexure interaction diagram for net section of L9-L11 members

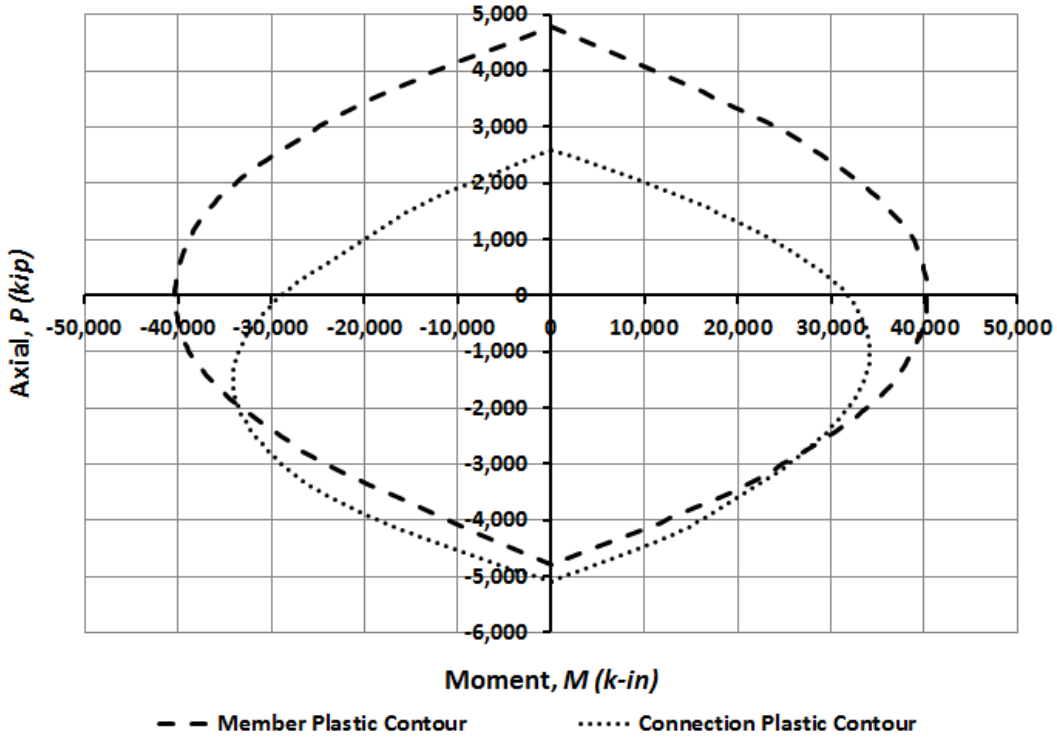

Figure 4.2-11: Scaled axial-flexure interaction diagram for U8-U10 members

4.3 Bridge Collapse Analysis

Nonlinear behavior was incorporated into the base two-dimensional model using the Nonlinear Links and Frame Hinges properties defined in the previous sections. Nonlinear Links are used at the U10 ends of the L9-U10 members to model buckling of the U10 gusset plates. Frame Hinges are used at the mid and end points of the chord members right above and below the L9-U10 diagonal, upper chord member U8-U10 and lower chord member L9-L11 respectively, to model potential plastic hinges at these locations.

In a first analysis, the full load of $12{,}863\ kip$ was applied to the model to study the inelastic behavior of the structural model under the best estimate of loading at the time of collapse. All the inelasticity occurs after load Stage 3 during the application of construction and traffic loads. The modeled buckling capacity on the Nonlinear Links of $2{,}137\ kip$ is reached first at node U10 and second at node U10'. Later, a plastic hinge develops at node L9 just before the full load was applied. The deflected shapes at the end of load Stages 3 and 4 are shown in Figure 4.3-1 and the deflections at control nodes U10, U14 and U14' are shown in Table 4.3-1.

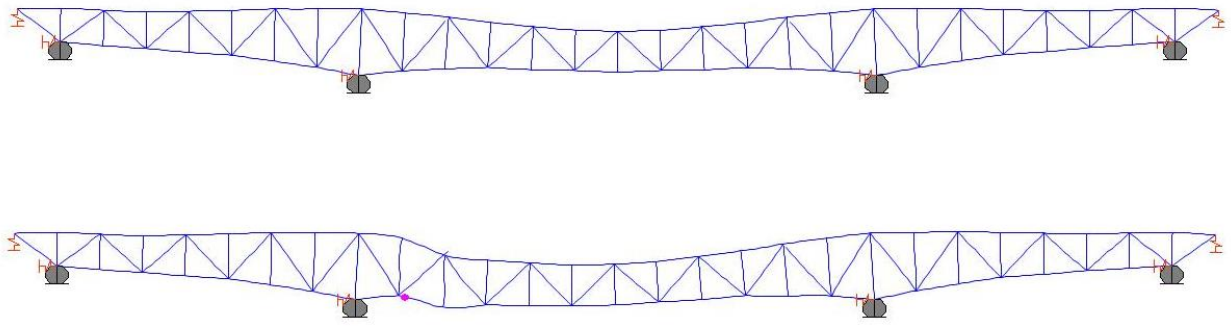

Figure 4.3-1: Deflected shape of west main truss under full load application At end of Stage 3 (top) and end of Stage 4 (bottom). Scale factor of 25

Table 4.3-1: Total load and deflections under full load application

Load stage	Load applied (kip)	Load percentage (%)	Deflections (in)		
			U10	U14	U10’
3	12,164	95	3.80	9.77	3.86
4	12,863	100	9.89	13.59	5.01

The total load versus deflection plots for the control nodes are shown in Figure 4.3-2. The first sudden change in stiffness defines the point where the buckling capacity is reached at node U10, and shortly thereafter there is a second stiffness change represents buckling at node U10’. There is a small amount of softening due to yielding at node L9 immediately before the total load is fully applied. Despite the fact that the model is still stable under the total load, the initial stiffness has dropped 98 percent at node U10.

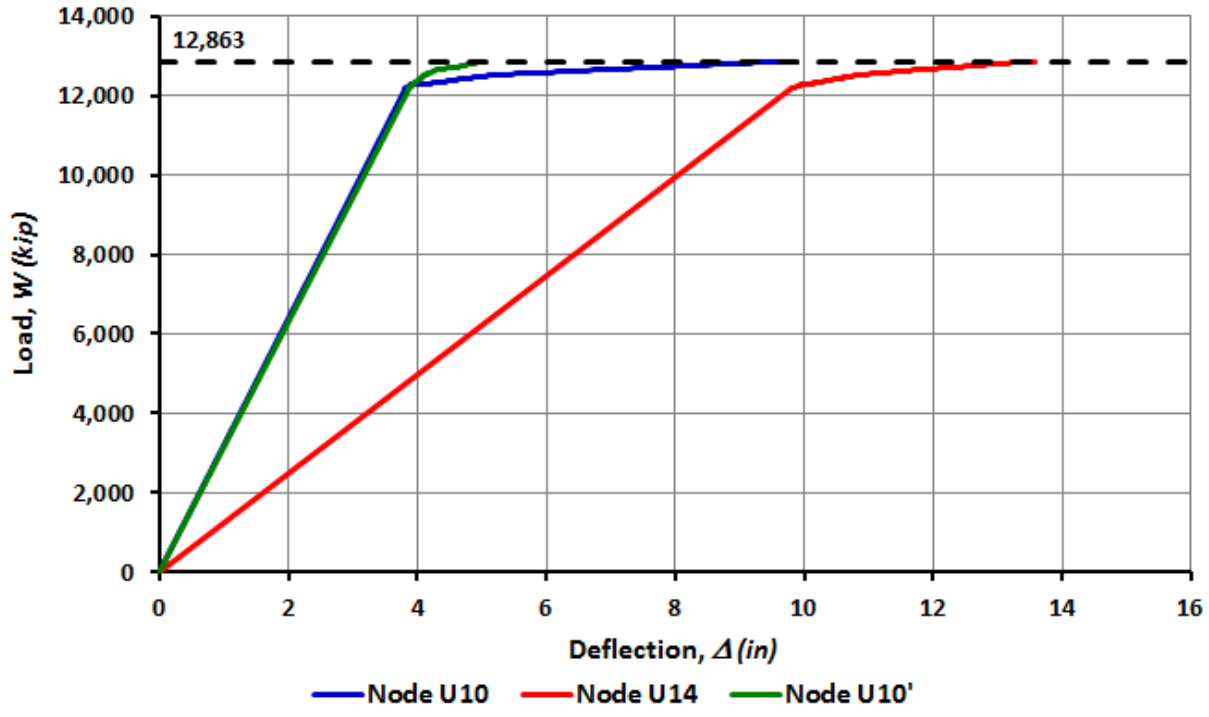

Figure 4.3-2: Total load vs deflection under full load application

The internal forces at the mid and end-points of L9-L11 bottom chord member are shown in Figure 4.3-3. The initial behavior is controlled by the axial forces due to the truss action. After buckling of the U10 gusset plates, bending moment becomes dominant with little increase in axial force. The L9 end of the member, shown in blue, reaches the plastic surface of the interaction diagram just before the end of the analysis.

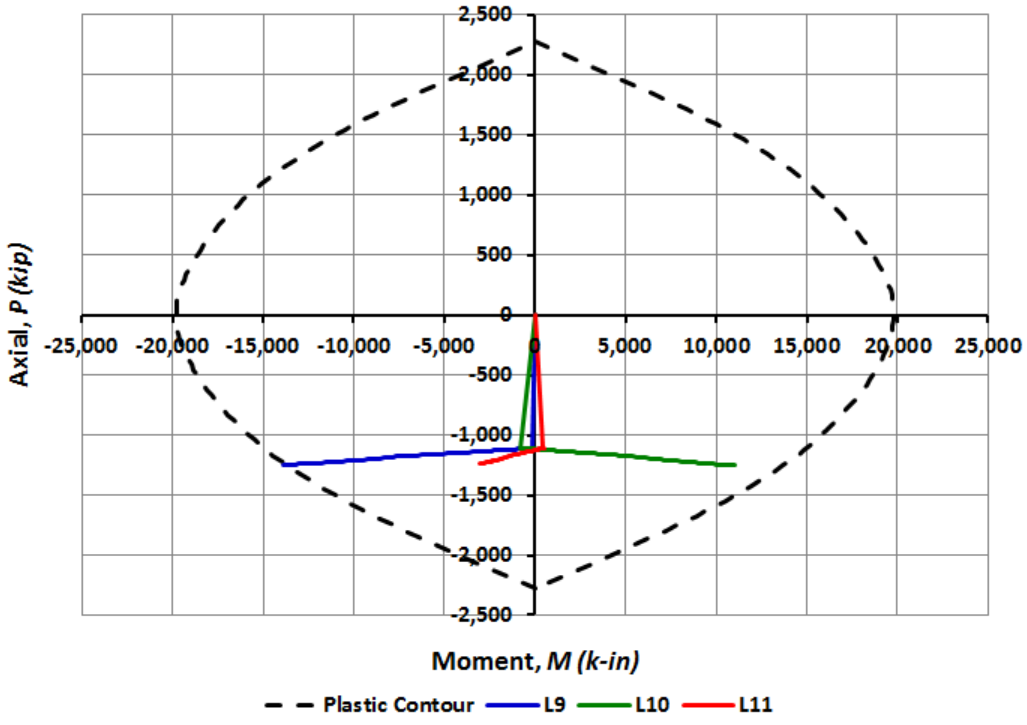

Figure 4.3-3: Internal forces in L9-L11 member under full load application

A second analysis was used to study the subsequent inelastic behavior and determine the load increment required to develop the collapse mechanism. Construction and traffic loads were applied in a displacement-controlled analysis until the collapse load was reached. The behavior from the end of load Stage 3 up to the total load of 12,863 kip is identical in both analyses because this analysis is an extension of the previous results.

Figure 4.3-4 shows the deflected shapes at the end of load Stage 3 and at the collapse load. Between the stage of full load application and the collapse load, seven additional plastic hinges develop and there is a large deflection increase. The 10-event failure sequence determined by this analysis goes as follows: buckling of gusset plates at nodes U10 (#1) and U10' (#2); plastic hinges develop at nodes L9 (#3); L10 (#4); U10 (#5); L9' (#6); L10' (#7); U10' (#8); L11' (#9); and U9 (#10).

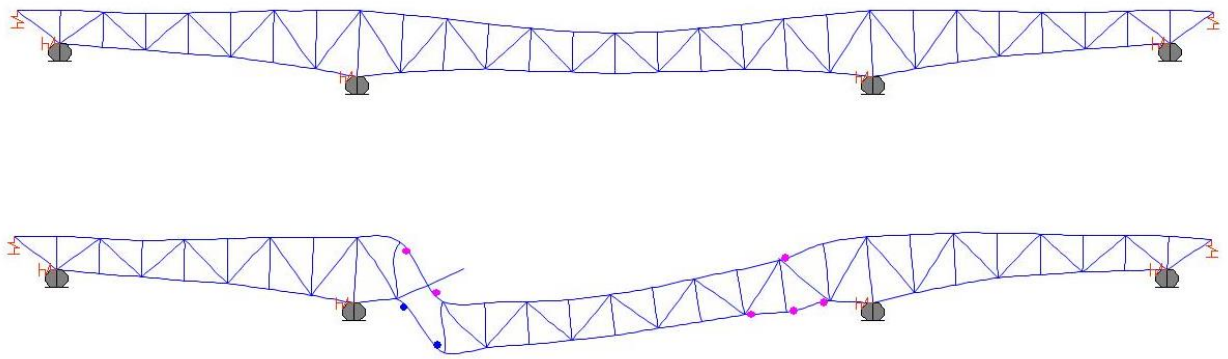

Figure 4.3-4: Deflected shape of west main truss at collapse
At end of Stage 3 (top) and end of Stage 4 (bottom). Scale factor of 25

The total load versus deflection plots for the control nodes up to the collapse load are shown in Figure 4.3-5 and deflections of the control nodes U10, U14 and U10' at the end of load Stages 3 and 4 and at the collapse load are summarized in Table 4.3-2. After the full load of 12,863 kip is applied, further stiffness reduction (softening) occurs as the plastic hinges develop at additional nodes. The deflections at node U10 increase faster compared to nodes U14 and U10'. The collapse load of 13,358 kip is only 495 kip or 4 percent higher than the best estimate of the total load at the time of collapse.

Table 4.3-2: Total load and deflections at collapse

Load stage	Load applied (kip)	Load percentage (%)	Deflections (in)		
			U10	U14	U10’
3	12,164	95	3.80	9.77	3.86
4	12,863	100	9.89	13.59	5.01
Collapse	13,358	104	28.03	25.03	10.45

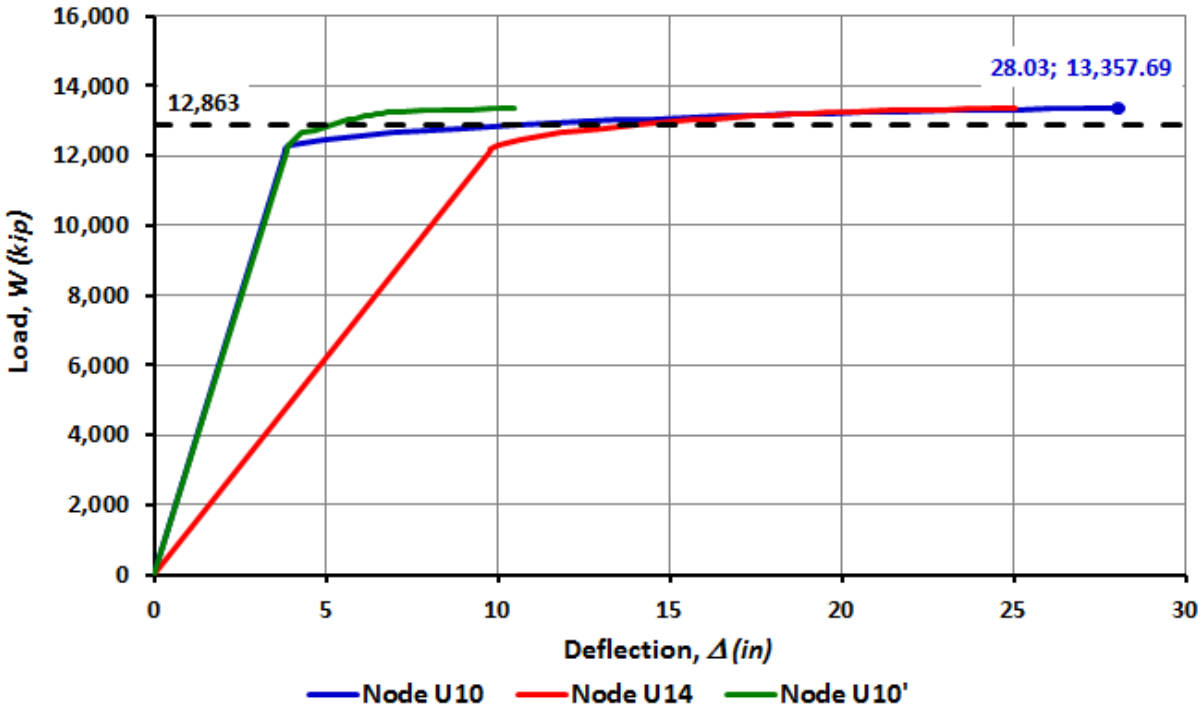

Figure 4.3-5: Total load vs deflection at collapse

Figures 4.3-6 through 4.3-9 show the internal forces in the four members where the Frame hinges were assigned. The L9-L11 member develops plastic hinges at nodes L9 and L10. The L9’-L11’ member develops hinges at three nodes as the axial plastic capacity (crush capacity) is approached. Member U8-U10 develops hinges at the U10 connection and at node U9. Finally, member U8’-U10’ only develops one plastic hinge at the U10’ end connection.

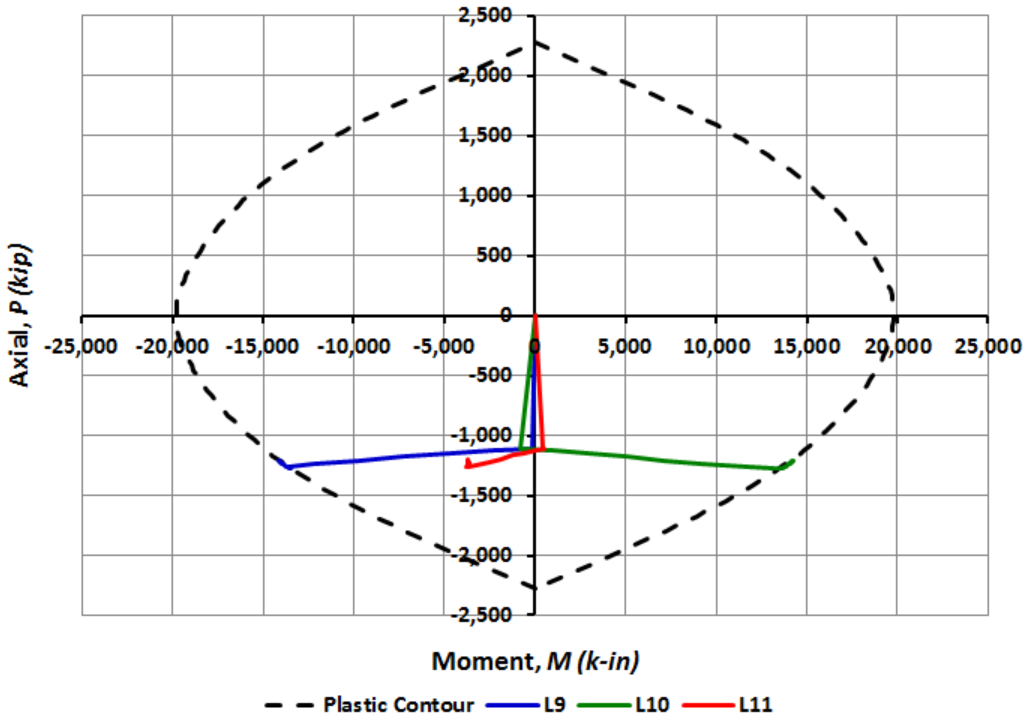

Figure 4.3-6: Internal forces in L9-L11 member at collapse

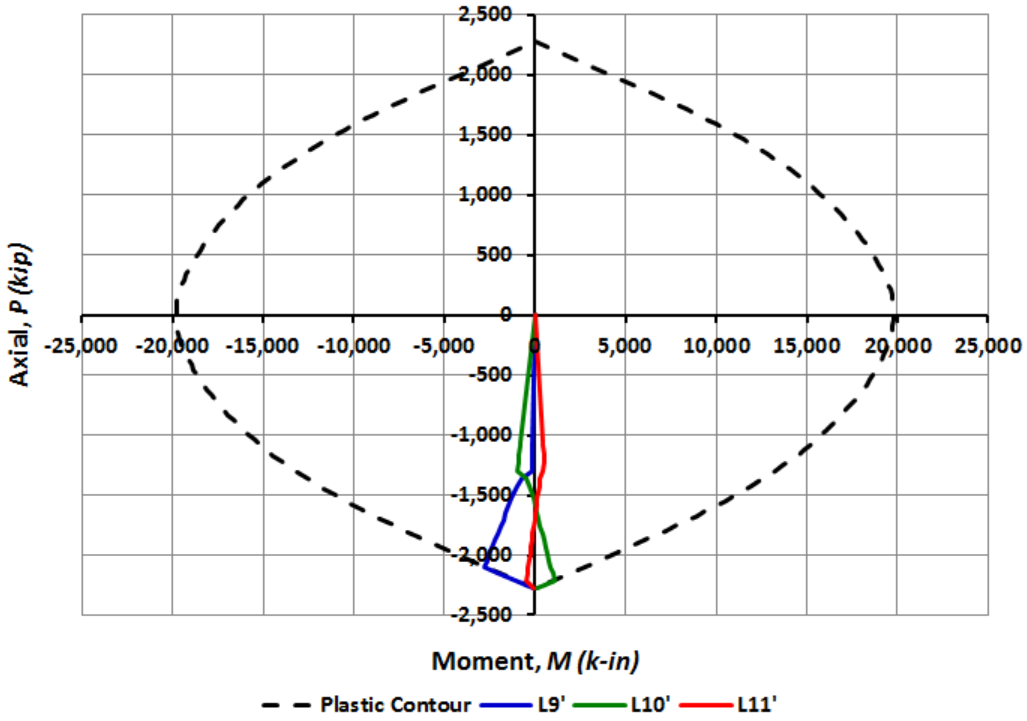

Figure 4.3-7: Internal forces in L9'-L11' member at collapse

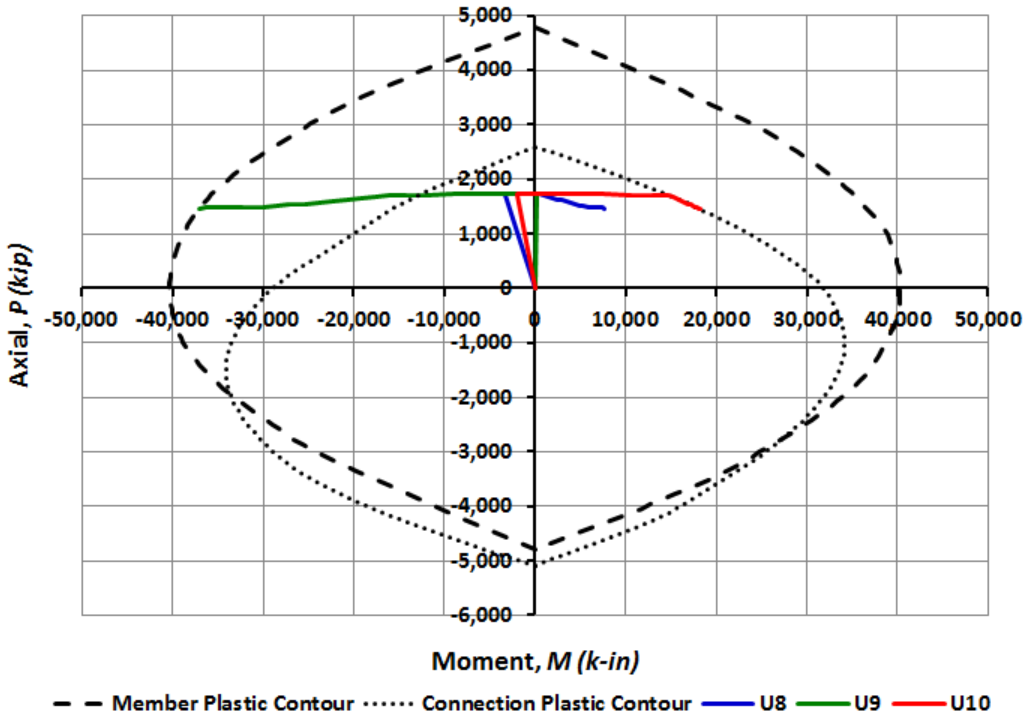

Figure 4.3-8: Internal forces in U8-U10 member at collapse

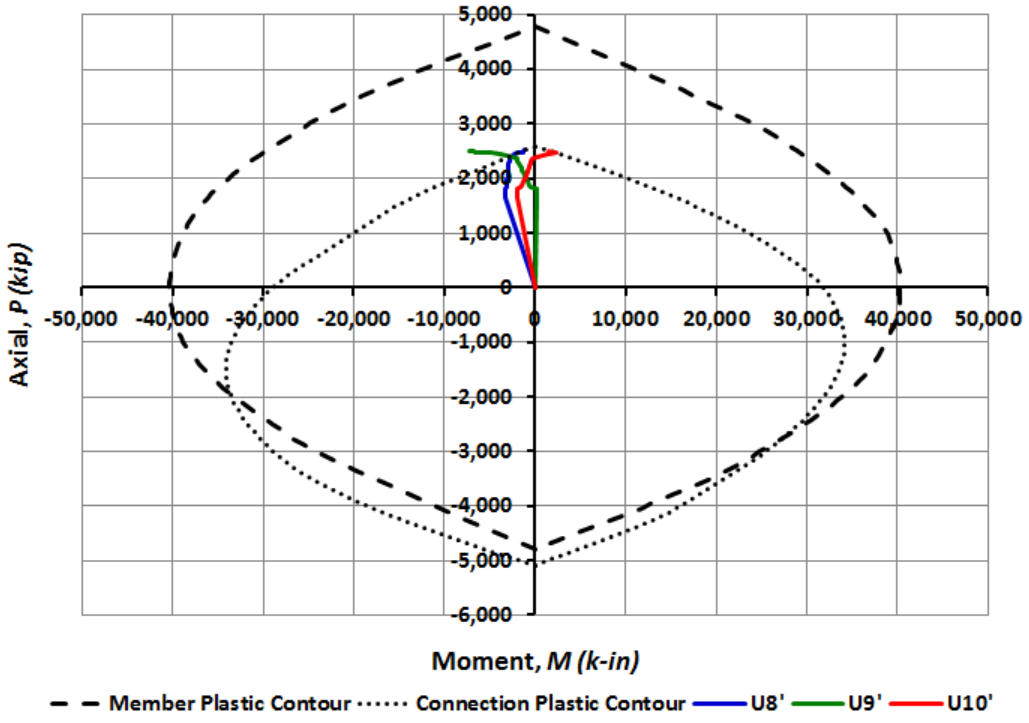

Figure 4.3-9: Internal forces in U8'-U10' member at collapse

The results above show that the collapse load is only $495\ kip$ higher than the total load applied in the model. As discussed in Ocel and Wright, 2008, the total dead load applied to the full model may be up to $300\ kip$ lighter than reality because of all the sources of uncertainty. In addition, the NTSB estimates a potential error of plus/minus 5 percent on construction and traffic loads, which is equivalent to $48\ kip$ in the full model. Within the accuracy of known facts, it can be stated that the 2D model with the frame hinges accurately predicts the collapse load and collapse mechanism of the bridge.

The axial force in the L9-U10 member was kept constant at $2{,}205\ kip$ after buckling of the U10 gusset plates, as shown in Figure 4.1-17. In reality, this load may drop at some point when the gusset plates fracture and the diagonal breaks free from node U10. Predicting this effect is complicated since the diagonal is known to have post-fracture bearing contact with the upper chord. The Frame Hinges assigned to the members L9-L11 and U8-U10 were defined with elastic-perfectly plastic constitutive models and infinite rotation capacity. In reality, the load may drop further due to fracture or local buckling at the critical cross sections.

Given the uncertainties on the load estimates and the assumptions on the behavior of the structure, the predicted collapse load of $13{,}358\ kip$, which is only 3.85 percent higher than the best estimate of the total load at the time of collapse ($12{,}863\ kip$) is accurate enough for the purpose of this research. The models provide an accurate event-to-event collapse sequence of the bridge showing the formation of the plastic collapse mechanism that is shown in Figure 4.3-10 and summarized in Table 4.3-3.

Table 4.3-3: Sequence of events up to the first collapse mechanism of the bridge

Event number	Event description	Load applied (kip)	Deflections at U10 (in)
1	Buckling L9-U10	12,282	3.93
2	Buckling L9'-U10'	12,573	5.93
3	Plastic Hinge L9	12,723	7.93
4	Plastic Hinge L10	12,997	12.53
5	Plastic Hinge U10	12,997	12.53
6	Plastic Hinge L9'	13,242	20.53
7	Plastic Hinge L10'	13,299	23.03
8	Plastic Hinge U10'	13,318	24.03
9	Plastic Hinge L11'	13,331	25.03
10	Plastic Hinge U9	13,358	27.03

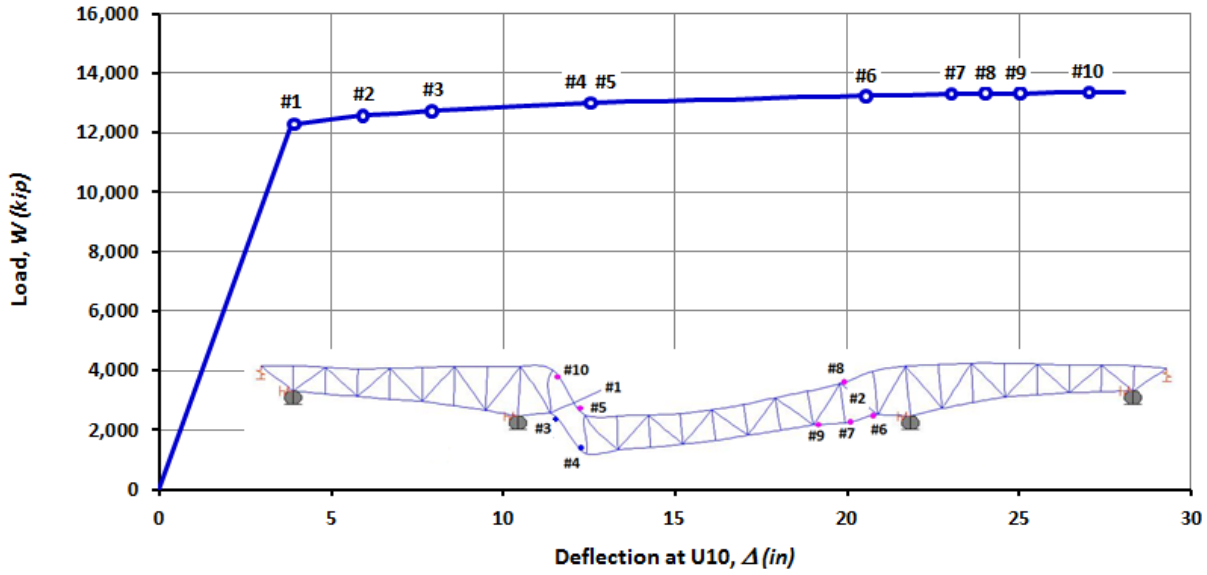

Figure 4.3-10: Collapse sequence of the bridge up to the first mechanism

4.4 Permanent Deformations

The comparison between the evidence and the analytical results is very important because it is an indicator of the validity of the results. The two main sources of evidence are the video footage captured by a security camera during the collapse and the measured deformations of the members recovered from the wreckage.

A motion-activated surveillance video camera recorded the collapse of a major part of the structure. The fourth frame of the video footage is shown in Figure 4.4-1 compared to the deflected shape at the end of the analysis. Both the bridge and the model are viewed from approximately the same northeast vantage point. It can be seen that the U10'-L10' vertical member pushes down at the mid-point of the L9'-L11' bottom chord and pulls down at the end of the U8'-U10' upper chord. This drop causes large rotations at nodes 9' and 10' of both chords. The deflected shape shown on the right indicates very pronounced deflections of the L9'-L11' and U8'-U10' members in a very similar mode to that captured by the video camera. This comparison validates that the nonlinear behavior at the north end of the center span that was captured by the structural model.

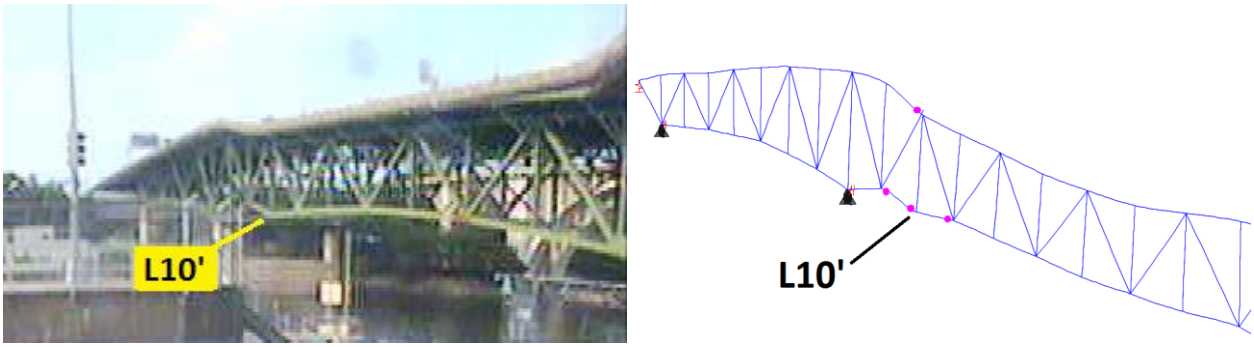

Figure 4.4-1: Deflected shapes of the bridge during collapse, looking northeast
Fourth frame captured by the security camera (left) and deflected shape at the end of analysis with a scale factor of 25 (right)

The nonlinear behavior at the south end of the center span was not capture by the video camera and therefore the same comparison with the deflected shape cannot be done at this area. The structure was recovered from the wreckage and permanent deformations of some members at the vicinity of the L9-U10 diagonal were measured by Dr. William Wright during the FHWA investigation. These deformations are compared to the structural analysis results in an effort to validate the nonlinear behavior captured by the structural model at the south end of the center span. The comparison is made on the L9-L10 segment of the L9-L11 bottom chord member because this is the location where the first plastic behavior occurred in the collapse analysis, therefore member behavior can be predicted with less uncertainty. Several factors may affect the accuracy of this comparison, such as changes in the proportioning of plastic deformations compared to the initial mechanism as the members begin to fracture. Another uncertainty is possible impact damage in the wreckage when the members contacted the river bottom and possible additional damage during the recovery process.

Figure 4.4-2: L9 end of the bottom chord segment L9-L10 recovered from the wreckage

The measured deformations on the L9-U10 member start at the innermost row of rivets at the L9 end, named as the reference location, where it completely fractured from the node during the collapse as shown in Figure 4.4-2. Measurements include out of straightness along the segment and the rotation angle at the L10 node. These deflections started 53 inches from the end of the member, projected to a straight line that connected the L9 and L11 nodes at the undeformed condition and then rotated 7.7 degrees to get the global locations and deflections. The results are shown in Table 4.4-1.

Table 4.4-1: Measured deformations of the L9-L10 segment

Location (in)			**Deformation (in)**	
Reference	**Local**	**Global**	**Local**	**Global**
0.000	53.000	**52.522**	0.000	**7.037**
6.000	59.000	**58.468**	0.875	**6.967**
12.000	65.000	**64.414**	1.500	**7.144**
18.000	71.000	**70.360**	1.938	**7.507**
24.000	77.000	**76.306**	2.188	**8.056**
30.000	83.000	**82.252**	2.375	**8.667**
36.000	89.000	**88.198**	2.563	**9.278**
48.000	101.000	**100.089**	2.750	**10.685**
72.000	125.000	**123.873**	2.875	**13.748**
96.000	149.000	**147.656**	2.750	**17.059**
120.000	173.000	**171.440**	2.375	**20.617**
144.000	197.000	**195.224**	2.188	**23.990**
168.000	221.000	**219.007**	1.875	**27.486**
192.000	245.000	**242.791**	1.625	**30.920**
216.000	269.000	**266.574**	1.375	**34.355**
240.000	293.000	**290.358**	1.188	**37.727**
264.000	317.000	**314.142**	0.875	**41.224**
288.000	341.000	**337.925**	0.688	**44.596**
312.000	365.000	**361.709**	0.438	**48.030**
336.000	389.000	**385.492**	0.313	**51.341**
360.000	413.000	**409.276**	0.125	**54.713**
373.625	426.625	**422.778**	0.000	**56.646**

The calculated deflections from the analysis results are also shown in Table 4.4-2. The total calculated deflections were taken from the same global location reference used for the measured deflections. The model results contain both elastic and inelastic deformation, while the measurements only contain the residual plastic deformation. A separate linear model of the member L9-L11 with the same applied external forces was used to obtain the elastic deflections so they could be subtracted from the total to get the plastic deflections.

As discussed previously, the collapse analysis stopped when the mechanism developed and no further information is available. Since two hinges had already developed in the segment at the end of the analysis, additional deflections in the structural model result from rigid body rotation up to the point of fracture. To compare the measured with the calculated deflections, the plastic deflections were scaled to the ultimate rotation capacity of the L9 plastic hinge, which has an approximate length of 20 inches based on evidence of cracks in the paint in the access-hole region as shown in Figure 4.4-2. The resultant scale factor of 6.595 is applied to the plastic deflections to get the scaled deflections presented in Table 4.4-2, which also show the differences with the measured deflections for comparison.

- Internal axial force: $P = -1{,}232\ kip$
- Depth of the tension block: $y_t = 4.50\ in$
- Curvature at plastic capacity: $\varphi_y = 0.0122\ in^{-1}$
- Curvature at rupture: $\varphi_u = 0.0267\ in^{-1}$
- Hinge length: $L = 20\ in$
- Plastic rotation by analysis: $\theta = 0.0428\ rad$

$$\Delta\varphi = \varphi_u - \varphi_y = 0.0267 - 0.0122 = 0.0145\ in^{-1}$$

$$\Delta\theta = \tan^{-1}(\Delta\varphi \cdot L) = \tan^{-1}(0.0145 \times 20) = 0.2823\ rad$$

$$SF = \frac{0.2823\ rad}{0.0428\ rad} = 6.595$$

Table 4.4-2: Calculated deformations of the L9-L10 segment

Global Location (in)	**Deformation (in)**				
	Total	**Elastic**	**Plastic**	**Scaled**	**Difference**
52.522	1.338	0.435	0.902	**5.951**	**1.086**
58.468	1.514	0.493	1.022	**6.737**	**0.230**
64.414	1.666	0.542	1.124	**7.411**	**-0.267**
70.360	1.817	0.592	1.226	**8.085**	**-0.578**
76.306	1.918	0.641	1.278	**8.425**	**-0.369**
82.252	2.120	0.690	1.430	**9.433**	**-0.766**
88.198	2.272	0.739	1.532	**10.106**	**-0.828**
100.089	2.617	0.838	1.779	**11.734**	**-1.048**
123.873	3.327	1.035	2.292	**15.118**	**-1.370**
147.656	4.038	1.232	2.806	**18.502**	**-1.444**
171.440	4.778	1.438	3.340	**22.027**	**-1.410**
195.224	5.506	1.635	3.871	**25.529**	**-1.539**
219.007	6.245	1.832	4.413	**29.106**	**-1.620**
242.791	6.985	2.029	4.956	**32.683**	**-1.763**
266.574	7.724	2.226	5.498	**36.261**	**-1.906**
290.358	8.460	2.432	6.028	**39.755**	**-2.028**
314.142	9.156	2.629	6.527	**43.045**	**-1.821**
337.925	9.852	2.826	7.026	**46.334**	**-1.738**
361.709	10.547	3.023	7.524	**49.623**	**-1.593**
385.492	11.158	3.228	7.929	**52.294**	**-0.953**
409.276	11.739	3.426	8.314	**54.830**	**-0.116**
422.778	12.079	3.541	8.538	**56.309**	**0.338**

The measured and calculated deflections are plotted in Figure 4.4-3. It is seen that the calculated deflections match the measured with reasonable accuracy given the possible sources of uncertainty. The measured curve shows significant rotation at the L9 end because the strain hardening effect spreads out the plastic strain. This is different from the assumed concentrated plasticity that occurs in the Frame Hinges used in the structural model. However, this comparison validates the nonlinear behavior at the south end of the center span that was captured by the structural model.

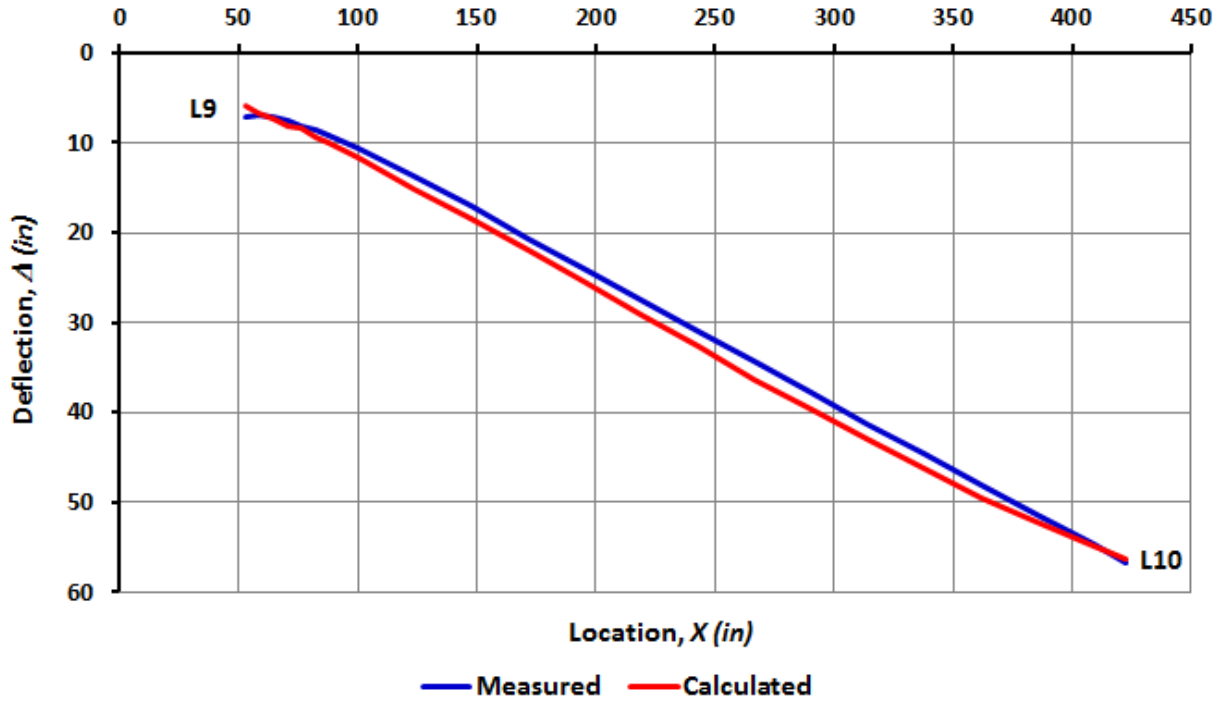

Figure 4.4-3: Measured and calculated deflections of the bottom chord segment L9-L10

CHAPTER 5. CONCLUSIONS

This thesis presents the event-to-event study of the collapse sequence of the I-35W Bridge, up to the point where a collapse mechanism was formed. Many structural models were created for different specific purposes and these were calibrated to get accurate results. Loads on the bridge were estimated based on the drawings and reported built weight of the structure, and post-collapse field measurements and observations. The boundary conditions were calibrated to field data collected by the University of Minnesota and the effect of the approach spans was taken as reported by the FHWA. The collapse study started with buckling analysis of specific critical gusset plates, which was the initial triggering event as concluded by the NTSB, and continued with inelastic behavior of the truss members. The results provide a better understanding of the inelastic behavior of the system. The most important findings are summarized as follows:

- The gusset plates at nodes U10 and U10' did not have adequate capacity to transfer the axial forces present in members L9-U10 and L9'-U10', the most heavily loaded compression diagonals. The loads on the bridge at the time of collapse were higher than the buckling capacity of these gusset plates. This corroborates the results of the NTSB investigation where gusset plate buckling created the initial instability in the system.

- Once the critical gusset plates buckled, the stiffness of the compression diagonals was lost and the chord members above and below these diagonals became flexural members. The resulting bending moments, combined with the axial forces already present, results in yielding in chord members L9-L11, U8-U10, L9'-L11' and U8'-U10', thereby forming a collapse mechanism.

The collapse of a major part of the bridge was captured by a surveillance video camera and permanent deformations of some members recovered from the wreckage were documented. The permanent deformations predicted in the nonlinear model correlate to the evidence with reasonable accuracy as described below:

- The deflected shape of the nonlinear model shows very pronounced deflections and rotations of the L9'-L11' and U8'-U10' members in a very similar mode to that captured by the video footage. The locations of the large rotations are in agreement with the locations of the plastic hinges in the nonlinear model.

- The calculated deflections of the L9-L11 member based on the nonlinear analysis results are in close agreement with the measurements of the member recovered from the wreckage. The calculated deflected shape does not capture the spread of plastic strains because the hinge properties defined assume concentrated plasticity.

Overall, this work develops an understanding of the plastic collapse mechanism that developed during the bridge collapse. There are no experimental system tests on anything approaching this scale, and therefore this information is important to anyone performing a system strength analysis. This work is particularly important to the on-going initiative to develop system analysis procedures to predict the residual strength and redundancy of truss bridges.

Recommendations for further research are:

- Verify the pre and post bucking behavior of the gusset with software that incorporates refined yield criterions like Von Mises.

- Study the behavior of the U10 end of the U8-U10 member by refined finite element analysis to get a more accurate understanding of the inelastic behavior at this location.

- Consider using adding distributed plasticity in the truss members to refine the correlation between the permanent deformations in the nonlinear model and the field measurements.

REFERENCES

Allied Structural Steel Company. (1966). General Management Plan, Elevation, & Sections for Bridge No. 9340 Over the Mississippi River. *(Revised 24 March 1966)*. Hammond, IN.

Beshah, F., Wright, W., & Graybeal, B. (2008). *Mechanical Property Test Report: I-35W over the Mississippi River*. Federal Highway Administration, Turner-Fairbank Highway Research Center.

Brazy, D. (2008). *Collapse of I-35W Bridge: Gusset Plate Photographs – Measurement Study Report.* National Transportation Safety Board, Vehicle Recorder Division, Washington, DC.

Bruneau, M., Uang, C.-M., & Sabelli, R. (2011). *Ductile Design of Steel Structures* (2nd ed.). McGraw-Hill.

CSI. (2009, April). CSI Analysis Reference Manual. Berkeley, California: Computers and Structures, Inc.

Graybeal, B. (2008). *Mechanical Properties of the Minneapolis I-35W Bridge Deck and Pier Concrete.* Federal Highway Administration, Turner-Fairbank Highway Research Center, McLean, VA.

Madison, R., & Irwin, G. (1974). Dynamic KIc Testing of Structural Steel. *Journal of Structural Division*.

Morrison, J., Brazy, D., & Schultheisz, C. R. (2007). *Report No. 07-115.* National Transportation Safety Board, Materials Laboratory Division, Washington, DC.

NTSB. (2008). *Collapse of I-35W Highway Bridge.* Highway Accident Report, National Transportation Safety Board, Washington, DC.

Ocel, J. M. (2013). *Guidelines for the Load and Resistance Factor Design and Rating of Riveted and Bolted Gusset-Plate Connections for Steel Bridges.* Turner-Fairbank Highway Research Center. McLean, VA: Federal Highway Administration.

Ocel, J. M., & Wright, W. J. (2008). *Finite Element Modeling of I-35W Bridge Collapse.* Federal Highway Administration, Turner-Fairbank Highway Research Center.

O'Connell, H. M., Dexter, R. J., & Bergson, P. (2001). *Fatigue Evaluation of the Deck Truss of Bridge 9340.* University of Minnesota, Department of Civil Engineering. St. Paul, MN: Minnesota Department of Transportation.

Salmon, C. G., Johnson, J. E., & Malhas, F. A. (2009). *Steel Structures: Design and Behavior* (5th ed.). Upper Saddle River, NJ: Pearson Prentice Hall.

Sverdrup & Parcel and Associates, Inc. (1965). T.H. 35W State of Minnesota Department of Highways, Bridge No. 9340 Design Drawings. *(Approved 18 June 1965).* St. Louis, MO.

WJE. (2008). *I-35W Bridge Over the Mississippi River Collapse Investigation.* Northbrook, IL: Wiss, Janney, Elstner Associates, Inc.

Wright, W. J. (2012, November). Steel Bridge Design Handbook. *Bridge Steels and Their Mechanical Properties, 1*, 24-26. Federal Highway Administration.